CHARACTERIZATION AND MODELING OF CONDUCTIVE AND INSULATING COATINGS FOR NEURAL INTERFACES

by

Saugandhika Minnikanti
A Dissertation
Submitted to the
Graduate Faculty
of
George Mason University
in Partial Fulfillment of
The Requirements for the Degree
of
Doctor of Philosophy
Electrical and Computer Engineering

Committee:

_____	Dr. Nathalia Peixoto, Dissertation Director
_____	Dr. Joseph. Pancrazio, Committee Member
_____	Dr. Qiliang Li, Committee Member
_____	Dr. Liansheng L. Tang, Committee Member
_____	Dr. Andre Manitius, Department Chair
_____	Dr. Kenneth S. Ball, Dean, Volgenau School of Engineering
Date: _____	Summer Semester 2013 George Mason University Fairfax, VA

Characterization and Modeling of Conductive and Insulating Coatings for Neural Interfaces

A Dissertation submitted in partial fulfillment of the requirements for the degree of Doctor of Philosophy at George Mason University

by

Saugandhika Minnikanti
Masters of Science
George Mason University, 2007

Director: Nathalia Peixoto, Professor
Department of Electrical and Computer Engineering

Summer Semester 2013
George Mason University
Fairfax, VA

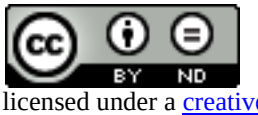
This work is licensed under a creative commons attribution-noderivs 3.0 unported license.

DEDICATION

This is dedicated to my loving husband Vamsi Ivaturi who encouraged me to pursue my PhD and supported me throughout with patience, to my parents M.V.A Sarma and M. Lalitha Sarma for their endless help, support, and guidance and to my in-laws Eswar Ivaturi and Dr. Bala Ivaturi for their patience and encouragement. To my dearest brother Dr. M. Venkatachala Sarma who has always been my inspiration and pride and my daughter Radhika for making it all worthwhile. Last but not the least all my dear friends who believed and encouraged me all this while.

ACKNOWLEDGEMENTS

I would like to express my sincere gratitude to my advisor Dr. Nathalia Peixoto for constant inspiration, encouragement, and help beyond academic guidance. My neural engineering lab mates for creating an enriching amicable work environment and the help. Finally, thanks to Dr. Joseph J. Pancrazio for his guidance, backing and patience.

TABLE OF CONTENTS

LIST OF TABLES

Table Page

LIST OF FIGURES

LIST OF ABBREVIATIONS

Accelerated Lifetime Testing.....ALT
Activated Iridium Oxide Films.....AIROF
Atomic Layer Deposition..... ALD
Carbon nanotubes.....CNT
Charge Storage Capacity anodic..... CSCa
Charge Storage Capacity cathodic..... CSCc
Chemical Vapor Deposition.....CVD
Cyclic Voltammetry.....CV
Electrochemical Impedance Spectroscopy .....EIS
Electrodeposited Iridium Oxide Films.....EIROF
Electrophoretic Deposition .....EPD
Glial Fibrillary Acidic Protein ..... GFAP
Inductively coupled plasma atomic emission spectrometer..... ICP-AES
Interdigitated Electrodes ..... IDEs
Interleukin.....IL
Mean Time to Failure.....MTTF
Multi Walled Carbon Nanotubes ..... MWCNT
Phosphate Buffered Saline..... PBS
Reverse Transcriptase-Polymerase Chain Reaction .....RT-PCR
Scanning Electron Microscope ..... SEM
Sputtered Iridium Oxide Films ..... SIROF
Thermally deposited Iridium Oxide Films.....TIROF
Toll like Receptor2 .....TLR2
X-ray Photon Spectroscopy ..... XPS

ABSTRACT

CHARACTERIZATION AND MODELING OF CONDUCTIVE AND INSULATING COATINGS FOR NEURAL INTERFACES

Saugandhika Minnikanti, M.S.

George Mason University, 2013

Dissertation Director: Dr. Nathalia Peixoto

Neural interfaces are engineered with implantable electrodes that are key in forming efficient connection between the brain and a machine. The implantable electrodes are essentially a combination of exposed conductive regions and passivated coatings. The conductive coatings act as sensors or stimulators while the insulation encapsulates the conductive tracks and device to provide protection against the harsh *in vivo* environment. For efficient design of implantable electrodes it is important to understand the factors affecting the interface of conductive coatings and neural tissue. Assuming the conductive materials are noble and corrosion-free, the reliability of the device would highly depend on the long term stability of the encapsulation. While the efficiency metric is different for conductive and insulating materials, in both cases electrochemical impedance spectroscopy and equivalent circuit model fitting can be used to diagnose their performance. This thesis is a culmination of experimental and modeling

work performed on implantable conducting and insulating coatings for neural interfaces. For conductive coatings (iridium oxide and carbon nanotubes) the goal was to characterize the difference between *in vitro* and *in vivo* performance. For insulation (Parylene C and Al_2O_3-Parylene C) the aim was to estimate the mean time to failure and to understand the modes of failure.

The immediate transition between *in vitro* to an *in vivo* environment did not affect the electrochemical properties of the carbon nanotube electrodes. In well controlled, low frequency stimulation acute experiments, we show that multi-walled carbon nanotube electrodes maintain their charge carrying capacity and impedance *in vivo*. We also report on the transcription levels of the pro-inflammatory cytokine IL-1β and TLR2 receptor as an immediate response to low frequency stimulation using RT-PCR. We show here that the IL-1β is part of the inflammatory response to low frequency stimulation, but TLR-2 is not significantly increased in stimulated tissue when compared to controls.

Iridium oxide, unlike carbon nanotubes, demonstrated changes in its electrochemical characteristic *in vivo* and its performance was also dependent on low frequency stimulation. A 30% decrease in *in vivo* CSCs was observed, and an increase in impedance for all electrodes. For low frequency stimulated electrodes, increase in impedance was observed in the low and high frequency spectrum. While the un-stimulated group impedance increased across the spectrum. Two equivalent circuit models were used to explain this difference. An increase in charge transfer resistance and diffusion impedance was observed. These changes reflect a modification in the double layer composition due to electro-bio-chemical interactions occurring *in vivo*. Here we discuss relevant

considerations when using *in vitro* models to predict the performance of implantable electrodes for deep brain stimulation and for recording of neurophysiological signals. A critical factor for an implanted insulation's performance is its barrier properties that limit access of biological fluids to the underlying device/metal electrode. Here we report a comprehensive study to examine the mean time to failure of Parylene C and Al_2O_3-Parylene C coated devices using accelerated lifetime testing. Samples were tested at 60 °C for up to 3 months while performing electrochemical measurements to characterize the integrity of the insulation. The mean time to failure for Al_2O_3-Parylene C was 4.6 times longer than Parylene-C coated samples. In addition, based on modeling of the data using electrical circuit equivalents, we show here that there are two main modes of failure. Our results suggest that failure of the insulating layer is either due to pore formation or blistering as well as thinning of the coating over time. The enhanced barrier properties of the bilayer Al_2O_3-Parylene C over Parylene C makes it a promising candidate as an encapsulating neural interface.

CHAPTER 1: INTRODUCTION

1.1 Thesis Organization

This thesis presents the design, characterization, and modeling of conductive and insulating coatings of implantable devices. For conductive coatings (iridium oxide and carbon nanotubes) the goal was to characterize the difference between *in vitro* versus *in vivo* performance. While for insulation (Parylene C and Al_2O_3-Parylene C) the aim was to estimate the mean time to failure and understand to the modes of failure. The performance in both scenarios is essentially evaluated via electrochemical characterization and fitting equivalent circuit models to the impedance spectra. Additionally, we discuss the characterization of early biological response to implanted carbon nanotube microwires with low frequency stimulation.

This thesis is organized in seven chapters. Chapter 1 describes briefly the world of neuroprosthetics with few examples of current applications for treating various disorders. The focus moves onto introducing two essential challenges of neuroprosthetics, understanding the difference between conducting electrode-electrolyte and tissue interface as well as the long term stability of the insulation/encapsulation materials. Chapter 2 starts with the material requirements of conductive and insulating coatings of neural electrodes. Then we present background information on carbon nanotubes, iridium oxide and parylene C. As the major work of this thesis involved developing equivalent

circuit models for the measured impedance spectra, Chapter 3 is dedicated to explaining electrochemical impedance spectroscopy and to the theory behind equivalent circuit models. Chapter 4 reports the methodology adopted for the experiments conducted during this thesis. This includes materials and procedure to prepare the tested electrodes, *in vitro* and *in vivo* electrochemical characterization, biological response towards carbon nanotube electrodes, age acceleration of tested insulation as well as details of statistical methods adopted are discussed. Chapter 5 gives an overview of experimental results with interleaved discussions of the *in vitro* and *in vivo* tests performed for low frequency voltammetry stimulated versus controls of electrodeposited iridium oxide coated microwires. The performance is evaluated by discussing the charge storage capacity, impedance spectra and equivalent circuit models. Chapter 6 provides with overview of experimental results with interleaved discussions of the *in vitro* and *in vivo* electrochemical characterization of multiwalled carbon nanotubes coated microwires. The performance is evaluated by the charge storage capacity, impedance spectra and equivalent circuit models. The initial biological response towards these electrodes implanted in an acute study in rodents is also reported. Chapter 7 gives an overview of experimental results with interwoven discussions of the age accelerated tests performed to evaluate the mean time to failure of insulation Parylene C and Al_2O_3-Parylene C on interdigitated arrays. Finally, Chapter 8 Provides with a brief conclusion of the results obtained in this study of characterizing conductive and insulation coatings for neural interfaces.

1.2 Introduction

Neural implants are engineered units that stimulate or sense the electrical activity from the neural tissue (Troyk and Cogan 2005). Their functionality can be divided into two major areas: modulators and prosthetics. As modulators they alleviate symptoms of neurological disorders by activating or suppressing abnormal neural activity either by chemical or electrical intervention. Examples of neuro-modulators are deep brain stimulators for alleviating the symptoms of Parkinson's disease via deep brain stimulation, where microelectrodes are placed in regions of the brain called thalamus, sub-thalamic nucleus, and globus pallidus (Vitek 2002). Deep brain stimulation to treat Tourette syndrome (Servello et al. 2008), obsessive compulsive disorder (Figee et al. 2013), chronic pain (Levy, Lamb, and Adams 1987), drug resistant depression (Mayberg et al. 2005) are under clinical trials. While, deep brains stimulation is emerging as treatment option for epilepsy (Velasco et al. 1995) and Alzheimer's disease (Laxton et al. 2010). Prostheses on the other hand restore the lost function of the body by bypassing the disabled region of the nervous system. Brain Gate™ a neural interfacing system connecting the brain of a quadriplegic patient to a robotic arm (Hochberg et al. 2012), motor implants for grasp restoration (Ethier et al. 2012), cochlear (Wilson et al. 1991) and retinal (Hornig et al. 2005) implants are examples of neuro-prosthetics. Neural stimulation activates or suppresses the neuronal activity while neural recordings help in decoding the intent of the disconnected brain region and using those signals to control a prosthetic device. They also are beneficial in building adaptive and patient-tailored, closed loop system.

Both conductive and insulating materials play a critical role in implantable devices. The conductive materials as sensors or stimulators while the insulation as encapsulations of electrical circuitry. Being a medical device, any material used for developing neural devices need to meet certain set requirements such as biocompatibility, structural integrity, and smaller dimensions. Apart from these requirements it is essential to understand the bi-directional influence of the interfacial interaction of the electrode-biotic interface (Merrill, Bikson, and Jefferys 2005) (Cogan 2008). The fundamental process occurring at this electrode-biotic interface is charge transduction between electrons of the electrode and ions present in the neural tissue. Another important concern for neural interfaces is the long term stability of implantable conductive as well as insulating coatings. These factors directly impact the efficiency and reliability of neural electrodes. Assuming that the noble metals and corrosion resistant coatings do not degrade over time *in vivo*, their long term stability for intended use would mostly rely on the insulation coatings to maintain their barrier properties.

The performance of both insulation and conductive coatings can be evaluated by electrochemical characterization via cyclic voltammetry (CV) and electrochemical impedance spectroscopy (EIS). CV measures the maximum charge that the electrode can deliver. This information is essential in evaluating electrodes used for electrical stimulation of tissue. EIS measures system response for a small amplitude, periodic AC signal spanned across a range of frequencies (Lasia 1999). EIS is an extremely useful tool for characterizing the electrochemical interactions occurring at the electrode-electrolyte interface and for material characterization at the surface (Macdonald 1991). It not only

shows the voltage-current behavior of the electrode in the electrolyte but it provides information on the way the impedance of an electrode varies for a chosen frequency range. Equivalent circuit models are fit to the EIS data to interpret the interface in simple electrical terms (Macdonald 1992). Impedance data are often represented in Nyquist formats accompanied by Bode representation (Macdonald 1992).

Mostly, initial investigations for electrode coatings understandably begin with an *in vitro* assessment. Models are developed to explain the *in vitro* performance and are usually used as predictors for *in vivo* scenarios. **The important question is how well do the *in vitro* models represent the *in vivo* scenarios? How relevant are the *in vitro* parameters when the interface changes *in vivo*? Is it dependent on the type of material used for electrode, frequency range of measurement or on the stimulation protocol?** Here we answer these questions using models developed to fit the *in vitro* and *in vivo* EIS data on two different materials, iridium oxide and carbon nanotubes. The iridium oxide used in this study was electrodeposited using a protocol adapted from (Meyer et al. 2001), while carbon nanotubes microwires were fabricated using protocol developed during the author's Master thesis (Minnikanti, Skeath, and Peixoto 2009a). Iridium oxide impedance has been previously shown to vary with current pulsing (Weiland and Anderson 2000). Thus we wanted to test if a slow cycle CV (50 mV/s) stimulation usually used to assess the charge storage capacity of electrode *in vivo* impacts the impedance of iridium oxide electrodes. Thus stimulated versus un-stimulated iridium oxide electrodes were investigated for our *in vitro* versus *in vivo* scenarios.

No matter how well we understand the changing interface or how exceptional the electrical or mechanical property of the conductive material, it will not function effectively for its intended use if its encapsulation fails. Microwires array typically fail after 18 months (Nicolelis et al. 2003) after implantation. While device performance depends on the tissue-response (Polikov, Tresco, and Reichert 2005), there is a growing recognition that device materials may not withstand exposure to the harsh ionic environment *in vivo* (Prasad et al. 2012). Fortunately, techniques as accelerated life time testing reduce the time required to predict the survivability age of a material (Meeker, Escobar, and Chan 2000). Materials are put under a stress that accelerates their failure compared to their normal life-time. The key here is to keep the same mechanism of failure in both accelerated and normal conditions (Bierwagen et al. 2003). The time to failure under the stress is evaluated by tracking the changes in properties due to the chosen duress (Bierwagen et al. 2003). One of the methods to induce stress is to elevate the temperature of the simulated normal life in situ environment. The rationale behind using an elevated temperature is the assumption that an increase in temperature increases the rates of chemical reactions, diffusion and molecular mobility (Meeker, Escobar, and Chan 2000). An estimate of life time is evaluated by extrapolating the results of mean time to failure (MTTF) of a thermally aged material to that of normal life operating temperature of the material. The test temperature needs to be below the glass transition of the material to avoid the occurrence of false failure (Li et al. 1998).

In this thesis Parylene C and atomic layer deposited-Al_2O_3 Parylene C encapsulation lifetimes were investigated under accelerated aging conditions in

phosphate buffered saline (PBS) at pH 7.4 to closely mimic the brain. A widely used encapsulation layer for implantable devices is Parylene C [poly(dichloro-p -xylylene) has been shown to fail (Hassler et al. 2010) as an encapsulation material. In an effort to improve encapsulation performance (Xie et al. 2012) recently reported a bi-layer encapsulation scheme which combines atomic layer deposited (ALD) Al_2O_3 followed by Parylene C. Thus an independent study was carried out on Parylene C and ALD-Al_2O_3 Parylene C coated interdigitated electrodes, to estimate the mean time to failure of each coating. Electrochemical methods including EIS, DC leakage current analysis and CVs on coated interdigitated electrodes were used to monitor electrochemical correlates of insulating layer integrity. Equivalent circuit models were developed to fit the impedance spectra of coated interdigitated structures to understand the modes of failure occurring in the insulation coating.

CHAPTER 2: BACKGROUND

2.1 Neural Electrodes

An ideal invasive electrode used for stimulation or recording should be small, so that there is minimal tissue damage, and it should have enough recording sites for monitoring many neurons simultaneously. These electrodes can be made of various substrates such as platinum, medical grade stainless steel, iridium and silicon (Schmidt, Bak, and McIntosh 1976)(Ashby et al. 1999)(Boockvar et al. 2000)(Rezai et al. 2002)(Hochberg et al. 2012). The electrode is the interface between the body and the prosthetic device used for electrophysiological research. One side is the metal electrode attached to an electrical circuit: here electrons are the charge carriers. The second side is the physiological medium (electrolyte) where charge is carried by ions. The fundamental process occurring at the electrode-electrolyte interface is charge transduction between electrons of the metallic electrode and ions of the electrolytic species (Merrill, Bikson, and Jefferys 2005). The two basic mechanisms of charge transfer at the electrode-electrolyte interface are Faradaic and non-Faradaic (Varma and Selman 1991; Bard and Faulkner 2006), as briefly discussed below. When reduction and oxidation of chemical species in the electrolyte takes place during electron transfer to and from the electrode then this is called Faradaic charge transfer. During reduction an electron is added to the chemical species and this occurs when the electrode is driven to negative potentials. In

oxidation, removal of an electron from the chemical species occurs when the electrode is driven to a positive potential in reference to the solution. For example, a typical example of a Faradaic charge transfer is the process at the surface of silver-silver chloride electrodes. This mechanism injects redox products in solution. In a reversible charge transfer the redox species injected into the electrolytic media are recovered at the electrode surface when the direction of current is reversed.

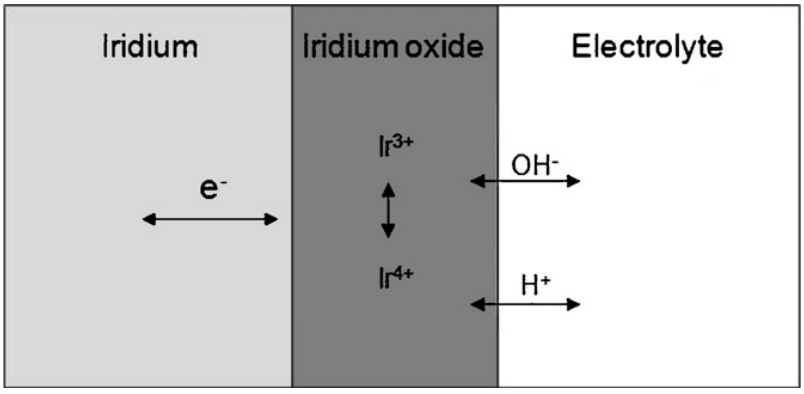

Figure 2.1: The charge transfer of activated iridium oxide is an example of a Faradaic process involving transfer of electron from the iridium film to counter ions in the electrolyte. (fig ref:(Yoo et al. 2013))

Iridium oxide investigated in this study transfers charge via a reversible Faradaic process (Meyer et al. 2001). The reduction and oxidation of the iridium oxide film is due to the valence transition from Ir^{3+} to Ir^{4+} with charge balance provided by the counter ions in the solution (H^+ and OH^-) (figure 2.1) (Cogan 2008). Thus, the capacity of iridium

oxide films to inject charge is highly dependent on the availability of the counter ions in the media (Cogan 2008).

Charge redistribution can also occur by charging and discharging of the double layer present at the electrode-electrolyte interface. The double layer acts like a capacitor, with the metallic electrode as one plate and the other being the electrolyte/tissue (Guyton and Terry Hambrecht 1974).

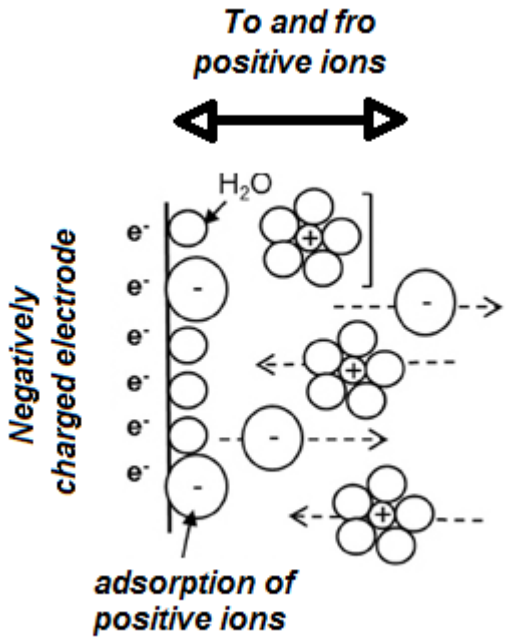

Figure 2.2: Non-Faradaic process involves redistribution of charge in the electrode-electrolyte interface. (fig ref: (Bareket-Keren and Hanein 2013))

Ions from the electrolyte either move towards or away from electrode depending on its charge (figure 2.2). This process doesn't involve actual electron transfer between the electrode and the electrolytic species. Carbon nanotubes are an example of materials that transfer charge via non-Faradaic process as long as they are in their pristine conditions (Barisci, Wallace, and Baughman 2000). Modified carbon nanotubes can present with Faradaic charge transfer depending on the attached functional groups (Barisci, Wallace, and Baughman 2000).

Usually, the charge presented by a conventional metallic electrode through a stimulus pulse is above the holding capacity of the double layer. Thus, the charge transfer contribution of the electrochemical Faradaic mechanism dominates the capacitive non-Faradaic mechanism (Guyton and Terry Hambrecht 1974).

2.2 Requirements of Neural Electrodes

The requirements of implantable electrodes are set by the mechanical, electrical and biochemical interactions between the electrode and the nervous tissue (Merrill, Bikson, and Jefferys 2005). Within these constraints electrodes need to be functional as well as offer reliable stimulating and recording capacity over the lifespan of the implant. A short description on the requirements for neural electrodes is given below. Each figure of merit will be used to describe the value of iridium oxide and carbon nanotube as neural electrode coatings in their respective sections.

2.2.1 Impedance

Impedance is the measure of the opposition towards a passing electric current presented by a system/material. It is an extension of resistance when dealing with AC fields and is the ratio of the applied voltage to the current response. However, unlike resistance impedance is frequency dependent as it accounts for the capacitance that presents with different opposition mechanisms towards electrical currents. Impedance is represented with a magnitude and a phase angle term, where the phase value of 0 and -90° corresponds to system behaving as a pure resistor and capacitor.

Inserting a foreign body into the brain has multiple consequences, one of which is the formation of a encapsulated layer around the implant (Edell et al. 1992)(Biran, Martin, and Tresco 2005). The reactive gliosis creates an insulating layer around the electrode (Polikov, Tresco, and Reichert 2005), thus increasing the apparent impedance between the electrode and the tissue (McConnell, Butera, and Bellamkonda 2009). Thus the insulating layer around an electrode would mean no passage of direct current between the conductive material and the biological tissue. Spatial proximity between the neural electrode and neurons determines how well the signal is transferred. The insulating layer increases the space between the electrode and the neuron (Liu et al. 1999), causing loss in signal. This would decrease their efficiency in recording low voltages and would require higher voltages/current to deliver the same amount of charge for stimulation. This would be harmful to the tissue. As the glial scar increases the interfacial impedance irrespective of the type of electrode, lower impedance of electrodes would in general be beneficial. Also, having lower impedance *in vivo* will maintain high signal-to-noise ratio (SNR)

while measuring small (micro Volts) neuronal signals from the extracellular space (Cogan 2008).

The increase in EIS based studies for neural electrodes has introduced a technique for understanding the electrode-tissue interaction without the need of a biological assay. By correlating the tissue response to impedance behavior (McConnell, Butera, and Bellamkonda 2009), the efficiency and long-term reliability of neural stimulating and recording electrodes can be evaluated and potentially predicted. The interface characteristics and interpretation can then be used to develop novel surface materials for implantation.

An important question is to understand dynamics of the interface when the electrode goes from an ionic solution into the neural tissue. The interacting ECM undergoing a dynamic ionic and cellular re-composition (Kurrat, Prenosil, and Ramsden 1997) due to changing foreign body response also modifies the electrode characteristics (Polikov, Tresco, and Reichert 2005). Published studies usually compare *in vitro* with *in vivo* impedance spectra using the same equivalent circuit model. (Aarts et al. 2008) and colleagues performed EIS prior, during, and after implantation of a three-dimensional probe array based on platinum electrodes. The probe was microfabricated in several steps, including a mounting step that may have led to many non-functional contacts. Furthermore, the reference and counter electrodes used in this study were stainless steel, which adds several variables to the electric circuit equivalent model. An increase in the impedance *in vivo* was observed when compared to the *in vitro* EIS, but the fit provided by the proposed model was judged only based on the modulus of the impedance (no

phase information) and considered to match well with only half of the experimental spectrum. A second example of EIS *in vivo* was conducted by Duan et al. with platinum microelectrodes implanted in the cat cochlea for six months (Duan, Clark, and Cowan 2004). In this case, the increase of the impedance *in vivo* was correlated to anomalous charge transport at the electrode–tissue interface. That increase was related to changes in composition of extracellular fluid adjacent to the electrodes. Duan's study also points out an interesting fact: the complex curve of the impedance spectrum changes behavior depending on the size of the electrode (micro, nano, macro) and on the distance between the working and reference electrodes. This last observation is due to the diffusion layer, and leads to a transmission line model for the impedance. Weiland et al., in 2000, assessed the effect of chronic stimulation of the brain through pitch-fork micro-probes coated with sputtered iridium oxide (Weiland and Anderson 2000). Their analysis is based on EIS and CV performed while electrodes were implanted in guinea pig cortex. They stimulated the tissue with pulses applied through the same micro-probes, and their results show a transient decrease of measured impedance immediately following pulsatile stimulation. They attributed that temporary reduction in impedance to an increase in efficiency of redox reactions at the surface of the sputtered iridium oxide. However, this phenomenon wasn't observed *in vitro* (in phosphate buffered saline), and thus must have been mediated by proteins of aminoacids only present *in vivo*. Similarly to other studies, separate high frequency and low frequency mathematical models were used to analyze the impedance behavior. The data and modeling results revealed that applying charge to the electrode could indeed reduce the impedance of the electrode-tissue system. Lempka

et al in 2009 fit EIS data collected from implanted "scaled down" version of DBS electrodes (Lempka et al. 2009). Two electrodes each with four Pt/Ir contacts were implanted in the thalamus regions of a rhesus monkey. EIS was measured from 0.5 Hz to 10 KHz using a two electrode setup. They fit four different equivalent circuit models to the *in vivo* EIS data. The model with least errors in the low and high frequency range was selected for interpreting the data. The results revealed an increase in the electrode impedance as seen in the semicircular arc of the high frequency range of the Nyquist plot. This high frequency range is associated with proteins adsorption and cell adhesion. They isolated the increase in impedance to cell adhesion rather than protein adsorption by comparing the data to *in vitro* EIS data. The *in vitro* test conducted in phosphate buffered saline-bovine serum albumin solution showed a negligible increase in high frequency impedance data. Here the comparison was not based on fitting a model. The effect of the clinically relevant stimulation showed up as a decrease in the high frequency impedance affecting the tissue. This study didn't compare an *in vivo* model to an *in vitro* as they were interested only in the changes in the composition of the electrode-tissue interface. However, the least error model used consisted of a constant phase element (CPE) to explain not only the electrode-electrolyte interface but the tissue capacitance. CPE is usually used to depict the non-ideal capacitive behavior of metal electrodes due to surface irregularities (Orazem and Tribollet 2008). The authors claim that the physical interpretation of the model is not clear. It is evident that both impedance and charge are affected by the continual cellular and molecular (protein) interactions occurring at the

electrode-tissue interface (Kurrat, Prenosil, and Ramsden 1997)(Polikov, Tresco, and Reichert 2005)(McConnell, Butera, and Bellamkonda 2009).

2.2.2 Mechanical Integrity

The electrode material should maintain its mechanical integrity, which means that the material should not bend, delaminate, or break when passing through tissue. It should withstand movement between the electrode and the tissue after implantation. The material should not degrade if placed in an electrolyte medium for extended periods, under physiological conditions.

2.2.3 Charge delivery and electrical stability

An electrode should be able to deliver sufficient charge through the double layer formed at the electrode-tissue interface to elicit an action potential. The charge delivered should be at a low electrode potential to prevent water electrolysis and damage the tissue (Merrill, Bikson, and Jefferys 2005). For any electrode there is a reversible charge injection limit i.e., the total amount of charge that an electrode can deliver before the electrode potential reaches the water electrolysis potential. Therefore, the reversible CSC of an electrode material should be high enough to deliver sufficient charge before irreversible reactions initiate. The reversible CSC depends upon the electrode material, electrolytic species, and on the stimulation parameters. Even if the electrode material is biocompatible the Faradaic reaction byproducts must not be toxic to the tissue. Also these redox byproducts should not cause damage to the electrode itself.

2.2.4 Water window

The potential window is defined as the voltage range above which irreversible electrochemical reactions take place. This is commonly used to evaluate the quality of the electrode material. Electrode materials can be tested in any solution of interest. However, in the case of a biological electrode the working potential window should be well within the water window limits (Brummer and Turner 1977)(Merrill, Bikson, and Jefferys 2005). The reason for that is the presence of water in biological tissue. A water window is defined as the potential region between the oxidation of water to form oxygen and the reduction of water to form hydrogen, which is ± 1.21 V (Zoulias et al. 2004).

2.2.5 Surface topology

Surface topography can influence the growth and orientation of neurons in culture. Surfaces having nanofeatures have been shown to influence cell attachment and can be used to navigate cells to a specific region on the silicon substrate (Craighead et al. 1998; Shein et al. 2009; Khang et al. 2007; Sorkin et al. 2009).

2.2.6 Biocompatibility

The electrode surface, which contacts the biological tissue, should be biocompatible. Biocompatible means that the material will not induce toxic effects once in contact with the body. Another important quality of the material should be to not cause excessive immune response. Once an electrode is implanted it will be treated as a foreign material by the body, but the material should not impact the immune system dramatically

(Polikov, Tresco, and Reichert 2005). This kind of response would reduce the electrode charge delivery capacity and recording sensitivity (Williams et al. 2007).

2.3 Iridium Oxide

Iridium oxide is a robust coating material for stimulating neural electrodes owing to its high charge delivery (Cogan 2008), low impedance (Cogan 2008), and biocompatible nature (Eick et al. 2009)(Göbbels et al. 2010). Its basic charge transfer mechanism is via a Faradaic reaction with the highest charge injection capacity amongst the current options of coatings (Cogan 2008; Negi et al. 2010).The following sub-section will briefly discuss various modes of depositing iridium oxide films on substrates, relevant properties as neural electrode coatings, and examples related to using iridium oxide based electrodes.

Iridium belongs to the group of platinum transition metals. It is known for its high corrosion resistance and biological inertness (Lee et al. 2003). The interesting property of iridium is that a multilayer oxide film forms on a substrate as its potential is cycled (Robblee, Lefko, and Brummer 1983). This process is known as “activating Iridium” and the coating is known as iridium oxide. The thickness, porosity and charge capacity of the oxide layer depends on the number of cycles (Robblee, Lefko, and Brummer 1983). The basic mechanism of charge transfer is reversible Faradaic process involving valence transitions between Ir^{3+} /Ir^{4+} within the oxide layer (Hüppauff and Lengeler 1993) and H^{+}, OH^{-} , Na^{+}, Cl^{-} as balancing counterions (figure 2.4) (Cogan 2008).

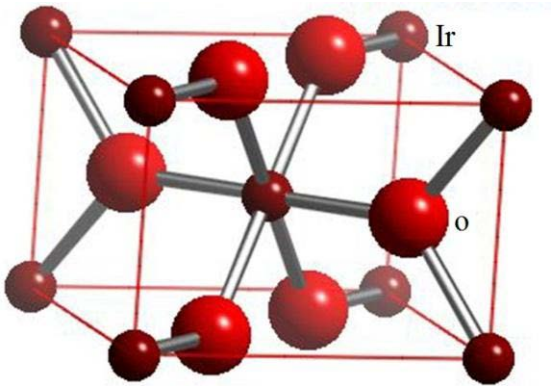

Figure 2.3: Iridium oxide stoichmetric crystal strucutre
(fig ref. http://www.webelements.com/compounds/iridium/iridium_dioxide.html)

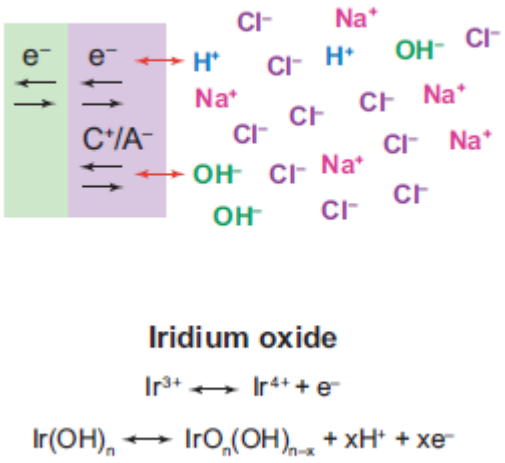

Figure 2.4: Counter ions involved in the charge injection process of iridium oxide. (fig ref:(Cogan 2008))

Iridium has an oxidation state of 4 in its crystal structure of rutile, i.e., a primitive tetragonal unit cell (figure 2.3). The reactions involved at iridium oxide surface depend on the H^{+} and OH^{2-} ion making its potential pH-dependent. Thus, iridium oxide films are being investigated as a material for pH sensing (Elsen, Monson, and Majda 2009). Iridium oxide falls in the category of "super Nernstian behavior", where it exhibits a pH-dependent potential > - 59 mV/pH-unit (Elsen, Monson, and Majda 2009).

A variety of electrode structures of neural interfaces have been coated with iridium oxide. The silicon based Michigan probes (Weiland and Anderson 2000) microwires (Andre et al. 2009) as well Utah electrode arrays (Negi et al. 2010) have been coated with iridium oxide and investigated as retinal (Cogan 2006) or cortical (Han et al. Feb.)(Kane et al. 2013) implants in animal models.

2.3.1 Iridium Oxide depositions for neural electrodes

There are two modes of deposition of iridium oxide depending on the substrate being the parent (Iridium) (Cogan 2008). Iridium based substrates work on the principle of activating the iridium surface by electric potential cycling or by sputtering. While for non-iridium substrates can be deposited with an oxide layer by using iridium salts based electrolytes (Yamanaka 1989). The commonly used methods of both categories are discussed below with examples of neural electrodes tested in *in vitro* or *in vivo* scenarios.

Activated iridium oxide films (AIROFs): Activating the iridium surface by varying its potential (Mozota and Conway 1981; Robblee, Lefko, and Brummer 1983) to form iridium oxide films was developed around in 1980s. Not only was it useful due to its corrosion resistance (Johnson and Hench, 1977), it was also investigated as a material

for display devices (Gottesfeld and McIntyre, 1979). The process involves electrochemical activation of the iridium substrate by electric fields induced by potential cycling, while the charge is compensated by the hydrogen and hydroxyl ions in the electrolyte, eventually forming a hydrated oxide layer.

The choice of electrolyte could vary from an acidic medium as sulphuric acid (H_2SO_4-1N) or a basic media as phosphate buffered saline (PBS) at (pH 7.4). AIROF films surface topology consists of hydrous nano-pores with a density lower by 20 % compared to the crystalline iridium oxide (11.2 g/cm^3) (Cogan et al. 2009). These films exhibit a super Nernstian behavior of -70 to -90 mV/pH-unit, suggesting that the other cations (Li^+, Na^+) as well as the H^+ and OH^{-2} are involved in its redox processes (figure 2.4) (Birss and Pickup 1988). Compared to platinum the charge transfer capacity of AIROF is larger by 5 times (Cogan 2008), however, its charge injection capacity is dependent on the applied positive bias (Cogan et al. 2009). The AIROFs on active iridium sites of neural interfaces have been used in a number of studies (Schuettler et al. 2002)(Hu et al. 2012; Yoo et al. 2013).

Sputtered iridium oxide films (SIROFs) is acquired via reactive sputtering (DC or RF) of an iridium target in an oxidizing plasma environment (Cogan 2009). Usually a reactive gas mixture of argon, oxygen and hydrogen is employed to produce SIROF on the parent metal. The deposited film contains a combination of $Ir^{3+/}Ir^{4+}$ reduction-oxidation state. The morphology and properties of the SIROF depends on parameters such as sputtering gas, pressure as well as the bias applied to the substrate (Negi et al., 2009). Sputtering leads to anhydrous dense crystalline oxide structures with densities

approximately 7.8 g/cm^3.These films are denser compared to AIROF (Negi et al. 2010) containing narrower pores, thus, the ionic transport in SIROF films is restrictive to smaller counter-ions compared to AIROF films (Steegstra and Ahlberg 2012). These characteristics give SIROF a lower resting potential that is near-Nernstian pH dependent (–58 mV/pH-unit), suggesting only hydroxyl and hydrogen ion as being dominant during oxidation and reduction of the films (Cogan et al. 2004)(Cogan et al. 2009). Regardless, SIROF presents with charge storage capacity similar to AIROF but maintains a greater charge capacity without bias. The process also allows for thicker iridium oxide films unlike AIROF. SIROF deposited planar multi electrode arrays were used successfully to record multiple single-unit spike activity from brain slices of train neo-cortex (Gawad et al. 2009).

Thermal decomposition of iridium salt solutions (TIROFs) involves thermal decomposition of iridium salts applied on the surface of a substrate (Cogan 2008). The temperatures involved are greater than 300 °C (Meyer et al. 2001). Its charge capacity is lower than SIROF and multiple depositions of TIROFs are required to attain levels required for neural stimulation. Owing to its high temperature the formed films have lower hydration with densities larger than AIROF and EIROF (Cogan 2009).

Electro-deposition iridium oxide films (EIROFs) are formed when a metallic substrate is immersed in an iridium salt containing aqueous solution while the electric fields are generated either by galvanostatic (Yamanaka 1989) or potentiostatic pulses (Baur and Spaine 1998). The setup involves an electrochemical cell with a three or two electrode setup. The electrolyte is the iridium salt solution and the working electrode

being the substrate of interest. Unlike AIROF and SIROF, iridium oxide can be directly deposited on a non-iridium substrate. The commonly used solutions are acidic sulfatoiridate complex solution (pH 0.9) (Yoshino, Baba, and Arai 1987) and an alkaline iridium tetrachloride (IrCl) solution (Yamanaka 1989). The potential or current between the working and the reference electrode is pulsed repetitively or in addition is swept for a cyclic growth of oxide film. The protocol used in the thesis that involves a potentiostatic pulsing and cycling adapted from Meyer et al 2001. In brief, the potential is swept between 0 to 0.55 V and back at 50 mV/s for 50 cycles, followed by 1600 cycles of a 1 Hz square wave, between 0 and 0.55 V. The sequence formed by the triangular and square waves constitutes one deposition cycle. EIROF has density similar to AIROF with its structure being, porous and hydrated as well. Its pH potential dependence and the reduction and oxidation of EIROF are similar to AIROFs (Cogan et al 2009). It has been suggested that the pulse and sweep potential method creates narrower pores in the EIROFs. This could impede the hydrogen ion diffusion through the film (Thanawala et al. 2008). As the deposition is independent of the parent material, EIROFs is flexible in terms of choice of substrate material and dimension However, the quality of the film varies from substrate to substrate (Negi et al 2009). Thus potential pulsing and sweeping parameters need to be optimized for proper adherence depending on the substrate. For example, Au substrates require constant repetitive pulse potential, while Pt, PtIr and stainless steel require a pre-layer-triangular potential waveform before the standard pulse deposition protocol (Elsen, Monson, and Majda 2009). Another advantage of EIROF is that doesn’t need an extra procedure to activate the film.

2.3.2 Properties as implantable neural electrode material

Each figure of merit described in section 2.2 is described below for iridium oxide coatings developed for neural electrodes.

Impedance

The impedance of a metallic substrate (iridium or non-iridium) lowers considerably over a wide frequency spectrum after iridium oxide deposition (Cogan 2008). The phase in the impedance spectra is usually resistive (closer to 0 degree) for iridium oxide. For example, the phase of impedance for planar AIROF is closer to 0º in the frequency range of 50 Hz to 50 kHz in PBS. While, the measured impedance phase for iridium was closer to -90° (~ capacitive) across the measured frequency spectra (Yoo et al. 2013).

For iridium oxide films the low frequency impedance is dependent on the buffer capacity and the high frequency impedance is dependent on the conductivity of the electrolyte (Cogan et al. 2007). The high frequency impedance increases with decreasing ionic conductivities (figure 2.5) and reduced buffer capacity increases impedance in the lower frequency (< 1 Hz) (figure 2.6). Reduced buffer capacity means lower H^+ and OH^- ions available for the charge transfer reaction for iridium oxide films (Cogan et al. 2007).

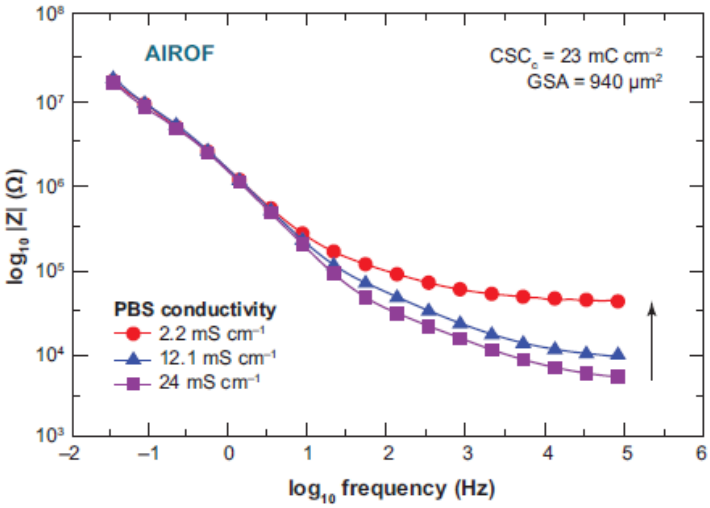

Figure 2.5: Impedance of an activated iridium oxide coated microelectrode measured in phoshphate buffered saline (PBS) with varying in ionic conductivities while the buffer capacity was constant. The geometric surface area (GSA) of the AIROF electrode was 940 µm^2. The high frequency impedance is shown to increase with decreasing conductvity of the electrolyte (fig ref: (Cogan 2008)).

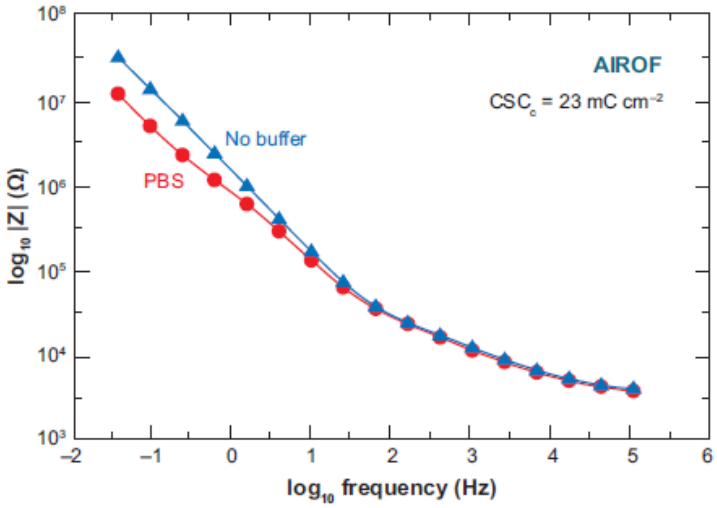

Figure 2.6: Impedance of an activated iridium oxide coated microelectrode measured in phoshphate buffered saline (PBS) and unbuffered saline (no buffer) of similar ionic conductivities. The low-frequency impedance decreases with increase in buffer capacity due to increasesd availability of H^+ and OH^- counterions in the electrolyte (fig ref:(Cogan 2008)).

Mechanical Integrity

The mechanical properties of iridium oxide are inferior compared to its parent iridium metal (Yoo et al. 2013). The films integrity decreases with increasing the thickness of the formed oxide. The mechanical integrity also depends on the applied potential pulses and delaminates over 0. 6 V (Cogan 2008).

Charge delivery and electrical stability

The charge delivery mechanism of iridium oxide is primarily via a reversible Faradaic redox reaction and thus is higher than other noble metals. The redox reaction involves transition between the states of Ir^{3+} to Ir^{4+} in the iridium oxide film (Hüppauff and Lengeler 1993), while counter-ions present in the electrolyte move through the film for charge balance (Cogan 2008). Increasing the electrode potential drives the iridium oxide to a higher valence state by ejecting protons into the electrolyte (Cogan 2008). Thus, its charge injection capacity depends on the applied potential and is greater for positive biases (Cogan 2009). The maximum safe charge injection capacity of iridium oxide electrodes is 3 mC/cm^2 (Cogan 2008) while for a platinum electrode it is a mere 0.4 mC/cm^2 (Cogan 2008). CVs of AIROF electrodes contain two prominent current peaks at 0.25 V (Ir^{3+}) and −0.21 V (Ir^{4+}) , while SIROF presents with two reduction (+ 0.2, − 0.4V) and oxidation (− 0.1, + 0.45 V) peaks (figure 2.7). In contrast, the parent iridium exhibits roughly a rectangular shape (Cogan 2008).

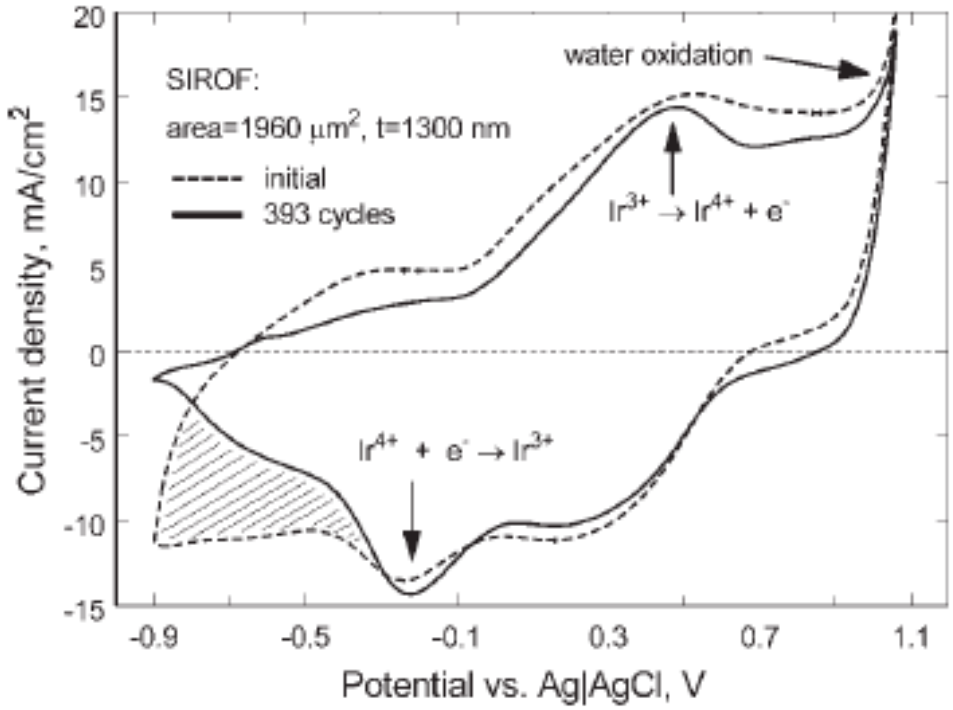

Figure 2.7 Typical cyclic voltagram (dashed line) of a sputtered iridium oxide film with clear redox peaks. Water oxidation is clearly visible at 1.05V. A decrease in the voltagram area is seen at potential -0.2 to -0.9 V after 393 cycles (solid line) (fig ref: (Cogan 2008))

Iridium oxide films charge injection capacity is independent on the buffer concentration and but is proportional to the ionic conductivity of the electrolyte (Cogan 2008). Our group has shown previously that non-pulse stimulated EIROF electrodes maintained their CSCc over a long immersion time in room temperature PBS compared to PEDOT electrodes (Peixoto et al. 2009). However, the CSCc is shown to decrease if the films are continuously pulsed with potentials (Weiland and Anderson 2000; Cogan et

al. 2004) or continuous CVs cycles (393) at 50 mV/s between –0.9 V and 1.05 V versus Ag|AgCl (Cogan 2008).

Water Window

The maximum potential range for iridium oxide is -0.85 V to 0.8 V, beyond these limits delamination of the film as well as hydrolysis of water occurs. At potentials less than −0.85 V AIROF films delaminate (Cogan et al. 2004). SIROF maximum potential range seems to fall within − 0.64 to 0.75 V versus saturated calomel electrode (Kevin Wang, Liu, and Durand 2009).

Surface topography

Iridium oxide morphology comprises of almost circular nodules with diameter ranging from 200 - 400 nm (Cogan et al. 2009). The packing density of the nodules depends on the mode chosen for iridium oxide formation. As the thickness of the oxide layer is increased the nodular structure is observable (Cogan et al. 2009).

Biocompatibility

Iridium oxide electrodes have been tested for stimulating various brain regions in animal models for spinal cord (Woodford et al. 1996), cochlear nucleus (Han et al. 2012), and the cortex (Kane et al. 2011). Iridium oxide coated microelectrode has been used for stimulating the human cortex in a clinical study (Kennedy et al. 2004). Han et al (2012) studied the chronic impact of silicon-based arrays coated with EIROF on Au for stimulating the cochlear nucleus. The histopathology results of neurons and astrocytes

show low levels of alterations in the tissue structure after chronic implantation and show only a localized inflammation around the probes.

Drawbacks

As the charge delivery mechanism is Faradaic based, it has the potential of generating toxic by-products if the voltages or currents exceed the reversible potential region. Additionally, the utilization of protons for electro-neutrality during iridium oxide redox reactions can induce local pH changes at the electrode-tissue interface (Elsen et al 2009). Also, iridium oxides impedance and charge storage capacity are dependent on the buffer capacity and conductivity of the media (Cogan 2008). There is a limit to activating the iridium to form iridium oxide films as continuous movement of ions creates a volume induced stress in the iridium oxide film (Cogan 2008). For example, the maximum achievable CSCc for AIROF and EIROF CSCc is 80 mC/cm^2 and 180 mC/ cm^2 before delamination occurs (Negi et al 2009). The instability of iridium oxide film due to long-term pulsing (Venkatraman et al. 2011) is its biggest challenge towards its application as a stimulating electrode material. AIROF and EIROF can deliver charge within the water window as long as the pulses are below 200 us at 0 Hz and the charge delivered is 1.2 mC/cm^2, though larger than limit for platinum (80 uC/ cm^2) (Cogan 2008).

2.4. Carbon nanotubes

Carbon nanotubes (CNTs), known since 1950 (Monthioux and Kuznetsov 2006) were rediscovered in 1993 (Iijima and Ichihashi 1993). They are known for ballistic conductance, chemically inertness (Niyogi et al. 2002), nano size (Ajayan 1999) and

chemically functionalized with ease (Shim et al. 2002; Sinnott 2002). All these properties elected them as the next generation biomaterial(Malarkey and Parpura 2007) (Malarkey et al. 2009). CNTs winning feature for neuroscientists was its diameter matching the dimensions of neuronal processes. Possible interaction at a molecular level, to form "functional neuronal circuits" (Lee and Parpura 2009), and bio-molecule functionalization (Mattson, Haddon, and Rao 2000) allowed ways for molecular control of neuronal architecture at focal microdomains. These factors made CNTs as an interesting candidate towards neural interfacing applications (Pancrazio 2008).

CNT is the fifth allotrope of solid state carbon. The structure consists of a hexagonal carbon sheet (graphene) rolled up into cylinders at nanometer scale (Ajayan 1999). The hexagonal network of carbon atoms are sp^2 bonded and the electrons are delocalized that are mobile inside and outside the nanotube channel (Dresselhaus et al. 2004). There are two major kinds of carbon nanotubes: Multi Walled Carbon Nanotube (MWCNT) and Single Walled Carbon Nanotube (SWCNT). MWCNTs are concentric cylinders of grapheme sheets around a common central axis with diameter varying from 2 to 25 nm and interlayer spacing between the cylinders around 0.34 nm (Ajayan 1999). While SWCNTs consist of a single graphene sheet rolled up as a cylinder with uniform diameter ranging from 1 to 2 nm (Ajayan 1999). Though the carbon-carbon bond is constant, SWCNTs exhibit metallic or semiconducting nature solely based on its diameter and chirality (Ajayan 1999).

2.4.1 Carbon Nanotubes depositions for neural electrodes

CNT films coated on neural interfaces have been produced by solvent evaporation, electrochemical deposition, chemical vapor deposition (CVD), layer-by-layer assembly, and electrophoresis. Each of these methods deposits CNT films with varying orientation and chemical properties.

In **CVD,** a hydrocarbon gas catalytically decomposes into carbon atoms that grow on seeded metallic (Fe, Ni) catalysts (Cassell et al. 1999) realized on a heated (500 °C to 1000 °C) substrate via standard microfabrication techniques. The substrates are usually silicon, silicon dioxide, quartz and metallic, or any other microfabrication compatible substrate. The substrates are placed in a quartz tube maintained at atmospheric pressure in a flow furnace. The size, geometry, location, quantity, and quality of yield are dependent on the support layer as well as on the metal catalyst (Cassell et al., 1999). Using the CVD technique CNTs have been grown on penetrating platinum-tungsten microwires electroplated with nickel (Ansaldo et al. 2011) and vertically grown on multi-electrode arrays (Wang et al. 2006).

Electrochemical deposition involves co-deposition of CNTs with metals, conductive, and non-conductive polymers. The electrode surface is coated with a charged species is and is placed in a solution containing counter-ion to be deposited. An electric field is applied such that it drives the oppositely charged species to oxidize and reduce on the electrode surface. Co-deposition with CNTs enhances the conductivity, porosity and provides with mechanical integrity. Electrochemical deposition has been used to coat variety of substrates and geometrical shapes for neural interfaces (Keefer et al. 2008).

Electrophoresis was employed to deposit CNTs onto metallic microwires (stainless steel and gold) used in this thesis. Electrophoretic deposition (EPD) occurs as the charged particles move in a suspension and deposit on the electrode surface under the influence of an applied electric field (Van der Biest and Vandeperre 1999). In the case of CNT EPD, the applied field deforms the particle double layer and causes particle coagulation on the substrate (Boccaccini et al. 2006). The coagulation is derived from the Derjaguin-Landau-Verwey-Overbeek theory and is governed by London-Van der Waals forces (Sarkar and Nicholson 1996). For each set of EPD experiments, a DC voltage is applied between a working and reference electrode. The protocol employed for EPD deposition of CNTs used in this thesis is discussed in chapter 4. Successful EPD of MWCNTs on implantable microwires has been previously reported by our group (Minnikanti, Skeath, and Peixoto 2009b).

Layer–by-layer assembly involves alternate adsorption of charged poly-ions to form a thin coating on a substrate. Each adsorption layer consists of a monolayer polyion species. Jan et al. (2009) used MWCNTs in poly(sodium styrene sulfonate) and Poly vinyl alcohol (PVA) as alternate adsorption layers on 400 nm diameter ball Pt/Ir electrode. This method can be used on arbitrarily shaped substrates.

Solvent evaporation involves dispersing CNTs in organic solvents. CNTs are deposited onto substrates as thin films when the organic solvent evaporates (Lovat et al. 2005). **Spray suspension method uses** compressed air to break down an aqueous media into a fine layer of mist that deposit on a heated substrate (Malarkey et al. 2009). These

techniques have not been used to coat implantable NEs, as adhesion and long term stability haven't been characterized yet.

2.4.2 Properties as implantable neural electrode material

Each figure of merit described in section 2.2 is described below for CNT coatings developed for neural electrodes. CNTs are often co-deposited and functionalized with materials such as conductive polymers, metals etc. Thus, performance of these coatings would depend on the properties, stability and integrity of both CNT and the co-existing material.

Impedance

Pristine CNTs have high electrical conductivity, on the order of 108 $\Omega^{-1}m^{-1}$ (Baxendale 2003) and functionalized, non-functionalized CNTs coatings decrease the apparent electrode impedance. PVA/MWCNT coating decreased the impedance of Pt-Ir electrodes (Jan and Kotov 2007). EPD MWCNT on stainless microwires show a decrease in impedance modulus by two orders of magnitude for most of the frequencies tested. Electrochemical (Keefer et al. 2008) as well as CVD (Ansaldo et al. 2011) grown CNTs on microelectrodes have shown a decrease in impedance.

Mechanical Integrity

CNTs are known for their strength with a Young's modulus of a single CNT exceeding 1TPa, about five times stronger than steel (Treacy, Ebbesen, and Gibson 1996). Yet, they are flexible and restore back to their formal shape on removal of

mechanical stress (Salvetat et al. 1999). Both these properties of strength and flexibility are essential for a penetrating electrode coating. Keefer et al (2008) inspected the surface morphology of explanted electrochemically deposited MWCNT electrodes revealed mechanical stability even after penetrating through the dura matter. Care must be taken if CNT are used merely as the last coating on a substrate. The underlying substrates mechanical features could influence the integrity of the CNT coating.

Charge Delivery and electrical stability

The increase in surface area for ion transportation due to an entangled matrix of CNTs over a substrate and the conductivity of the nanotube increases the double layer capacity (Fang et al. 2006). Research has shown that charge transfer of pristine CNT in an electrolytic medium is primarily non-Faradaic (Barisci, Wallace, and Baughman 2000). However, CNTs are often functionalised and co-deposited with other materials and these could induce redox reactions leading to faradaic charge transfer (Barisci, Wallace, and Baughman 2000). A higher CSC was reported for the PVA/MWCNT electrodes in comparison to polyethylenedioxythiophene and iridium oxide having identical thickness (Jan et al., 2009). The CSCc of bare stainless steel electrodes significantly increases after EPD-MWCNT deposition, for example in one case the CSCc increased from 2.18 $\mu C/mm^2$ to 7.15 $\mu C/mm^2$ after deposition (Minnikanti et al. 2010). Some EPD-MWCNT-coated electrodes aged in air at room temperature had enhanced charge delivery capacity. Electrochemically deposited carbon nanotubes showed an increase in the CSCc (Keefer et al. 2008). However, due to instability of

polypyrole(PPy), CSCc of PPy-CNT coatings degraded after extensive periods of standard clinical stimulation pulses (Ansaldo et al. 2011). Thus, stability of CNT coatings is highly dependent on co-deposited materials, its attachment to underlying substrate and deposition method.

Water Window

CNTs "well defined graphitic structure", give it a wide working potential (Hu et al. 2004) well within the water window limit. However, its working potential would highly depend on co-deposition materials, underlying substrate and mechanism of deposition.

Surface Topography

CNT electrodes offer stable networks and strong physical interactions has been observed between the neurons and the CNTs (Sorkin et al. 2009). The neurons move towards CNT covered surfaces and single neurons move particularly towards the CNT surfaces (Galvan-Garcia et al. 2007). The surface topography depends on the mode of deposition. Using CVD technique they can be aligned vertically while other modes produce an entangled matrix of CNTs creating a micro/nano-porous structure.

Bicompatibility

Though CNT surfaces are chemically inert (Niyogi et al. 2002), its biocompatibility is dependent on the deposition method, nanotube size, purification chemical functionalization, and type of administration (Ciofani et al. 2010; Nayagam et

al. 2011). CNT coated surfaces attracted and directed neuronal growth in *in vitro* scenarios (Galvan-Garcia et al. 2007). The immobile CNTs on arrays induced a minor host response while the dislodged CNTs were phagocytosed in male guinea pig muscles (Nayagam et al. 2011). CNTs positive interaction with neurons has been confirmed by various studies (Lovat et al. 2005; Ben-Jacob and Hanein 2008; Keefer et al. 2008; Lobo et al. 2008; Khraiche, Jackson, and Muthuswamy 2009). (Lu et al. 2010) conducted a chronic study on PPy/SWCNT coated platinum wire implanted in rat brains for 6 weeks. They found the GFAP expression lower and higher neuronal density for the CNT coated wires in comparison to the control electrodes. Absence of acute reactive gliosis for flexible CVD coated CNTs on multi electrode arrays implanted in the motor region of a non-human primate (Sauter-Starace et al. 2009) was reported.

Drawbacks

Inherent hydrophobicity of pristine CNTs (Yang et al. 2007) lowers its contribution towards charge transfer in an aqueous media (Wang et al., 2006). Hence, surface modification of nanotubes with cytotoxic organic solvents is done to make them hydrophilic (Lacerda et al. 2006). Thus care must be taken to remove any trapped solvents in and around the porous nanotubes (Wang et al., 2006). The bioavalibality of metallic catalysts used for growing CNTs are of great concern due to its negative affect on the overall tissue health (Guo et al. 2007). Thus employing harsh purification these metal catalysts (Fe, Ni) (Hu et al., 2003) are removed. Both metallic (conductive) and semiconducting (semi-insulating) CNTs grow together as bundles and are hard to

separate (Krupke et al. 2003), this lowers the bulk conductivity of the nanotube coatings. As CNTs are nanostructures and if allowed to be dispersed in cell media or tissue can block and modulate ionic channel behavior, which in turn impacts neuronal characteristics potentially in the long (Park et al. 2003)(Ni et al. 2005; Xu et al. 2009). Thus, it is imperative that CNT coatings are stable and robust during the lifetime of the implant.

2.5 Al_2O_3-Parylene C

Parylene C [poly(dichloro-p -xylylene), is a semi-crystalline polymer and belongs to the familyof thermoplasts known as polyparaxylylene. It is deposited via vapor deposition polymerization process where the dimer is heat vaporized in a vacuum chamber to create gaseous monomer. The gaseous monomer polymerizes on a cooler substrate held in a deposition chamber. Parylene C has several advantageous properties including a low dielectric constant, non-cytotoxicity (Chang et al. 2007) and can be deposited as a conformal pinhole free film, addressing extreme contours as sharp edges and crevices (Ramachandran et al. 2007) characteristics of micromachined devices. Nevertheless, failure of Parylene C as an encapsulation and insulator have been reported (Hassler et al. 2010). In fact, long term *in vivo* measurements with Parylene C coated microelectrode arrays revealed decrease impedance and concurrent bioelectrical signal loss suggesting degradation of the insulating layer (Simeral et al. 2011). Various techniques have been used to investigate the electrical and barrier properties of Parylene C. Literature review shows that the barrier properties of Parylene-C can be improved by

using adhesion promoters (Chang, Lu, and Tai 2011), functionalization (Seymour et al. 2009) and annealing the polymer (Metzen and Stieglitz 2013).

As a popular choice for chronic implantable polymer, ALT of Parylene C on different substrates and structures are being investigated by various groups. (Hara et al. 2012), performed ALT of Parylene C sheath microelectrode array at 80 °C and used EIS to assess the quality of the ageing electrodes. Changes in modulus of impedance with phase shifts were reported and were related to probable delamination of Parylene C with a reported a life time of 6 months at 37 °C. Li et al, performed both passive and active ALT on Parylene C(4.7 and 9 µm) thin films at 77 and 90 °C in saline (Li et al. 2010). In passive ALT tests the Parylene C samples (n=5) were only soak tested while active tests involved a continuous application of 5V at 60 Hz between the sample and a reference electrode. Failures were evaluated by optical microscope (passive samples) and measuring the changes in DC resistance (active samples) of the soaked samples. The reported MTTF for the 4.7 µm was very low compared to the 9 µm thick Parylene C in both active and passive tests. The authors suggested that a thickness of approximately 10 µm would provide with better barrier properties and the extrapolated survival time of 60 years at 37 °C (body temperature). However, thinner Parylene C layers are preferred due to small dimension requirements of neural interfaces. Other methods such as atomic layer deposition (ALD) of alumina underneath a thin layer of Parylene-C have been proposed to increase Parylene C efficacy to work over a long time period (Xi et al, 2012). In this study interdigitated electrodes (IDEs) coated with a bilayer of Al_2O_3-Parylene C (3 nm/6 µm) were age accelerated (37 57, 67and 80 °C) and EIS with DC leakage currents were

used to evaluate the performance of the electrodes. At 80 °C the bilayer coated samples lasted 3 times longer than only Parylene C coated samples. The MTTF was not reported as no failures were observed to determine the lifetime.

CHAPTER 3: ELECTROCHEMICAL IMPEDANCE SPECTROSCOPY

3.1 Overview

Electrochemical impedance spectroscopy (EIS) is a powerful tool to investigate the electrochemical properties of materials as varied as conductors, semi-conductors, insulators (Fernández-Sánchez, McNeil, and Rawson 2005) and even biological tissue (Macdonald 1992)(Azzarello, Masi, and Mancuso 2012)(Randviir and Banks 2013). The technique involves measuring the current response to small sinusoidal AC voltage (5-50 mV) perturbation by varying its frequency (Barsoukov and Macdonald 2005). The response is measured for at least every five points per decade change in frequency. The ratio of the applied voltage and current response is impedance, a measure of the barrier towards an applied electric field through a system. This ratio of voltage and current at different frequencies gives us a spectrum of impedance of the system. Impedance spectra (0.1 mHz –10 kHz) gives a single snapshot of various prominent kinetic processes in different frequency ranges, such as low frequency mass control/diffusion, charge transfer resistance in mid and dipolar properties in high frequencies (Barsukov and Macdonald 2002). It is restrictive in the sense that it best describes the system properties as long as the electrical perturbation is in the linear range (Barsukov and Macdonald 2002). However, its power lies in the fact that various complex processes describing a specific

system can be broken down into discrete and distributed electrical components by fitting the impedance spectrum (Barsukov and Macdonald 2002).

In this study, EIS was used to characterize the electrochemical properties of conductive electrodes as the interacting media changes from an electrolyte to a tissue. Additionally, EIS was used as a tool to understand how insulation degrades under accelerated age conditions of heated electrolyte (Bierwagen et al. 2003). The basics, measurement technique and equivalent circuit modeling relevant to this study will be discussed in this chapter.

3.2 Basics

The Ohm's law states that the voltage (V) varies linearly with current (I), where the proportionality constant is known as resistance (R). However, real systems not only dissipate energy (R) but also exhibit energy storage (Macdonald 1991). These are described as capacitors (C), where the voltage and currents are time dependent and are related as follows: $I = C\frac{dV}{dt}$

Thus, a small signal AC voltage applied across real systems would generate an AC current as an output response. Depending on the physical, structural and chemical properties of the material the AC current response may lead, lag with respect to the applied potential (figure 3.1)**.** The lead and lag between the input and output signals is defined by a phase angle (θ). The value of θ defines the properties of the materials with θ = 0° pure resistor, -90° pure capacitor. Thus, complex numbers were used to distinguish the in phase resistance the out of phase capacitive properties of the material.

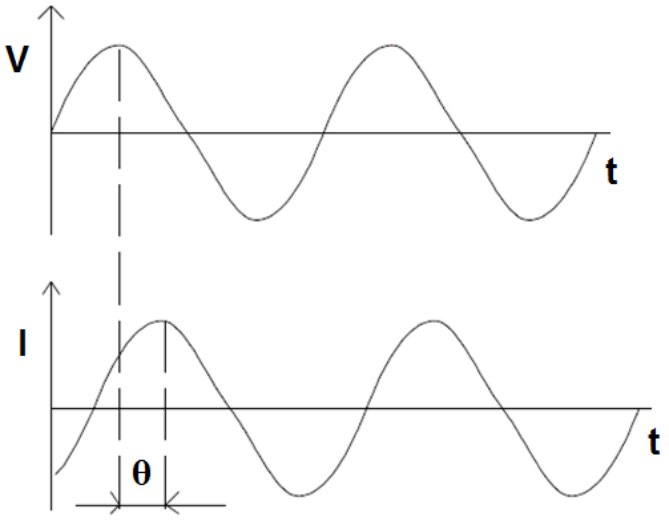

Figure 3.1: Current (I) response to an applied sinusoidal voltage (V) signal plotted with respect to time. The phase difference between the input and output is represented by θ.

Impedance is represented as $Z = Re(Z) + J\,Im(Z), (J = \sqrt{-1})$ and the real part of impedance (Re(Z)) represents the resistance and imaginary impedance (Im(Z)) is known as the reactance. The reactance of capacitance is expressed as $1/j\omega C$; $\omega = 2\pi f$, f is frequency in hertz, C is the capacitance in farads.

Another useful format of expressing impedance is in its polar form: $Z = |Z|e^{-j\theta}, |Z| = \sqrt{(Re(Z))^2 + (Im(Z))^2}, and\ \theta = \tan^{-1}\frac{Re(Z)}{Im(Z)}$, where |Z| is known as the impedance modulus and θ is the impedance phase.

3.3 Measurement

The basic device used to measure EIS is a potentiostat. A potentiostat is control instrumentation and measures the impedance spectrum by controlling a sinusoidal voltage and measuring the resulting current response in an electrochemical cell (Barsoukov and Macdonald 2005). To isolate the processes at the working electrode a three-electrode setup is employed involving a working, reference and a counter electrode (figure 3.2). Working electrode (WE) is the site where the investigated electrochemical phenomena takes place by controlling its potential. The reference electrode (RE) is used to measure the potential of the working electrode. The counter electrode (CE) serves as a source or sinks for electrons so that current can be passed from the external circuit through the cell thus completing the cell circuit (Barsukov and Macdonald 2002).

The three electrodes are immersed in an electrolyte that is a medium through which charge transfer can take place by the movement of ions (figure 3.2). The collection of the electrodes, the electrolyte, and the container holding the solution is known as the electrochemical cell (figure 3.2). To isolate the impedance at the working electrode it is essential that the impedance of reference and counter electrode is negligible (Orazem and Tribollet 2008).

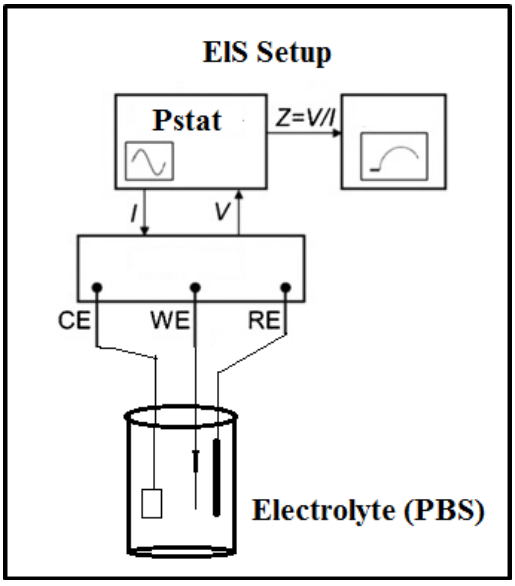

Figure 3.2: Schematic of an electrochemical setup and connections used for measuring electrochemical impedance spectroscopy. The potentiostat (Pstat) terminals working electrode (WE), counter electrode (CE), and reference electrode (RE) are connected to respective electrode immersed in an electrolyte solution. The potentiostat is controlled via a computer to set the parameters of the experiment and observe the impedance spectra.

The potentiostat maintains the potential between the working electrode and the reference electrode equal to a signal generator potential. This potential may be a constant voltage supply or a time varying signal. This control of the cell potential between the working and reference electrode is done by forcing it to be same as the signal generator through a negative feedback circuit containing the counter electrode in such a way to reduce the difference to zero (Orazem and Tribollet 2008). The measured variable is the cell current between the working and the auxiliary electrode. This whole process must be performed in such a way so that a considerable amount of current is not drawn through the reference electrode (Orazem and Tribollet 2008).

3.4 Data representation and analysis

Two most widely used graphical representations are Nyquist and Bode format which help in identifying the different electrochemical processes (Orazem and Tribollet 2008). Nyquist representation uses the Cartesian format of impedance and plots imaginary (Im(Z)) versus the real impedance (Re(Z)) (figure 3.3). Bode representation uses the polar format of impedance and plots of impedance modulus (|Z|) and phase (θ) against a logarithmic scale of frequency (figure 3.4). In a Nyquist plot the frequency information is embedded (higher frequency information on left) and the shape of the plot identifies the electrochemical process elements (Orazem and Tribollet 2008). For example, a resistor appears as a shift on the X-axis while a vertical line represents a capacitor(Orazem and Tribollet 2008). A simple combination of a resistor in parallel with a capacitor appears as a semicircle (figure 3.3). A straight line with a slope of 1 is related to mass transport processes (Warburg diffusion) (Orazem and Tribollet 2008).

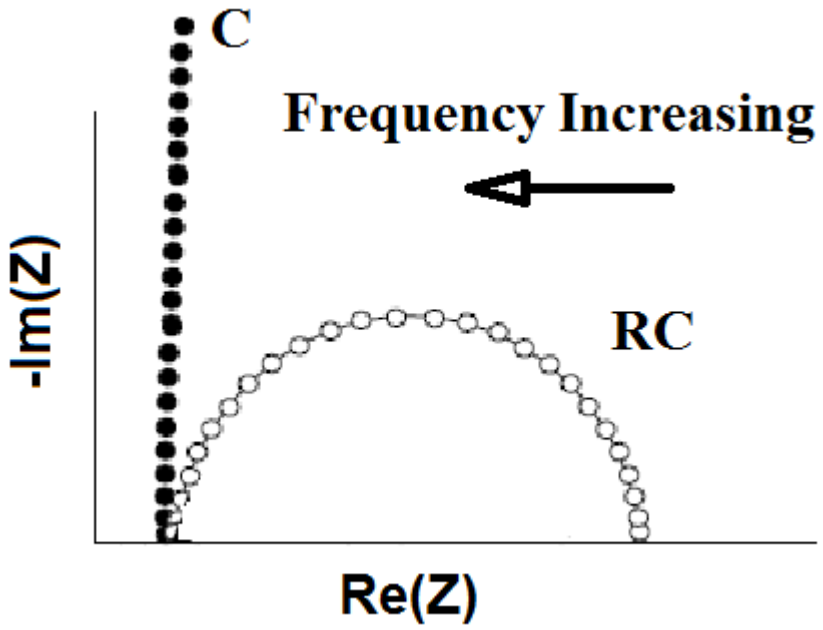

Figure 3.3: Nyquist Plot of pure capacitor (black dots) and a resistor in parallel to a capacitor (white dots). A pure resistor would appear as a shift (resistance value) on the Z' axis (impedance real). The frequency information is embedded in the plot with right to left as the increasing direction of frequency.(fig modified from (Fernández-Sánchez, McNeil, and Rawson 2005))

The variation of impedance with frequency is explicit in the Bode format (Orazem and Tribollet 2008). The slope of |Z| is used to identify different process parameters as resistance (0) , capacitance (1) and diffusion (-1/2) (figure 3.4) (Fernández-Sánchez, McNeil, and Rawson 2005).

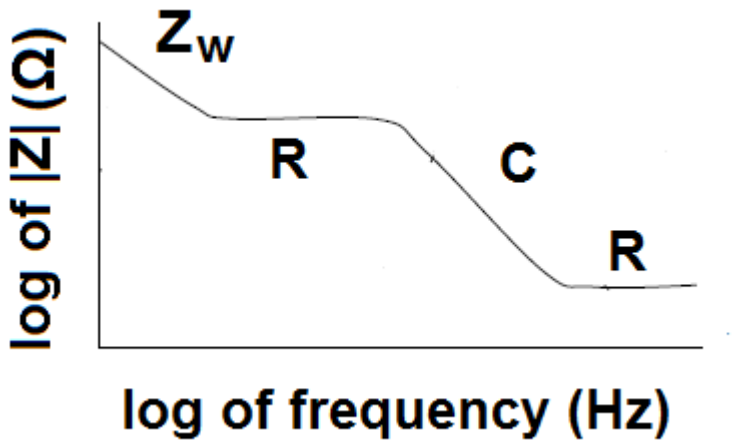

Figure 3.4: Bode Plot of impedance modulus (|Z|), describes impedance behavior of a simple electrochemical cell involving a single Faradaic process. The type of circuit element can be identified by the slope of the |Z| curve. The horizontal lines are representative of resistive behavior while a slope of -1/2 and 1 represents Warburg diffusion and capacitance respectively. (fig modified from (Fernández-Sánchez, McNeil, and Rawson 2005))

3.5 Equivalent Circuit Modeling

Using the information from the graphical representation, the measured impedance can be fit to an equivalent circuit consisting of discrete and distributed electrical components representing the different electrochemical processes (Barsoukov and Macdonald 2005; Orazem and Tribollet 2008).

3.5.1 Discrete elements

The charge transfer processes and conductive paths in the bulk of system are represented by resistors (Barsukov and Macdonald 2002). The space-charge-polarization due to dielectric bulk properties and charge redistribution at the interface are represented

by capacitors (Barsukov and Macdonald 2002). While, the concentration variations due adsorption and diffusion processes are approximated by different combinations of capacitors and resistors. The impedance using discrete elements can be solved by using linear algebra(Barsukov and Macdonald 2002).

3.5.2 Distributed elements

Certain electrochemical properties such as diffusion or distribution of activation energies in the bulk cannot be described by finite combination of discrete elements (R,C). Instead, these process are better described via combinations of discrete elements, repeated infinitely creating a chain line network known as the "transmission line" (Barsukov and Macdonald 2002). These infinitely long networks are called "distributed" circuit elements and solving these requires higher forms of calculus (Barsukov and Macdonald 2002).

Many distributed elements have been proposed to describe the bulk material properties (Cole-Cole, Cole-Davidson, Havriliak Negami) (Barsukov and Macdonald 2002), and diffusion (Warburg, PNPA) (Barsukov and Macdonald 2002) etc. In this study two distributed elements were used to fit both conductive and insulated electrodes, Constant Phase Element (CPE) and Warburg (W) impedance. CPE is a frequency dependent capacitor and is usually associated with the distribution of time constants due to inhomogeneous surfaces (Orazem and Tribollet 2008). CPE is mathematically expressed as $Q_o/(j\omega)^{\alpha}$,Q_o is a constant, $j = (-1)^{1/2}$, $\omega = 2\pi f$, and α is a constant between 0 and 1. If $\alpha=1$, Q_o is the capacitance in farads (Orazem and Tribollet 2008). The Warburg (W) diffusion element is a CPE with $\alpha=5$, representing diffusion at low frequencies

(Orazem and Tribollet 2008). This representation of Warburg assumes that ions in the bulk diffuse towards the electrode surface placed at infinite distance (Orazem and Tribollet 2008). However, an electrochemical cell is always finite in dimensions and various modifications and corrections of the Warburg impedance have been reported and complex theoretical models are currently being developed (Macdonald 2011).

3.5.3 Data fitting

Once the equivalent circuit model is developed according to the measured spectrum, appropriate impedance function can be generated. Parameter optimization can be achieved using non-linear least square fit algorithms such as Levenberg-Marquardt (Barsukov and Macdonald 2002) and Down-Hill Simplex methods (Orazem and Tribollet 2008). Various standalone programs have been developed to fit impedance spectra such as LEVM (Macdonald and Potter, 1987), and ZsimpWin (Bruno Yeum, 2001). Assuming the model explains the electrochemical processes the impedance function is fit to the measured impedance spectra. The general accuracy of the fit can be evaluated using these three basic criteria (Orazem and Tribollet 2008): (a) visual fit to Bode, Nyquist, real, and imaginary impedance values versus frequency plots, (b) low chi-squared value ($\chi 2$), and (c) low relative standard errors for every circuit element. As suggested by Cui and Martin, a $\chi 2$ of on the order of 0.001 or below is acceptable (Cui and Martin 2003). Relative standard errors for each variable are considered acceptable if lower than 15%. An ideal equivalent circuit should be able to fit all three graphical representations accurately with a low $\chi 2$, low relative standard error and present a random residual plot (Orazem and Tribollet 2008). Residuals are the difference between the actual data and

estimated data values of the fit. For an *ideal fit* where the circuit elements describe the processes accurately, the plot of residuals will be randomly distributed (Orazem and Tribollet 2008). Figure 3.5 (a) shows clear trending in residual plots, while an improvement in residuals in figure 3.5 (b) is implied as they are clearly scattered though not perfectly random.

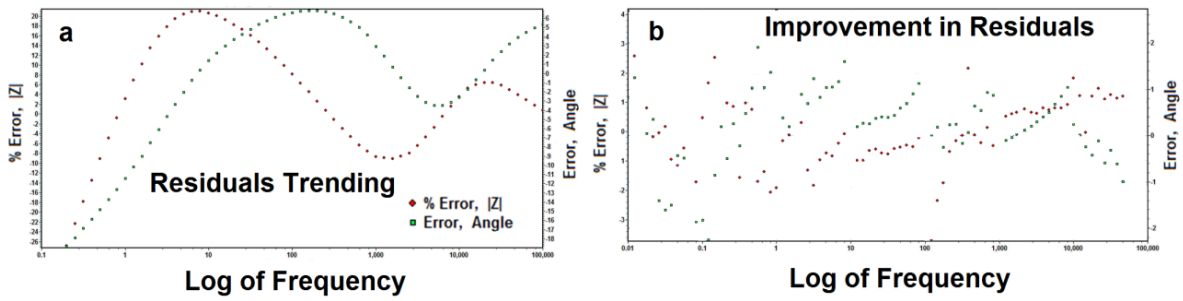

Figure 3.5: Plot of residuals for a fit to an impedance spectra. (a) Trending in residuals and (b) a scattered residual plot suggesting an improvement in the model.

Trending in the residual plots could be due improper circuit model, incomplete or non-accurate representation as well as to biases as due systematic errors (Orazem and Tribollet 2008). The model fits conducted in this study did not generate perfectly random residuals. The main reason being that the distributed elements used were not a true representation of the system under study. The Warburg impedance used for the fits is a poor approximation of the diffusion processes (Macdonald 2010). Diffusion models such as Poisson Nernst Anomalous Plank (PNPA), developed by Dr. Macdonald, though a

better approximation couldn't be applied due to geometrical and material restrictions (Macdonald 2010). PNPA diffusion model doesn't assume electro-neutrality for the diffusing ions unlike Warburg diffusion (Macdonald 2010). However, it requires the counter and working electrodes have a plane parallel geometrical setup. Also, PNPA is applicable towards blocking electrodes (no Faradaic charge transfer) or quasi-Faradaic charge transfer (Macdonald 2010). Various distributed elements (Havriliak Negami, Davidson Cole, etc) are better options in terms of fitting the bulk properties over discrete element. However, there are issues in assigning physical relevance to these parameter values. Thus, discrete elements and distributed elements that are approximations of the process with physical significance were chosen for the models.

3.5.4 Modeling Conductive coating

The common electrical model describing the conductive electrode-electrolyte interface is the Randles circuit (figure 3.6). When an electrode is placed in an electrolytic media, charge redistribution occurs at its surface represented as a double layer capacitor (C_{dl}) (Bard and Faulkner 2006; Barsoukov and Macdonald 2005; Orazem and Tribollet 2008). Electrochemical reactions start to occur at this interface if a charge/potential is applied at the electrode surface. The simplest electrochemical reaction can be described as n number of electrons (ne^-) transferring from an oxidant (O) to form a product (R) is as follows $O + ne^- \rightarrow R$.

This type of charge transfer involving electron transfer across the interface is known as Faradaic process (Bard and Faulkner 2006). The energy barrier for the electron transfer to cross the interface and through the solution at an applied potential is described

as polarization (R_P) and solution (R_S) resistance (Chang and Park 2010). However, if a standard electrode potential is applied to the electrode, R_P is instead designated as charge-transfer potential (R_{ct}) (Chang and Park 2010). The rate of electron transfer is dependent on mass transport of the reactants and products diffusing at the interface and is defined by Warburg distributed element Z_w (Orazem and Tribollet 2008). While the charging of the interfacial double layer described as a C_{dl} contributes to the non-Faradaic charge transfer (Orazem and Tribollet 2008). Randles circuit composition with the elements described above is shown in Figure 3.6.

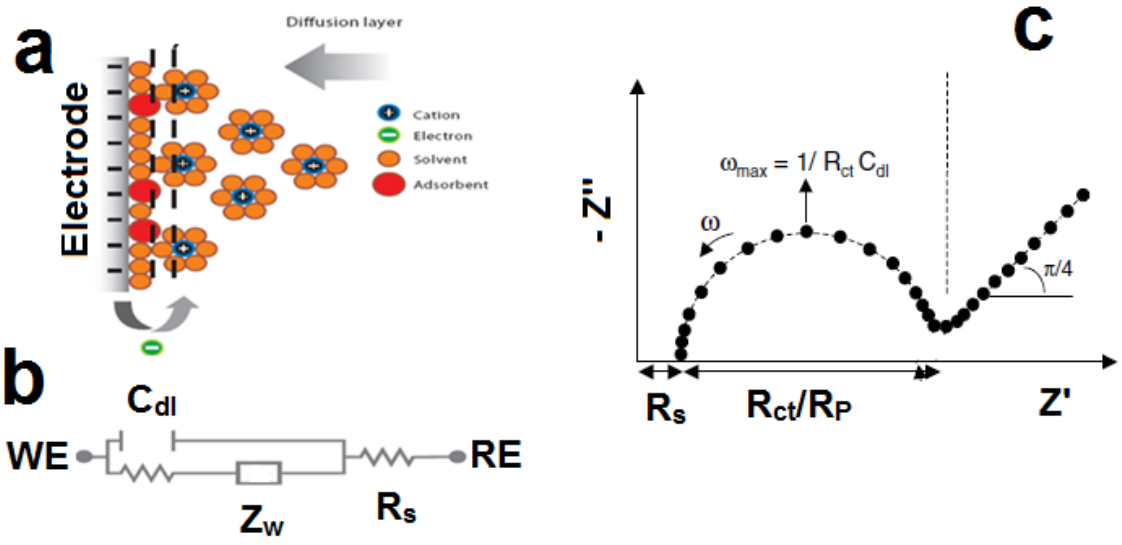

Figure 3.6: (a) A negatively charged electrode attracts positive ions present in the electrolyte. The charge accumulation at the electrode surface is modeled as a double layer capacitor (Cdl). Faradaic process of electron transfer is modeled as Rct and diffusion as Warburg impedance Z_W. (b) An idealized Randles electrical equivalent circuit for the interface measured between a working electrode (WE) and reference electrode (RE) (c) Nyquist representation of the impedance spectra where the parameters are identified. ((fig modified from (Chang and Park 2010))

Nyquist representation (figure 3.6 (c)) can be used to make good initial estimate for the parameter values described in the Randles circuit (Barsoukov and Macdonald 2005). Solution resistance (R_s) is estimated as the difference between the value of Z' at left most edge of the spectrum and center of axis (Fernández-Sánchez, McNeil, and Rawson 2005). While the width of semicircle gives an estimate of R_{ct}/R_P (Fernández-Sánchez, McNeil, and Rawson 2005). C_{dl} is estimated by finding the mid frequency (f) of the semicircle and using the expression $C_{dl} = \frac{1}{2\pi f R_{ct}}$. The Warburg coefficient is estimated by extrapolating the 45° diffusion line towards Z' axis (Fernández-Sánchez, McNeil, and Rawson 2005).

3.5.5 Modeling Insulation

An insulated coating on an electrode immersed in an electrolyte is modeled as electrolyte solution resistance (Rs) in series with capacitance (C_L) (Fernández-Sánchez, McNeil, and Rawson 2005). C_L is the capacitance of the insulated coating on the electrode. R_L accounts for any defects in the bulk of the coating creating conductive pathways in an insulating material. Figure 3.7 shows an example of the equivalent circuit model and Nyquist representation of the EIS spectra for an intact coating.

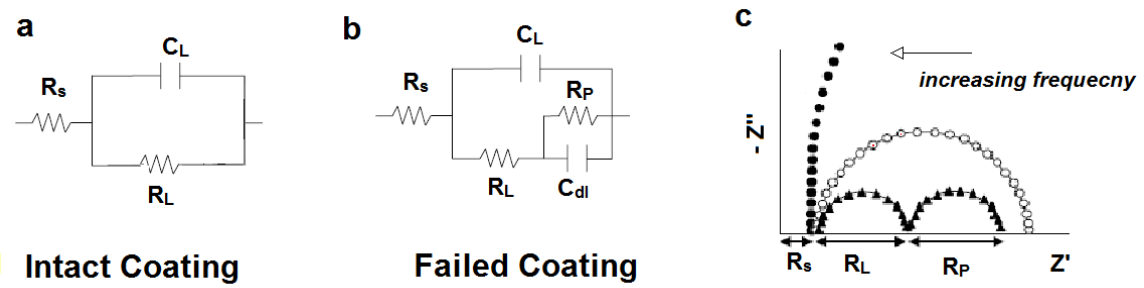

Figure 3.7: (a) Equivalent circuit of an intact, (b) failed insulation immersed in an electrolyte. R_s the solution resistance, C_L layer capacitance, R_L layer resistance, R_P polarization resistance and C_{dl} double layer capacitance of the exposed metal. (c) Nyquist spectrum of an intact insulation (black circles) , electrolyte penetration (white circles) and electrolyte accessing the underlying metal (black triangles). (fig modified from (Fernández-Sánchez, McNeil, and Rawson 2005))

The coating resistance (R_L) gradually decreases with electrolyte penetration and appears as bending of the Nyquist curve to form a semicircle (figure 3.7(a)) (Fernández-Sánchez, McNeil, and Rawson 2005). While, C_L increases with electrolyte permeation, as the aqueous electrolyte has a higher dielectric constant ε_r=80 (Uematsu and Frank) compared to an insulation, for example Parylene C (ε_r =3) (Xie et al. 2012).

Thus, the same model used for intact coating can be used to model the EIS spectra as presented in figure 3.7(a). The impedance characteristics changes as the insulation degrades further allowing the electrolyte to penetrate enough to access the underlying metal (Fernández-Sánchez, McNeil, and Rawson 2005). A second semi-circle emerges in the Nyquist curve (figure 3.7(c)) associated with the polarization resistance (R_P) and double layer capacitance (C_{dl}) of the exposed metal figure 3.7(b) (Fernández-Sánchez, McNeil, and Rawson 2005). The semi-circle at high frequency in figure 3.7(c) is due to

coating capacitance (C_L and R_L) (Fernández-Sánchez, McNeil, and Rawson 2005). R_P reflects the rate of corrosion of the underlying metal substrate and C_{dl} is the double layer capacitance between the exposed metal and the electrolyte (Fernández-Sánchez, McNeil, and Rawson 2005).

CHAPTER 4: METHODOLOGIES

4.1 Overview

This chapter describes the various methods used for evaluating conducting (carbon nanotubes, iridium oxide) coatings on microwires and insulation (Parylene C and Al_2O_3-Parylene C) on interdigitated structures. Evaluations were primarily investigated by electrochemically characterization, essentially electrochemical impedance spectroscopy and cyclic voltammetry. Microwires coated with iridium oxide and carbon nanotubes were further electrochemically characterized *in vivo* for acute scenario using rodent model. The early signs of inflammation due to the presence of carbon nanotube electrodes were also investigated. For insulation the samples were thermally age accelerated and the stability of the barrier properties were evaluated primarily via electrochemical impedance spectroscopy and DC leakage currents.

4.2 Electrode Fabrication

Two kind of electrode structures were used in this study, microwires of 250 µm diameter (figure 4.1) for all conductive coatings and IDE structures (2.7 x 0.6 cm) with electrode width and pitch of 130 um (figure 4.2). The electrode fabrications of each kind with different coatings are described in the subsections.

4.2.1 Microwires

Substrates were made from 250 µm diameter medical grade (316L) stainless steel wire encapsulated with polyimide insulation. 3 mm of the polyimide was removed from the tip, leaving an exposed geometrical area of 2.5mm^2 for deposition. Every electrode is chemically cleaned and electrochemically cycled prior to deposition. The cleaning procedure includes bath-sonication of electrodes in three electrolyte solutions for 20 minutes each. The solutions are potassium hydroxide, distilled water, and ethanol, respectively. This step is followed by dipping the stripped electrode tips in aqua-regia (concentrated (HNO_3:HCl), 1:3) at room temperature for 2 minutes. This step slightly etches the surface of the stainless steel and removes surface contaminants. Electrodes are also cleaned through an electrochemical cycling process. The voltage is swept from -0.7 V to 0.7 V at 50 mV/s for 25 cycles against a silver/silver chloride (Ag|AgCl) reference electrode and platinum foil (counter electrode), in phosphate buffered saline (PBS). Current is simultaneously measured via a commercial potentiostat (REF 600, Gamry Instruments, Warminster, PA). This step is called electrochemical cycling and the measured current peaks with the shape of the voltage versus current curve provides a visual confirmation as to whether the electrode shows stainless steel, carbon nanotube, iridium oxide like behavior.

4.2.2 Multi-walled carbon nanotubes (MWCNTs)

An electrophoretic cell was made using an 8 ml glass vial containing the MWCNT suspension as described in Minnikanti et al (2009). A two-pin socket is placed

over the opening of the vial and the electrodes are inserted in two adjacent sockets. The reference electrode and the deposition (working) electrode are placed parallel to each other in an electrophoretic cell. The inter electrode distance is less than or equal to 1mm. The 3 mm uninsulated tip of the deposition electrode is completely dipped in the suspension. The reference electrode used is either gold or silver. Once the electrodes are immersed in the suspension, a voltage of 2.3 V is applied between the two electrodes (inter electrode distance ~1 mm) for about 10 to 20 minutes. Later the voltage is switched off to stop the electrophoretic deposition and the electrode (figure 4.1) is removed from the electrophoretic cell. Every electrode is characterized electrochemically by cyclic voltammetric and electrochemical impedance spectroscopy before and after deposition as described in section 4.3.

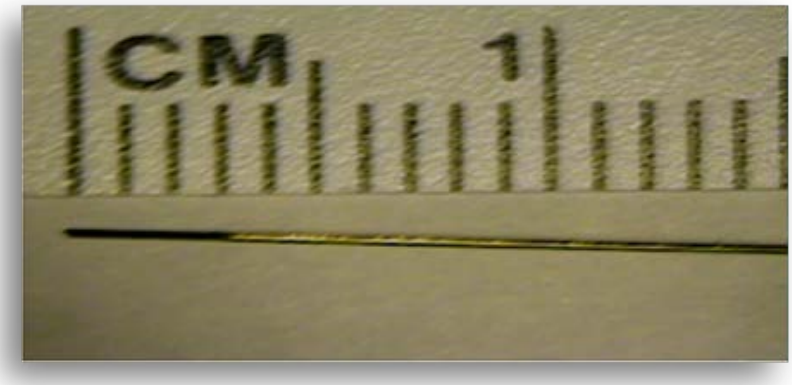

Figure 4.1 MWCNT electrocphoretically deposited on a stainless steel (250 μm diameter) microwire.

4.2.3 Electrodeposited iridium oxide films (EIROF)

The electrochemical deposition of EIROF used here is a modification of the Meyer et al (2001) technique, optimized for *in vivo* long term charge delivery performance. The deposition solution is prepared with iridium tetrachloride (0.4 mM) and oxalic acid (40 mM), and adjusted to a pH of 10.3 with the addition of high molarity potassium carbonate (500 mM). Iridium oxide is electrochemically deposited onto stainless steel substrates by sweeping an applied voltage between the steel substrate and a Ag|AgCl pellet from 0 to 0.55 V and back at 50 mV/s for 50 cycles, followed by 1600 cycles of a 1 Hz square wave, between 0 and 0.55 V. The sequence formed by the triangular and square waves constitutes one deposition cycle, and it takes approximately 45 minutes to complete. Electrodes are deposited for typically 32 cycles (approximately 24 hours). The number of cycles is varied and the electrical performance of the deposited film evaluated. For a subset of microwires EIROFs were deposited while placed in an ultra-sonicating bath. Every electrode is characterized electrochemically by cyclic voltammetric and electrochemical impedance spectroscopy before and after deposition as described in section 4.3.

4.2.4 Interdigitated Electrode Arrays (IDEs)

Parylene C and Al_2O_3-parylene C coated IDEs were provided and fabricated at University of Utah using standard lift-off lithographic process. The IDEs structures were fabricated on a 500-µm thick fused silica substrate with electrode width and pitch of 130 µm (figure 4.2). The electrodes are stacked layers of Ti(100 nm)/Pt(150 nm)/Au(150 nm) and annealed for 45 min at 375 °C in forming gas (98% of Ar and 2% of H_2). 30 AWG wire (10 cm) with high-temperature insulation were soldered (lead free) to two bond pads on IDEs for electrical contact. The solder joints and contact pads were coated with silicone (MED-4211). After cleaning IDEs with ultrasonication for 5 minutes each with acetone-isopropyl alcohol-deionized water, they were placed in a fixture that allowed for complete coating of the sample. This was followed by parylene C only and Al_2O_3-parylene C coating of the IDE substrate. 6 µm of parylene C on top of Silane A-174 (Momentive Performance Materials) was deposited using the standard Gorham process (Gorham 1966) using LabTop 3000 parylene. Thin Al_2O_3 (5 nm) was deposited using plasma assisted atomic layer deposition (PAALD) using sequential trimethylaluminum (TMA) vapor and oxygen plasma for 500 cycles at 120 °C using Fiji F200 (Cambridge , NanoTech Inc.). The pressure for each cycle was set at 0.3 mTorr and the pulse sequence was 0.06 s TMA, 10 s argon purge, 20 s oxygen plasma, and 5 s argon purge. Following the PAALD layer, 6 µm of parylene C with Silane A-174 (2 hours in vacuum) was deposited at room temperature as described above. The coated IDEs are mounted into caps of 6 ml vials and sealed with silicone med-4211 (figure 4.2). This ensures positional stability of IDEs in the vial and also lowers the evaporation rate of PBS over time.

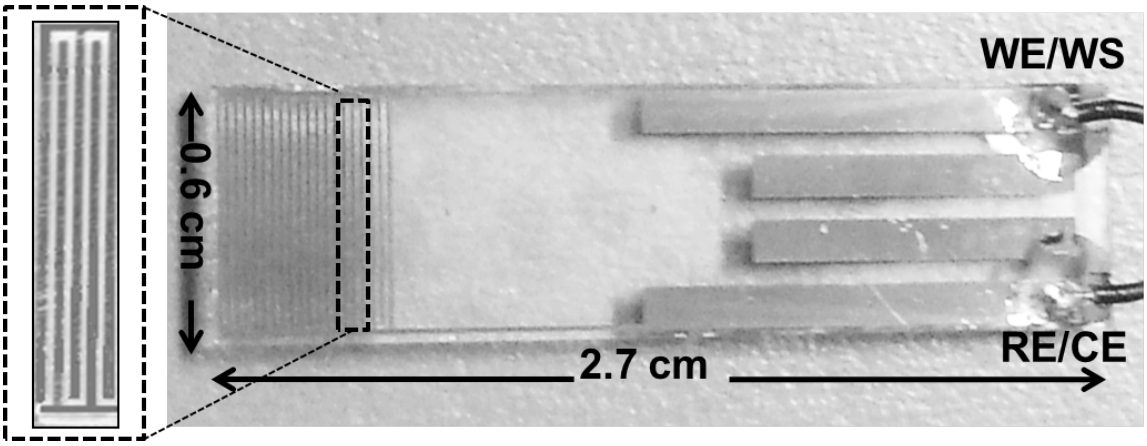

Figure 4.2 The interdigitated electrodes structure consists of gold microelectrodes coated with either Al_2O_3 -Parylene C (5 nm/6 µm) or Parylene C (6 µm). The width and pitch of the interdigitated electrodes is 130 µm. Wires connected to the solder bond pads provide with electrical connections to the IDE structure. Electrochemical characterization is performed using a two electrode setup where the working electrode/working sense (WE/WS) and reference electrode/counter electrode (RE/CE) terminals of the potentiostat are connected to the two fingers of the IDE.

4.3 Electrode Electrochemical Characterization

The electrochemical setup and electrochemical characterizations employed for *in vitro*, *in vivo* investigations of microwires and thermal age acceleration of IDEs are discussed below.

4.3.1 Electrochemical cell setup

All *in vitro* analyses for microwires were realized in 1 X PBS poured into 25 ml beakers at room temperature 25 °C, kept at a pH of 7.4 using a three-electrode setup with Ag|AgCl as the reference electrode and platinum foil as the counter electrode. For *in vivo* analysis a three electrochemical setup consisted of a coated microwire stereotaxically implanted in the left hippocampus (described in section 4.5) with the Ag|AgCl pellet (reference electrode) and platinum foil (counter electrode) positioned against the exposed skull, and bathed in 0.9% NaCl. The *in vitro* and *in vivo* electrochemical setup were connected to REF600 (Gamry Instruments, Warminster, PA) potentiostat.

While a two electrode setup was employed for characterizing all IDEs at room temperature and 60 °C in 1 X PBS (pH 7.4). The IDEs are mounted into a 6 ml vial containing PBS. The counter; reference terminals of the potentiostat were shorted and connected to one of the IDE fingers (figure 4.2), while, the working and working sense were connected to the second IDE finger. CHI660D (CH instruments Inc., Austin, TX) potentiostat was used for all electrochemical testing at room temperature and 60 °C.

4.3.2 Cyclic Voltammetry

The CV cycles at a rate of 50 mV/s within the voltage limits of -0.7 V to 0.7 V against a reference electrode potential were employed for microwires and IDE structures. The cathodic charge storage capacity (CSCc) is obtained by integrating the cathodic current over time for one period of the triangular waveform. The CSCc can be visualized as the lower half of the area delimited by one CV cycle. We assume here a surface area of 2.5mm^2 for all coated microwires, despite the fact that the MWCNT coating and EIROFs

increases the active area of the electrode. All CSCc values are reported in $\mu C/cm^2$ for consistency.

The CV section precedes the potentionstatic EIS for the deposited microwires and includes 25 pre-conditioning CVs followed by 5 CV cycles. *In vivo* analysis follows the same regime and is conducted both prior and subsequently to implanting the electrode. For a subset of EIROF films the 25 pre-conditioning CVs followed by 5 CV cycles was not conducted *in vivo* and *in vitro* in PBS prior to implantation. For IDEs the CV section includes 5 CV cycles measured every 6 hours throughout the experimental time course.

4.3.3 Electrochemical Impedance Spectroscopy

The *In vitro* and *in vivo* EIS frequency range for coated microwires ranged from 0.01 Hz to 100 kHz, with an AC sinusoidal signal of 10 mV_{rms} and 0 V DC bias. The measured frequencies were 10 points per decade on a logarithmic scale. For each *in vivo* experiment, there are two associated *in vitro* (PBS) measures: before implantation (pre) and after explanation (post). Before performing the impedance scan the open-circuit potential (OCP) was recorded in each case as it reflects the chemical characteristics of the interface (Franks et al. 2005).

For IDEs the EIS frequency range chosen was from 0.01 Hz to10 kHz with an AC sinusoidal signal of 50 mV_{rms} and 0 V DC bias. The measured frequencies were 12 points per decade on a logarithmic scale.

The impedance data from coated microwires (*in vitro*, *in vivo*) and IDEs (room temperature: 25 °C, age accelerated: 60 °C) were fit to appropriate equivalent circuit

models. The software used to fit the impedance data was commercially available ZSimpWin (Ann Arbor, MI). ZSimpWin employs the down-hill simplex method a non-gradient optimization technique. Function evaluations and comparisons are repeated until a local minimum is reached using a trial-and-error method. This local minimum is equal to the global minima. This software also provides with good initial estimates highly essential in regression based fits. Initial estimates were also gathered from the pictorial representations and compared to software derived. Data was imported in raw format from Echem Analyst™ (Gamry Instruments, Warminster, PA), for microwires data. While the IDE impedance data from CH instruments had to be converted to a text file with the format of Frequency, Impedance real and negative impedance imaginary columns using a customized MATLAB ® code (Dr.Nathalia Peixoto).

All the models used in this study meet all the following four criteria (Orazem and Tribollet 2008): (a) explains the biophysics at the interface/ physical interpretation, (b) visual fit to Bode, Nyquist, real, and imaginary impedance values versus frequency plots, (c) low chi-squared value ($\chi 2$), (d) and relative standard errors for every circuit element below 20 %. As suggested by Cui and Martin, a $\chi 2$ of on the order of 0.001 or below is acceptable (Cui, Martin, 2003).

4.3.4 DC leakage currents

The DC leakage currents were measured for IDE structures from each coating Parylene C and Al_2O_3 Parylene C using Chronoamperometry. Here a potential pulse is applied between the working and the reference electrode while the response current is measured with respect to time. All DC leakage currents were measured by applying a 5 V DC pulse for 600 seconds.

4.4 Surface Characterization

The surface morphology of EPD MWCNT coatings on microwires was evaluated by a scanning electron microscope (SEM) operated at 5.00 kV. The resolution varied from 100 nm to 200 μm.

Elemental analysis for the industrial and research grade suspensions used for EPD was achieved by inductively coupled plasma atomic emission spectrometer (ICP-AES) (Perkin–Elmer Optima 3000DV). MWCNTs were dispersed in HNO_3 (1%) solution. The ICP-AES characterizations were calibrated with standard samples.

X-ray photoelectron spectroscopy (XPS) was performed using a custom-instrument predominantly composed of equipment from Perkin–Elmer (physical electronics division). The X-ray source has a spot size of a few millimeters and is operated at 15 kV, 17 mA (250 W) using a dual Mg/Al anode. Non-monochromatized Al (Ka 945; hv = 1486.6 eV) source was used for these experiments. Survey spectra were collected by scanning from 1000 to 0 eV on the binding energy scale at pass energy of 100 eV; a total of 10 scans were averaged. The operating pressure of the spectrometer was typically 109 mbar and signal processing was performed using AugerScan™ (RBD Instruments, Bend, OR).

4.5 Surgery Procedures

Male Sprague–Dawley rats were kept in a controlled environment with a constant 12:12 h light–dark cycle and were provided food and water ad libitum. All procedures were performed in accordance with the National Institutes of Health Guide for the Care and Use of Laboratory Animals and were reviewed and approved by the George Mason University IACUC (protocol number: 0140-2007). Adult animals were used throughout this study, with approximate weight of 250 g; they were anaesthetized with isoflurane (2%) and kept under anesthesia during the implant procedure. Following the coordinates as shown in the 2007 edition of the Paxinos Rat Brain Atlas (Paxinos and Watson 2007), electrodes were stereotaxically implanted in the left hippocampus (5.2 mm behind bregma and 5 mm to the left of the line connecting bregma to lambda), and then slowly (1 mm/min) lowered 7 mm **(**figure 4.3**).**

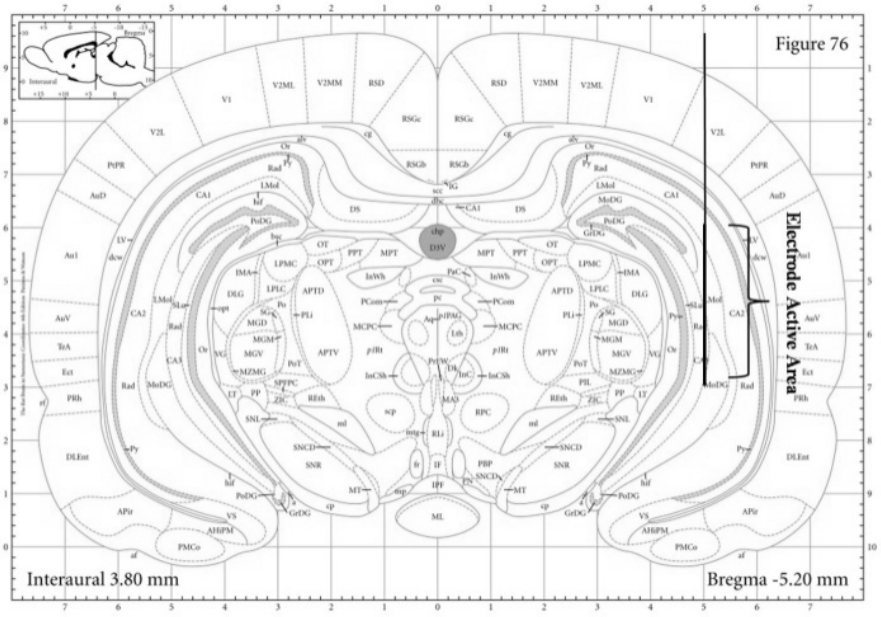

Figure 4.3: Test electrodes were stereotaxically implanted in the left hippocampus (bregma referred AP = − 5.20 mm and ML = − 5.00 mm), and then lowered to DV= − 7.00 mm as in the coronal section shown in this figure. The electrode is implanted such that the active area, with a 3 mm height, is located within the hippocampal region. (fig modified from Paxinos and Watson 2007)

Only one electrode was implanted per animal, and EIS and CV was performed during the surgery through a three electrode setup as described in section 4.2. The electrode was then explanted and cleaned with ethanol and deionized water

4.6 Low frequency stimulation protocol

For MWCNT microwires the electrochemical performance and early inflammatory reaction was investigated using a total of 18 animals. These were divided in three experimental groups: control animals, with no implants, implanted animals, with electrodes implanted, but no stimulation, and stimulated animals, with one electrode implanted and electrical stimulation applied during the surgery. The simulation model

followed was electrode-based, rather than animal-based, and therefore the choice of repeating the stimulation protocol in a buffered electrolyte solution and during the acute surgery is justified, if not required. The stimulation protocol consists of cyclic voltammetry and potentiostatic electrochemical impedance spectroscopy. The CV section included 25 pre-conditioning CVs followed by 5 CV cycles and preceded the potentionstatic EIS. After stimulating the rat hippocampus, electrodes were explanted, and cleaned with ethanol and deionized water. The electrodes were immediately re-characterized in order to evaluate whether they maintained their electrochemical characteristics.

For EIROF the *in vivo* electrochemical performance in comparison to a very similar *in vitro* paradigm was investigated using a total of 12 animals. These were divided into two experimental groups: un-stimulated animals, with no CVs applied *in vitro* and *in vivo* prior to EIS, and stimulated animals, with application of CVs prior to *in vitro* and *in vivo* EIS. After stimulating the rat hippocampus, electrodes were explanted, and cleaned with ethanol and deionized water. The electrodes were immediately re-characterized in order to evaluate whether they maintained their electrochemical characteristics.

4.7 Tissue collection and RNA extraction

Hippocampi were removed and individually frozen in dry ice. The frozen tissue was pulverized and homogenized in Trizol reagent (Invitrogen, Carlsbad, CA, USA); total RNA was isolated following manufacturer's instructions. RNA was treated with

DNase (Invitrogen, Carlsbad, CA) to remove any potential genomic DNA contamination. RNA concentration was measured spectrophotometrically at 260 nm.

4.8 Reverse Transcriptase - polymerase chain reaction (RT-PCR)

Total RNA (1 µg from each sample) was used in cDNA generation using oligo-dT (Invitrogen, Carlsbad, CA) and Reverse Transcriptase (Improm, Promega,San Luis Obispo, CA). The generated cDNAs were used for PCR amplification of fragments corresponding to TLR2, IL-1β, and ß-actin (internal control) using Platinum Taq polymerase (Invitrogen). Specific primers were designed based on the available sequences in GenBank and synthesized by IDT (Coralville, IA): TLR2: sense 5'- TCT CTG TCA TGT GAT GCT GCT GGT-3' and antisense 5'- TCC AAG TGT TCA AGA CTG CCC AGA -3'; IL-1β: sense 5'- TGT CAC TCA TTG TGG CTG TGG AGA -3' and antisense 5'- AAG ACA GGT CTG TGC TCT GCT TGA -3', and β-actin: sense 5'- CTA AGG CAA ACC GTG AAA AGA -3' and antisense 5'- ATT GCC GAT AGT GAT GAC CTG-3'. The expected amplification products for TLR2, IL-1 β and β-actin were 248, 555 and 421 bp, respectively. After separation in 2% agarose gels and staining with ethydium bromide (1mg/mL), the PCR products were densitometrically quantified using ImageJ (Abramoff, Magelhaes, and Ram 2004).

4.9 Accelerated lifetime testing

The process for ALT is presented in figure 4.4. Samples from each coating Parylene C and Al_2O_3 Parylene C were initially inspected in air and phosphate buffered saline (pH 7.4) at room temperature to rule out false positives due to fabrication, handling

or transportation damage. This was followed by samples being age accelerated in PBS at 60 °C, in a thermal bath. Go!Temp (Vernier, Beaverton, OR) a USB temperature sensor probe was enclosed in a PBS filled 6 ml vial placed in the thermal bath. The temperature was monitored via Logger Lite software (Vernier, Beaverton, OR) and variations were below ± 2 °C. Silicone oil was used in the bath to avoid evaporation. The samples were completely submerged in PBS throughout experiment. The glass transition temperature (T_g) for Parylene C as reported in the literature varies between 55 °C and 95 °C (Kahouli et al. 2009). ASTM F1980 (American Society for testing and materials-Standard guide for accelerated aging of sterile medical device packages) recommends that aging temperature not exceed 60 °C to avoid non-linear variations in the rate of reaction (Bierwagen et al. 2003), therefore we maintained a constant 60 °C during our experiments. As high impedance measurements are prone to noise, all measurements were conducted within a Faraday cage. Testing was interrupted to replace PBS in the vials every two weeks.

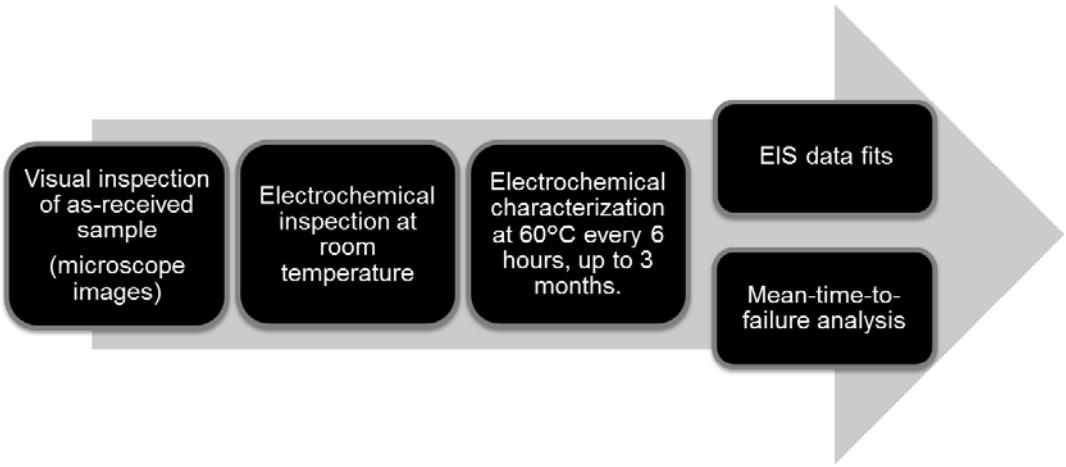

Figure 4.4: Process for accelerated lifetime testing of Al2O3 -Parylene C (5 nm/6 µm) and Parylene C samples (6 µm). The samples are initially inspected via electrochemical characterization (EIS and DC leakage currents) in air and immersed in PBS. All samples that pass the room temperature inspection are placed in the thermal bath for age acceleration. Electrochemical characterization (EIS, DC leakage currents and CVs) are measured every 6 hours throughout the course of the experiment. This is followed by mean time to failure estimation as well as equivalent circuit modeling of the measured EIS spectra.

The data files for each measurement were saved both as .bin and .txt files, with filenames specifying the IDE sample ID, potentiostat channel number and run number. Data was plotted and exported using customized MATLAB ® codes (coded by Dr. Nathalia Peixoto). The exported EIS files were further used for fitting the data with appropriate equivalent circuits.

4.10 Statistical Analysis

4.10.1 CSCc and Impedance

Statistical Analysis Data are presented as mean ± SEM (standard error of mean) over the arithmetically averaged experimental values of each of the three independent experiments. Significant effects ($p < 0.05$) were determined using the unpaired Student's t-test. Statistical analyses were performed for comparing CSCc and impedances of electrodes using the Wilcoxon Signed Rank test.

4.10.4 Biological response

For mRNA analysis parametric ANOVA and Newman-Keuls Multiple Comparison Test using the GraphPad software (Graph-Pad Prism, San Diego, CA) and SPSS (SPSS Inc., Chicago, IL) were used. Values shown in this study are expressed as mean ± SEM and, in all cases, statistical significance was accepted where $p<0.05$.

4.10.3 Mean Time to Failure

The criteria for failures was defined as when the DC leakage currents surpassed a threshold of 1 nA (Xie et al. 2012) with impedance modulus below 0.1 GΩ for frequencies above 1 Hz and impedance phase above -80° for any frequency greater than 1 Hz (Akbarinezhad and Faridi 2008). The time to failure for the insulating layers was estimated from the time stamp on the initial EIS files presenting with failed spectra. An exponential distribution was assumed for the failure times for Parylene C and Al_2O_3-Parylene C IDE sample groups at 60 °C. The mean time to failure (MTTF) for each sample was expressed as mean ± s.e.m.

This was followed by hypothesis testing to compare the MTTF between the two IDE groups. The null hypothesis was that MTTF of Parylene C (μ_1) is not different from Al_2O_3-Parylene C (μ_2) and was tested against one-sided alternative of $\mu_2 > \mu_1$. All samples that survived the 3 month accelerated aging without failing were included as right censored data. This accounts for the times of failure of the surviving IDEs as being "right" or greater than the 3 month ALT period. Next, the information from this study was used to determine sample sizes for future studies. Specifically, we determined sample sizes necessary to achieve a power of 80 % at the significance level of 0.05 to detect an effect size by using a log-rank test. The effect size used in the hypothesis testing and sample size calculation is the ratio of μ_1/ μ_2. The analysis was conducted by Dr. Guoqing Diao (Deptt. of Statistics, GMU)

The following formula and assumptions were used extrapolate the MTTF to body temperature (37 °C). $Q_{10} = 2$ (a 10°C increase in temperature doubles the reaction), T_{AA}= 60°C (Accelerated Aging temperature), T_{RS}=37°C (Recommended Shelf temperature-Body temperature).The simulated age at 37°C is calculated using the equation $Age_{37°C} = (Age_{60°C})* Q_{10}^{[T_{AA}-T_{RT}]/10}$ (Hukins, Mahomed, and Kukureka 2008).

CHAPTER 5: MWCNT- RESULTS AND DISCUSSIONS

The results discussed here are an extension of the Master's thesis that demonstrated enhanced performance of electrophoretically deposited multi-walled carbon nanotubes through electrochemical techniques such as cyclic voltammetry and impedance spectroscopy (Minnikanti et al 2009).

Neural electrodes are required to maintain electrochemical properties in the aqueous of the nervous system. This includes electrical characteristics (charge and impedance) *in vivo* for a proper functioning of neural prostheses. Thus, investigations on *in vitro* versus *in vivo* performance of MWCNT electrodes were undertaken. The characterizations included electrochemical, surface, and early biological response towards MWCNT coated microwires including low-frequency stimulation acute experiments. As the objective was to evaluate the *in vivo* (rat hippocampi) performance of MWCNT electrodes, and to compare that performance with the *in vitro* results, the same protocol was used for *in vitro* and *in vivo* setups. The *in vivo* electrochemical characterization is what we are deeming as the low frequency stimulation owing to cyclic voltages (25 cycles of 0.7 V to 0.7 V at 50 mV/s). This is justified as neuronal activity can be modulated by applying low frequency electric fields (Radman et al. 2007). This modulation is proportional to the field amplitude and polarity (Radman et al. 2007;

Sunderam et al. 2006) Thus, by characterizing the electrode *in vivo* the inflammatory response can be also be assessed for a low amplitude and frequency stimulation protocol.

The early stages of neuro-inflammation due to mechanical and electrical trauma induced by implants can be better understood by detection of pro-inflammatory molecules rather than by histological studies. Inflammatory responses affect the mechanical and electrical stability of the implanted electrodes (Saxena et al. 2013). The inflammatory response was evaluated by reverse transcriptase- polymerase chain reaction analyses of Toll like receptors (TLR2) and pro-inflammatory cytokine Interleukin (IL)-1β transcripts expression levels, and contrasted to control animals. Both these molecules are associated with the inflammatory response (Perry 1994) of the CNS and are described in detail in the subsequent sections.

MWCNT coated microwires maintained their charge storage capacity (CSC) and impedance *in vivo* in the well-controlled, low-frequency stimulation acute experiments. Evaluation of inflammatory molecules revealed that transcripts for the cytokine IL-1β are upregulated in response to low-frequency stimulation, whereas no modulation was observed for TLR2. This result indicates that the early response of the brain to mechanical trauma and low-frequency stimulation activates the IL-1β signaling cascade but not that of TLR2.

5.1 Physiochemical Characterization and Bioavailability

The surface morphology of EPD MWCNT coatings on microwires was evaluated by a SEM operated at 5.00 kV. The resolution varied from 100 nm to 200 μm. Figure 5.1 shows the SEM images obtained from a single MWCNT coated electrode aged in air for

60 days. The images reveal homogeneous random entangled arrangement of MWCNT over the metal substrate. The nanotubes are oriented parallel to the surface of the stainless steel substrate. The bright spots are assumed to be the metal nanoparticles used as catalysts to grow MWCNTs. This particular result has raised several questions about the metal impurities present on the surface of the electrode coatings.

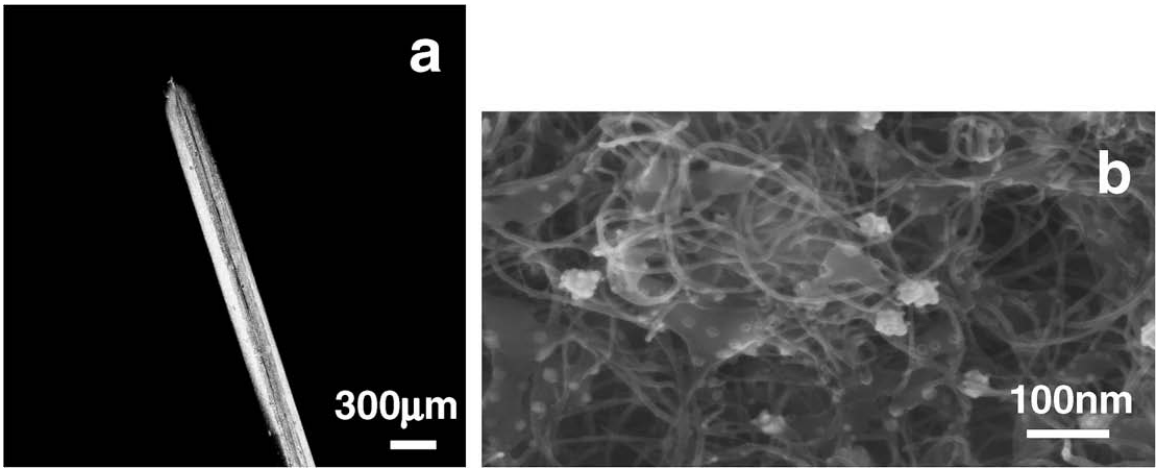

Figure 5.1: SEM image of a single bare stainless steel electrode after 10 min of electrophoretic MWCNT deposition. The bare electrode diameter is 250 µm. (b). SEM image at higher magnification of single bare stainless steel electrode after a 10 min electrophoretic MWCNT deposition. The MWCNT nominal diameter is 15 nm and length is longer than 20 lm. Homogeneous random entangled arrangement of MWCNT over the metal substrate is observed. The observed mesoporous matted structure over the electrode increases the effective area of the electrode. The bright spots are assumed to be metal nanoparticles used as catalysts to grow MWCNTs. (fig ref: Minnikanti et al 2009)

In order to quantitatively evaluate impurities in our samples, two additional analyses were performed, inductively coupled plasma atomic emission spectroscopy and

X-ray photoelectron spectroscopy. While the ICP-AES screens for metal catalysts, the XPS reveals the state of the surface of the MWCNT used for deposition.

Two grades of MWCNTs (research and industrial) were deposited on stainless steel substrates (Minnikanti et al 2009). Elemental analysis for the industrial and research grade suspensions used for EPD was achieved by inductively coupled plasma atomic emission spectrometer (ICP-AES). All the elements detected are listed in figure 5.2(a). Industrial grade MWCNTs had higher percentage of elements such as Al, B, Ca, K, Na, and Si (figure 5.2a). These can be associated with ceramic oxides, potential residual components in industrial grade MWCNTs. The elemental iron content in industrial grade MWCNTs was 1.91 wt%. Surprisingly, research grade MWCNTs presented with higher percentage of elemental Fe (2.10 wt%). XPS was performed using a custom-instrument predominantly composed of equipment from Perkin–Elmer (physical electronics division). Prominent peaks for carbon and oxygen are seen in the XPS spectrum of both research grade (figure 5.2b) and industrial grade (figure 5.2c), while peaks for metal catalysts were not detected.

a

Element	Industrial Grade wt%	Research Grade wt%
Al	1.431	0.123
B	1.446	0.682
Ca	2.395	0.892
Ba	0.005	-
Cu	0.204	0.276
Fe	1.915	2.103
K	1.312	1.007
Li	0.178	0.081
Mg	0.375	0.142
Mo	0.343	0.814
Na	2.353	0.725
P	0.254	0.202
Pb	-	0.213
S	1.130	0.452
Si	4.556	2.172
Sr	0.007	-
Ti	0.015	0.039
Zn	0.109	0.655

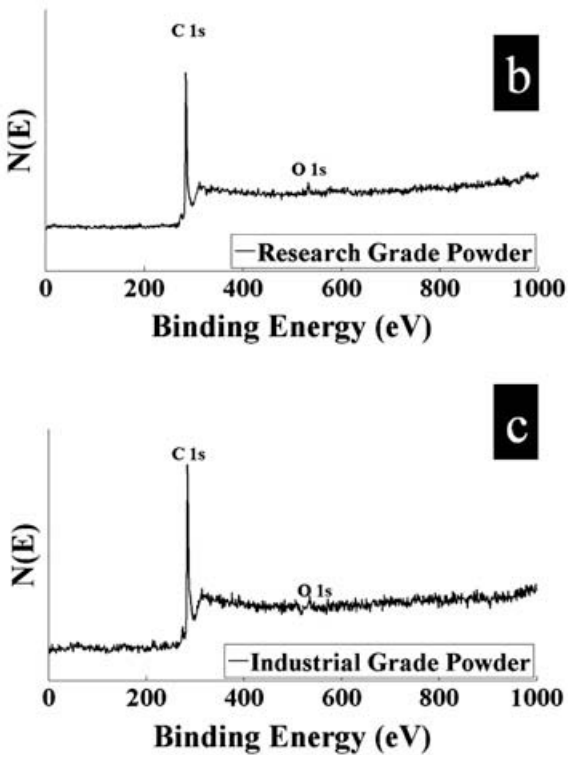

Figure 5.2: (a) ICP-AES elemental analysis of industrial and research grade MWCNT suspensions used for electrode coatings. ICP analysis realized in the Research Analytical Laboratory (Univ. Minnesota, MN). The following elements were present at quanties below the minimum detection level : Ni, As, Be, Cd, Co, Cr, Mn, Rb, and V electrodes (b). XPS of research grade MWCNT. (c). XPS of industrial grade MWCNT. The surface composition of samples shows in (b) and (c) is indistinguishable, presenting 97.5% (industrial) and 98% (research) carbon content. The other peak in each spectrum refers to oxygen.

SEM images of MWCNT electrodes aged in PBS and explanted after an acute implantation period were also obtained. Figure 5.3(a) and (b) show the SEM images obtained from a single MWCNT-coated electrode aged in PBS for 60 days. The images reveal homogeneous random entangled arrangement of MWCNT over the metal substrate. The nanotubes are oriented parallel to the surface of the stainless steel

substrate. Several layers of a carbon nanotube mesh cover the stainless steel surface in all coated electrodes. Figure 5.3(c) and (d) present the SEM image of an explanted electrode after an acute implantation period (30 min implant time). Figure 5.3(e) and (f) show an explanted electrode used for stimulating hippocampus (45 min stimulation). Explanted electrodes presented a more condensed mesh. Due to superficial cleaning, other biological species were present adsorbed to the mesh. When no cleaning is performed, crystals are visible on the surface of the electrode (data not shown). The images show that the nanotube-coated electrodes lasted through the shear forces of insertion and extraction through the dura mater, as well as the protective layering of the brain. The difference between implanted and non-implanted electrode surfaces was clear: there was no debris on the non-implanted electrodes. It was expected to see several surface modifications due to mechanical stress on the surface of the MWCNT mesh. The MWCNT mesh withstood implantation, indicating the robustness of the adhesion of this film to the stainless steel surface, successful implant and extraction procedures used during surgery.

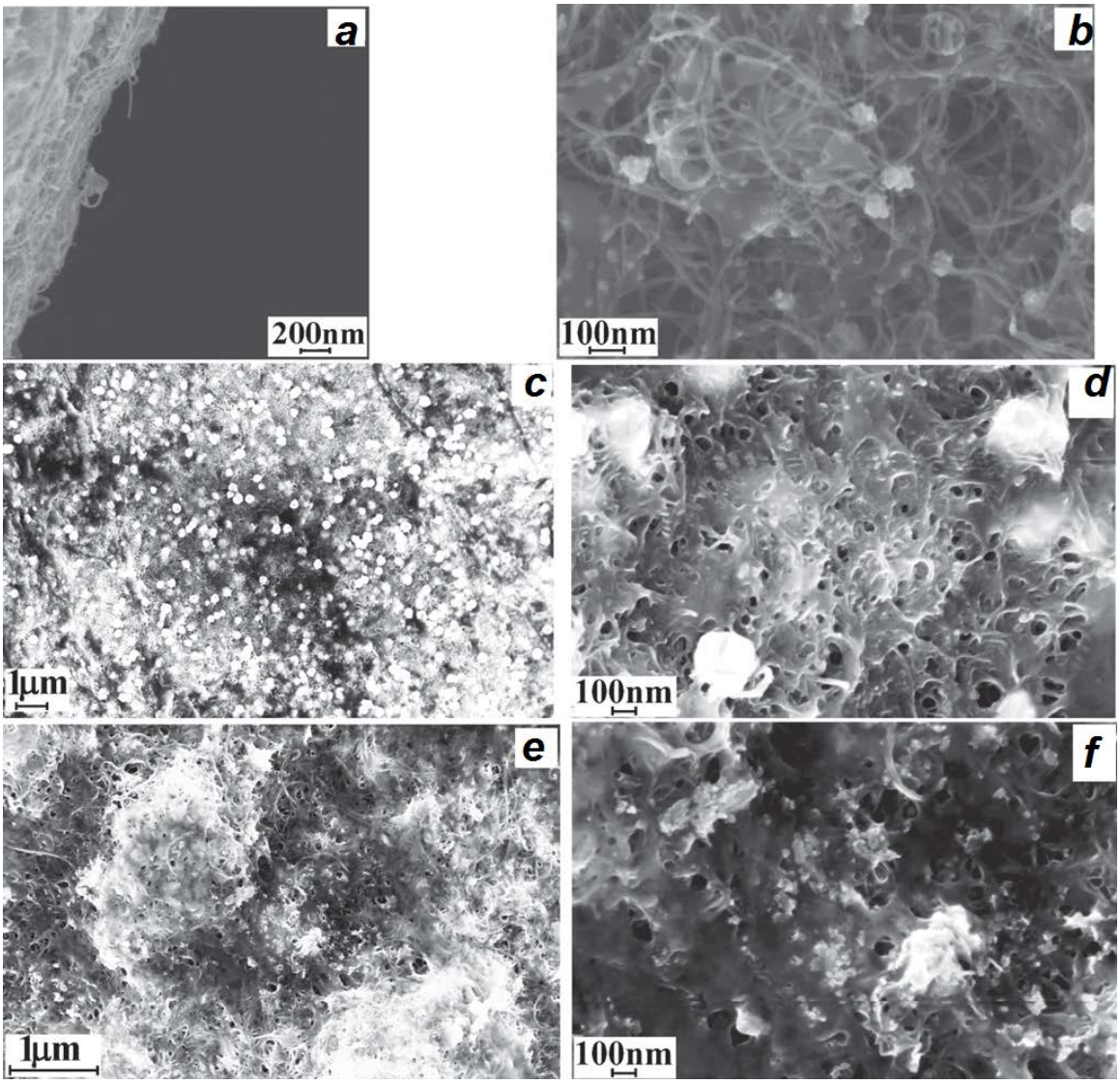

Figure 5.3: Electrode surfaces are modified by coatings. Several layers of a carbon nanotube mesh cover the stainless steel surface in all coated electrodes. (a and b) SEM of as-prepared MWNT electrode. (c-d) Explanted electrode, after acute implant, with no stimulation (30min implant time). (e-f) Explanted electrode, after implant and stimulation of hippocampus (45 min stimulation). Explanted electrodes present a more condensed mesh. Despite superficial cleaning, other biological species are still present, and remain adsorbed to the mesh. When no cleaning is performed, crystals are also visible (data not shown) (fig ref: Minnikanti et al. 2010).

5.2 Early biological response

Insertion of an electrode in the brain closely mimics a penetrating wound by severing capillaries, thus causing rapid destruction of neurons and glia (Perry 1994; Liu et al. 1999; Polikov, Tresco, and Reichert 2005). The trauma activates cellular mechanisms in order to maintain homeostasis (Anderson 2004). The macrophages in the vicinity of a stab wound of the CNS will immediately secrete members of IL-1 family and other pro-inflammatory factors that promote astrogliosis (Perry 1994). Astrogliosis leads to the reactive glial scar tissue formation, which has been shown, with histopathological techniques, to extend over weeks to years (Polikov, Tresco, and Reichert 2005)(Griffith and Humphrey 2006).

Some of the molecules involved in orchestrating the early body response to damage are TLRs (Olson and Miller 2004). IL-1β is one of the agonist members of the prototypic inflammatory cytokine IL-1 family (Rothwell and Luheshi 2000)(Didier et al. 2003). Following neurotrauma, IL-1 can be detected in the extracellular space within 60 min, peaking at the second day after the trauma (Fassbender et al. 2000). The signaling response to TLR stimulation shares features with IL-1 receptor signaling (Owens et al. 2005). While these are general response mechanisms in the CNS, little is known of the actual molecular mechanisms and the time-course by which the brain's immune response is activated upon implantation of electrodes. Tracking of such response over time would profit from better analysis methods over several temporal and spatial scales (Saxena et al. 2013).

However, traditional techniques to assess this tissue response remove the implant and the adjacent neural tissue and analyze them at various points in time (Griffith and Humphrey 2006). The histopathological evaluation involves sectioning, staining (Szarowski et al. 2003), and identifying cell number, location, type, and by-products (Turner et al. 1999) (Biran, Martin, and Tresco 2005). Although traditional methods assess the biocompatibilty and inflammatory responses, they are qualitative. This problem can be overcome by evaluating the expression of key molecules involved in the signaling cascades of neuroinflammatory response for example. Measuring mRNA levels using RT-PCR helps in quantifying the expression of production and release of any protein (cytokines or receptor).

As the main objective of these experiments was to evaluate the *in vivo* performance of MWCNT electrodes, and to compare that performance with the *in vitro* results, we designed a protocol and applied it with no modifications to both the *in vitro* and *in vivo* setups. The model we follow is electrode-based, rather than animal-based, and therefore the choice of repeating the stimulation protocol in a buffered electrolyte solution and during the acute surgery is justified, if not required. MWCNT electrodes were first implanted and then used for sub-threshold low-frequency stimulation of the hippocampus. The inflammatory response was evaluated by RT-PCR analyses of TLR2 and IL-1β transcripts expression levels, and contrasted to control animals.

5.2.1 TLR2

TLRs are part of a family of receptors known to be involved in pathogen-dependent responses in the innate immune system (Olson and Miller 2004) by recognizing the molecular sequences found in microbes, such as bacteria, fungi, and viruses. TLRs drive the innate responses, and the downstream signaling cascades involved are significant determinants of inflammatory responses occurring within the CNS (Jack et al. 2005), but recent data suggest that non-pathogenic molecules endogenously released by an injury can also trigger inflammatory cascades via TLR2 (Babcock et al. 2006). TLR2, as well as other TLRs, acts as an innate bridge to neuro-inflammation, leading to transcription of proinflammatory cytokines (e.g. IL-1β) and chemokines, and to up-regulation of cell surface molecules involved in the initiation of adaptive immune responses (Carpentier et al. 2005). TLR2 is constitutively expressed in the hippocampus as RT-PCR results show that the levels of mRNA were easily detectable in all controls and in non-manipulated and in contralateral hippocampi. TLR2 transcripts were not upregulated after low frequency stimulation. The statistical analysis showed that neither MWCNT implantation nor charge application (25 CV cycles and EIS) was capable of yielding statistically significant ($p > 0.05$, $n = 4$) up-regulation of TLR2 mRNA levels (figure 5.4). The averaged results of expression levels of transcripts for TLR2 are presented in table 5.1 .

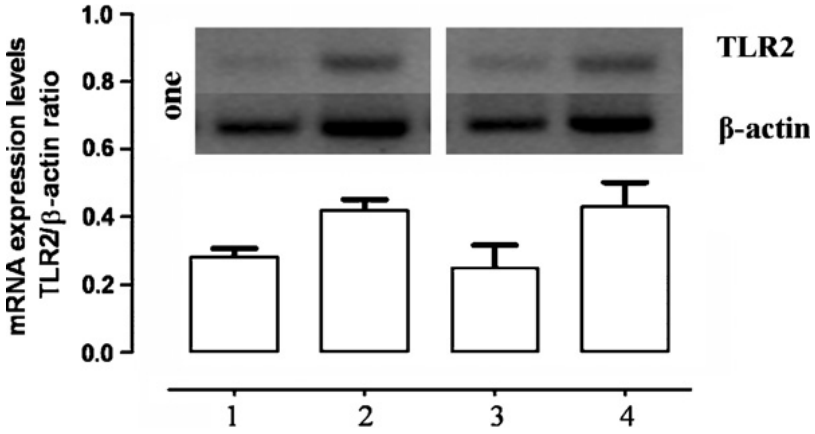

Figure 5.4: Expression levels of transcripts for toll-like receptor 2 (TLR2). The upper panel shows agarose gel representing the profile of RT-PCR product after amplification of TLR2 and β-actin transcripts for n=1 sample. The lower panel is the histogram representation for of n=4 samples. Groups are: (1) control group (not implanted), right hippocampus; (2) control group, left hippocampus; (3) CNT group, right (contralateral) hippocampus and (4) CNT group, left hippocampus (implanted hippocampus). N=4. Data were analyzed by one-way ANOVA (Newman-Keuls), p >0.05 (fig ref:Minnikanti et al 2010).

Table 5.1: Descriptive Statistics for TLR2 and IL-1β (Minnikanti et al 2010)

Group	mRNA levels (ratio of arbitrary units)[a]
TLR2/β-actin from control right hippocampus	0.28±0.05
TLR2/β-actin from control left hippocampus	0.41±0.07
TLR2/β-actin from right hippocampus (implanted animal, contralateral structure)	0.36±0.39
TLR2/β-actin from left hippocampus (implanted and stimulated, ipsilateral structure)	0.38±0.15
IL-1β/β-actin from control right hippocampus	0.42±0.19
IL-1β/β-actin from control left hippocampus	0.45±0.19
IL-1β/β-actin from right hippocampus (implanted animal, contralateral structure)	0.54±0.17
IL-1β/β-actin from left hippocampus (implanted and stimulated, ipsilateral structure)	1.41±1.16

[a]Arbitrary units for band density corresponding to the quantity of fragments of each mRNA, represented as the ratio target mRNA / β-actin.

5.2.2 IL-1β

IL-1β is also an important microglial effector cytokine (Hanisch 2002). Pro-inflammatory cytokine IL-1β is, like TLR2, constitutively expressed in the hippocampus and was easily detectable by RT-PCR in all controls and in non-manipulated and contralateral hippocampi (figure 5.5). However, unlike TLR2 its mRNA expression level was upregulated in the implanted hemisphere after 3 h, as compared with the un-implanted hippocampus in the contralateral hemisphere of the brain (figure 5.5). This result was statistically significant ($p < 0.05$, $n = 4$) when compared with the contralateral hippocampus of the implanted animal, as well as with any of the control animals. The averaged results of expression levels of transcripts for IL-1 β are presented in table 5.1**.**

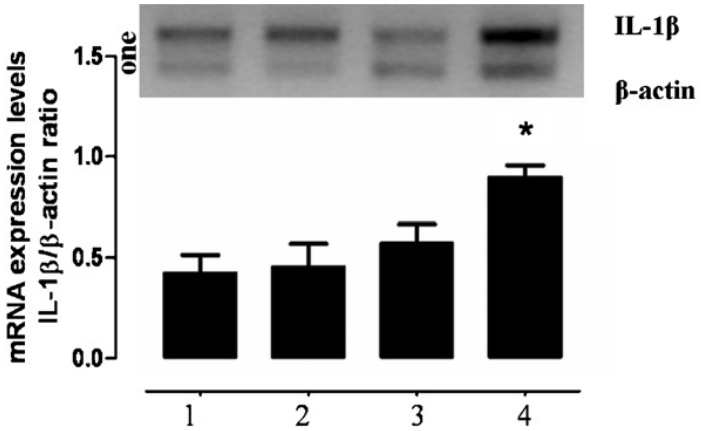

Figure 5.5: Expression levels of transcripts for interleukin 1-β (IL-1β). The upper panel shows agarose gel representing the profile of RT-PCR product after amplification of IL-1β and β-actin transcripts for n=1 sample. The lower panel is the histogram representation for of n=4 samples. Groups are: (1) control group (not implanted), right hippocampus; (2) control group, left hippocampus; (3) CNT group, right (contralateral) hippocampus, and (4) CNT group, left hippocampus (implanted hippocampus). N=4. Data were analyzed by one-way ANOVA (Newman-Keuls), * indicates $p < 0.05$ (fig ref: Minnikanti et al 2010).

5.3 Cyclic Voltammetry

MWCNT-coated electrodes deliver higher charge than stainless steel electrodes. The cyclic voltammetric spectrum of a typical MWCNT-coated electrode (figure 5.6) in comparison with bare electrode shows an increase in the enclosed area of the curve. The averaged (n=10) CSCc results were as follows: stainless steel 5.89 ± 1.67 μC/ mm^2 and MWCNT coated 9.65± 2.70 μm/mm^2. The CSCc for bare and MWCNT deposited electrodes were calculated and statistically compared using Wilcoxon signed-rank test (n=10). The CSCc of bare electrodes significantly increased ($p < 0.05$ or P-value = 0.005,

two tailed) after MWCNT deposition, for example for the MWCNT electrode of figure 5.6 the CSCc increased from 0.488 mC cm^2 to 0.996 mC cm^2.

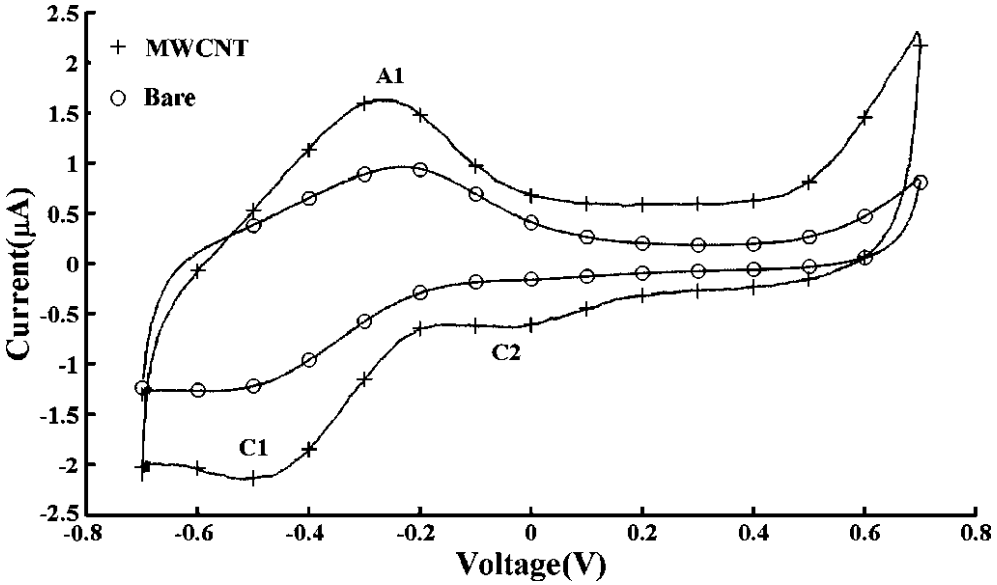

Figure 5.6: Cyclic voltammogram (CV) of a single bare stainless steel electrode stars (o) in comparison to that of a MWCNT deposited electrode (+).CV measurement taken with a three electrode setup in PBS (pH 7.4) solution and Ag/AgCl as the reference electrode and Pt foil as the counter electrode, at a scan rate of 50 mV/s. Cathodic area under the CV curve denotes the CSCc value. For the bare stainless steel electrode, CSCc=4.88 μC/mm^2; for the MWCNT coated electrode, CSCc= 9.96 μC/mm^2 (fig ref: Minnikanti et al 2010).

Figure 5.7 presents the comparison of *in vitro* and *in vivo* cyclic voltammogram of a typical MWCNT-coated electrode. For this particular electrode, the CSC is 12.05 μC

mm^2 *in vitro* and 12.73 µC mm^2 *in vivo*. Statistical analysis showed no significant change ($p > 0.05$ or P-value = 0.715, two tailed) in the CSC for MWCNT electrodes (n = 4) *in vivo* when compared against their *in vitro* performance. The difference in average CSCc (n = 4) between the *in vivo* 11.11 ± 4.01 µC mm^2 (mean ± s.e.m) and *in vitro* 10.80 ± 2.83 µC mm^2 (mean ± s.e.m) model was statistically insignificant ($p > 0.05$ or P-value = 0.715, two tailed).

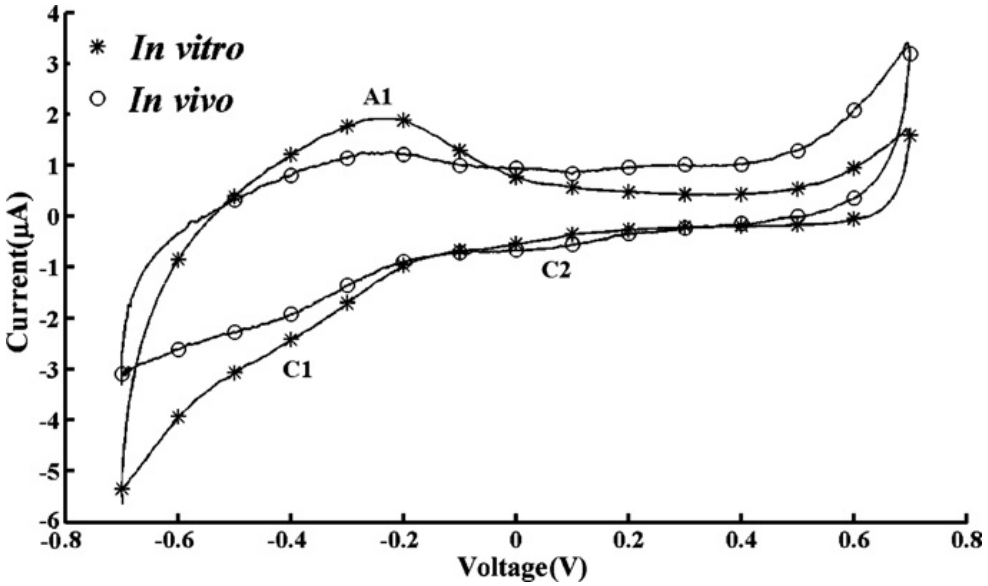

Figure 5.7: CV spectrum of implanted MWCNT electrode (○) in comparison to *in vitro* (*) MWCNT electrode. Redox peaks at the same excitation voltages point to similar morphology of the electrolyte-electrode interface. Charge storage capacity in both situations is also comparable: *in vivo* MWCNT CSCc=12.05 µC/ mm^2 and *in vitro* MWCNT electrode CSCc= 12.73µC/ mm^2 (fig ref:Minnikanti et al 2010).

5.4 Electrochemical Impedance Spectroscopy

Statistical analyses comparing *in vitro* and *in vivo* EIS at frequencies 0.2 Hz, 2 Hz, 20 Hz, 200 Hz and 2 kHz show that the impedance modulus and phase (n=4) were not significantly different ($p > 0.05$, two tailed). In particular, P-values at 0.2 Hz, 2 Hz, 20 Hz, 200 Hz and 2 kHz were, respectively, 0.465, 1, 0.144, 0.465 and 0.068. Figure 5.8 shows the impedance modulus and phase Bode plots comparing *in vitro* and *in vivo* for a MWCNT electrode.

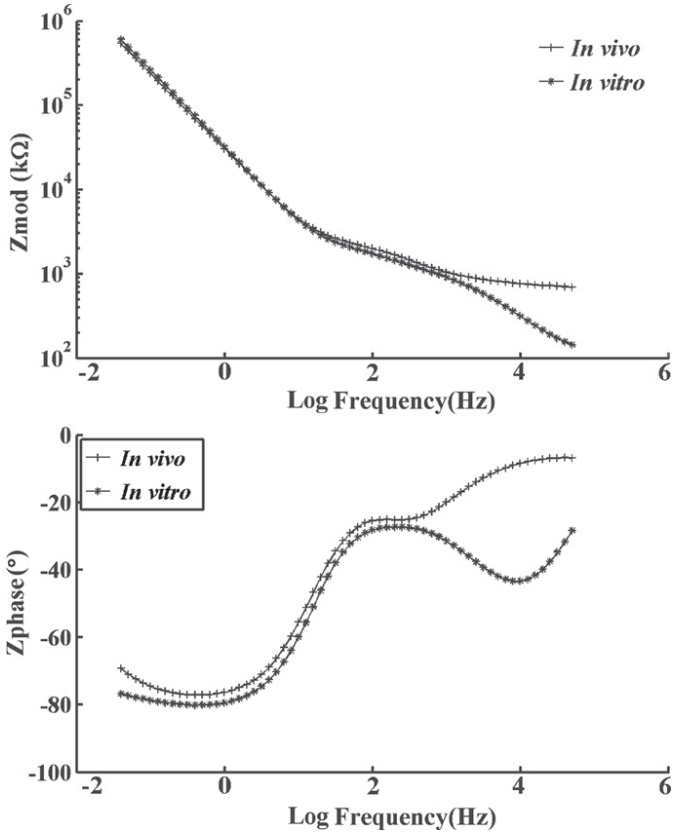

Figure 5.8: Bode plots of (a) impedance modulus and (b) impedance phase for *in vivo* (+) MWCNT electrode and *in vitro* (*) MWCNT electrode. At lower frequencies the electrode behavior does not change, however, at higher frequencies the impedance tends to increase (fig ref:Minnikanti et al 2010).

5.5 Conclusions

MWCNTs can be electrophoretically deposited over stainless steel electrodes for stimulation of biological tissue. The electrode surface area increases with the MWCNT deposition (figure 5.6), thus allowing for higher CSCc, but the underlying electrochemistry is preserved, and the reduction-oxidation peaks observed in the metallic substrate are maintained after MWCNT coating (figure 5.6)(Minnikanti et al 2009). *In vivo* electrochemical characterization of MWCNT electrodes shows that they also

maintain their CSCc and redox peaks upon implantation (figure 5.7). This behavior is contrary to traditional stimulation electrodes such as iridium oxide, where a 30 % decrease in charge delivered is observed (chapter 6).

The electrochemical behavior of CNTs is dependent on its impurities (metal catalysts) (Banks et al. 2006; Niessen, Jonge, and Notten 2006), structural defects (Portet, Yushin, and Gogotsi 2007), pre-treatment, orientation, and the amount of available adsorbed species on its sidewalls and open ends (Gooding 2005). CNTs with greater amount of metal catalysts show superior electrochemical behavior if compared to purified nanotubes (Niessen, Jonge, and Notten 2006). However, the experiments show no significant difference in the performance of research and industrial grade was observed with respect to CSCc and impedance. Probably the orientation of the nanotubes in relation to the surface is one of the reasons for the industrial and research grade nanotubes to behave similarly. Both CV and EIS spectra show that the adsorbed species and metal catalysts do not play a major role in charge transfer in EPD deposited MWCNT coatings on microwires in *in vitro* scenarios.

Inflammatory molecules and glia cells around the implant tend to increase the impedance of the electrode (Polikov, Tresco, and Reichert 2005). It has been reported in the literature that astrocyte adhesion, while taking part in glial scar formation, was less prominent in neural implants made up of carbon nanofibers (Webster et al. 2004). Studies have shown that physical topology of an implant affects the protein adsorption and cellular interaction (Woo, Chen, and Ma 2003). When *in vivo*, the electrodes interact with neural tissue consisting of neurons bound by scaffolds of extracellular matrix (ECM).

The ECM consists of mostly interwoven protein fibers of nanometer length scale randomly oriented (Ayad et al. 1998). Surfaces with nanoscale features are being investigated as next generation materials in tissue scaffolding and neural regeneration (Harrison and Atala 2007). Traditional electrodes such as stainless steel and iridium oxide have smooth surfaces (Green et al. 2008) whereas the deposited MWCNT have fibrillar and present random orientation (figure 5.3). This closely resembles the topology of the extracellular matrix. This similarity could be one of the reasons that neural tissue and MWCNT interact in a fashion that is conducive and non-interfering for *in vivo* charge transfer.

The *in vivo* environment and the inflammatory molecules initially active at the electrode-nervous tissue interface and do not increase the impedance of MWCNT electrodes. The increase in impedance is at higher frequencies (> 2 kHz) and this is associated with tissue properties. EIS performed *in vitro* and *in vivo* showed that the impedance modulus was not significantly different ($p>0.05$) when electrode are implanted in deep brain structures. This behavior is unlike that observed in traditional electrodes.

Neurons *in vitro* are sensitive to the different functional groups attached to the CNT surface (Webster et al. 2004)(Wei et al. 2007). Both non-functionalized (data not presented) and -COOH functionalized MWCNT present the same charge carrying behavior in acute *in vivo* experiments. Thus, it seems that long as the final interface is composed of nanotubes, and so long as it exhibits CNT-like electrochemistry, it has stable electrical and mechanical characteristics, in solution or in the biological tissue.

An inflammatory response involving a series of molecular and cellular events including the production and release of neuro-inflammatory cytokines occurs as soon as the electrode is implanted (Polikov, Tresco, and Reichert 2005). The quantification of transcripts (mRNA) also allows the detection of very early modulatory events in such a tissue, organ or cell, as we show here. Two of the key molecules involved in the signaling cascades for inflammatory responses to damage in the central nervous system are TLR2 (Babcock et al. 2006) and IL1-β (Hanisch 2002) (Didier et al. 2003).

The transcription levels of TLR2 in the contralateral hippocampus of the experimental group were not up-regulated (figure 5.4). The transcription levels of TLR2 (figure 5.4) in the implanted and stimulated hippocampus were not significantly different ($p > 0.05$, ANOVA) (table 5.1) when compared with controls and contralateral hippocampus. This suggests that the electrode insertion, MWCNT, voltammetry and low amplitude stimulation by themselves do not trigger the early inflammatory response involving TLR2. The interesting result is that IL-1β transcription levels (figure 5.5) were significantly increased ($p<0.05$, ANOVA) for the MWCNT implanted hippocampus when compared with the control group and contralateral hippocampus (table 5.1). This response need not be necessarily as a reaction to MWCNT and more due to blood brain permeation due to electrode insertion (Saxena et al 2013). The results discussed in this chapter lead to two publications (Minnikanti et al 2009, 2010) and a review chapter (Minnikanti and Peixoto 2011).

CHAPTER 6: EIROF-RESULTS AND DISCUSSIONS

6.1 Overview

The objective of this chapter is to demonstrate that two models fit the impedance spectra of electrodeposited iridium oxide coated microwires depending on the application of slow CV cycle (-0.7 V to 0. 7 V at 50 mV/s) stimulation prior to EIS measurement for *in vitro* and *in vivo* scenarios. As it was shown that current pulsing *in vivo* changed the impedance of SIROF electrodes (Weiland and Anderson 2000), we were interested to see if slow CV cycles a traditional method to evaluate electrodes affected the impedance for EIROF electrodes. Additionally, for un-stimulated (CV) iridium oxide microwires the high frequency and full spectrum *in vivo* equivalent circuit model differed from its *in vitro* model by a parameter element. The performance of EIROF tested *in vitro* and *in vivo* were evaluated using the following figures of merit (1) lowering of impedance, as shown by EIS curves, (2) increase in charge storage capacity, as given by CV curves, and (3) open circuit potential measured prior to EIS. Graphical methods and equivalent circuit help in interpreting the changes in the impedance in simple electrical terms. The goal is here to quantify and understand what electrical properties of EIROF micro-wires change in moving from PBS (*in vitro*) into a rodent hippocampi (*in vivo*) scenario. As this was an acute study, the immediate changes in impedance of the electrode are not confounded by the changes in electrical behavior associated with glial scar (Grill and Mortimer

1994)(McConnell, Butera, and Bellamkonda 2009)**.** Traditionally, a DC bias is applied while measuring EIS to activate the iridium oxide films (Weiland and Anderson 2000; Cogan 2006). As the focus of the study was to understand the changes of impedance of the coated electrode in its native state, DC bias was not applied during any of the EIS measurements. All electrodes used for comparison had roughly the same surface area.

6.2 Cyclic Voltammetry

EIROF microwires (n=10) were implanted in a rodent brain. The cathodic and anodic charge storage capacity (CSCc, CSCa) were measured via CVs prior and post to implantation in PBS and in rat brain (table 6.1). All CVs were conducted prior to EIS measurements and used a three electrode setup. The CSCc of iridium oxide layers has been shown to be directly proportional to its thickness (Meyer et al 2001). Judging by the relative standard error of CSCc the difference in thickness of EIROF was around 12 % across the samples. Experiments to investigate the thickness of layers EIROFs over the substrates were not carried out.

Table 6.2: Summary of the *in vitro* and *in vivo* CSCc and CSCa with corresponding standard error means. The columns summarize the results for set up, along with the standard error means, while column three shows the percentage decrease in the CSC from *in vitro* to *in vivo.*

	In vitro (n=9) mean ± s.e.m	***In vivo (n=9) mean s.e.m***	***% decrease***
CSCa (µC)	392.24 ± 47.39	270.50 ± 35.84	30.65 ± 3.83
CSCc (µC)	382.65 ± 49.52	259.67 ± 36.09	31.37 ± 4.38

All implanted EIROF microwires demonstrated a decrease in the charge delivered to the tissue to 30% of the *in vitro* CSCc (table 6.1). A 1 mC/mm^2 CSCc electrode tested *in vitro* would drop to 0.30 mC/mm^2 *in vivo*. This decline is observed in the cyclic voltammetry immediately after implantation; a typical example of that is shown in figure 6.1.

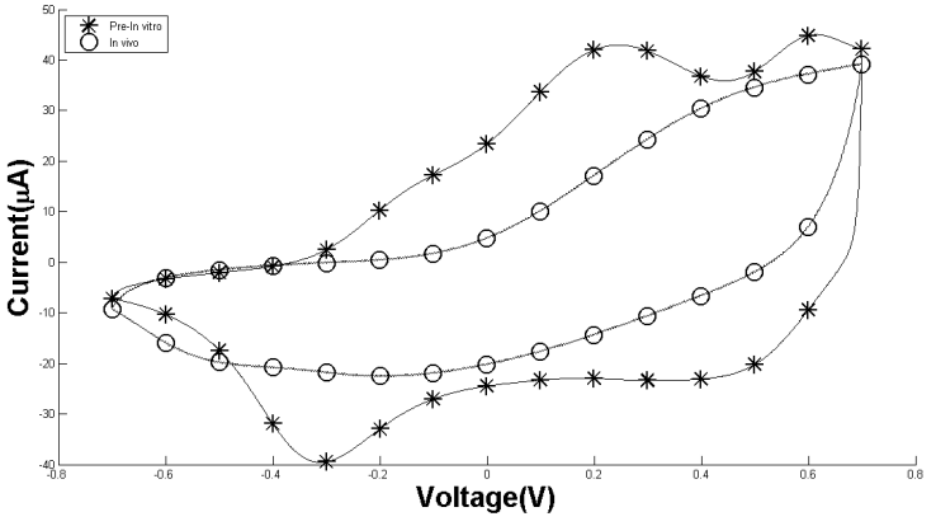

Figure 6.1: Cyclic voltammetric spectrum of implanted iridium oxide electrode (○) in comparison to *in vitro* (*) electrode. A three electrode setup is used with Ag/AgCl pellet as reference and Pt foil as counter electrode. The *in vitro* test is realized in phosphate buffered saline at pH 7.4, and the *in vivo* measurement is taken in the hippocampus while the skull is bathed in sterile saline solution (0.9%). Loss of the reduction and oxidation peaks *in vivo* is indicative of biofouling and non-conducive environment for Faradaic charge transfer, leading to a decrease in the charge storage capacity. In this example, the cathodic charge storage capacity (CSCc) decreases from an *in vitro* of 628.1 μC/mm^2 to *in vivo* of 407.7 μC/mm^2 (fig ref:Minnikanti et al 2010).

The reduction-oxidation peaks, characteristic of the valence-changing iridium oxide at the surface, are gone or reduced when the electrode is implanted in the brain. This signifies an absence of an electron-limited transfer. This is true for any brain structure tested by our group. However, Cogan et al (2006) reported that the *in vivo* charge transfer was "facile *in vivo*" in comparison to inorganic interstitial fluid. There was no loss of redox peaks on the *in vivo* CVs (50 mV/s), but a shift in the peaks was observed. However, the difference could be attributed to the fact that the AIROF microelectrodes were tested in subretinal space that presents a different environment compared to deeper brain structures. Our group has consistently seen a decrease in CSCc as well as a decrease or absence of redox peaks in rat hippocampus. As we have previously demonstrated, this reflects a loss of mass-transfer capacity at the electrode-electrolyte interface (Zaidi et al. 2010). The electrode behavior is recovered once it is explanted from the brain and once its surface is properly cleaned. This rejects the hypothesis that the insertion through the dura-mater damages the coating of the electrodes.

6.3 Electrochemical Impedance Spectroscopy

EIROF covered microwires (n=12) were implanted in rodent hippocampi in an acute study. EIS and CV were performed before, during, and after implantation for n=6 electrodes and hereafter will be named as **Stimulated group (groupB)**. Here the slow 25 CV cycles (50 mV/s) between -0.7 V and 0.7 V are deemed as stimulation. While only EIS was measured before, during and after implantation for n=6 electrodes and hereafter will be named as the **un-Stimulated group (groupA)**. Impedance data presented here

represented either in complex impedance-plane or Nyquist formats and Bode representation or impedance-modulus and phase versus frequency in a logarithmic scale.

6.3.1 *In vitro* performance

Two sets of impedance spectra emerged from EIS data collected from electrodes, identified as Stimulated and un-Stimulated group. A prominent impedance phase peak is seen in the high frequency range (1-10 kHz) for un-stimulated group (figure 6.2) while for stimulated group two transitions points are visible in the impedance phase between 1-10 Hz and 100 Hz-1 kHz (figure 6.3). The transition point is defined as where the derivative of the phase curve w.r.t. to the frequency is zero (stars in figure 6.2-6.3). Interestingly, the open circuit potentials (Eoc) for un-stimulated group was positive with an average of 326 ± 112 mV (mean ± s.e.m), whereas the electrode with least Eoc of 34 mV presented the highest impedance across the frequency spectrum and having a phase spectrum matching stimulated group. Stimulated group had negative Eoc (-73.84 ± 0.85 mV).

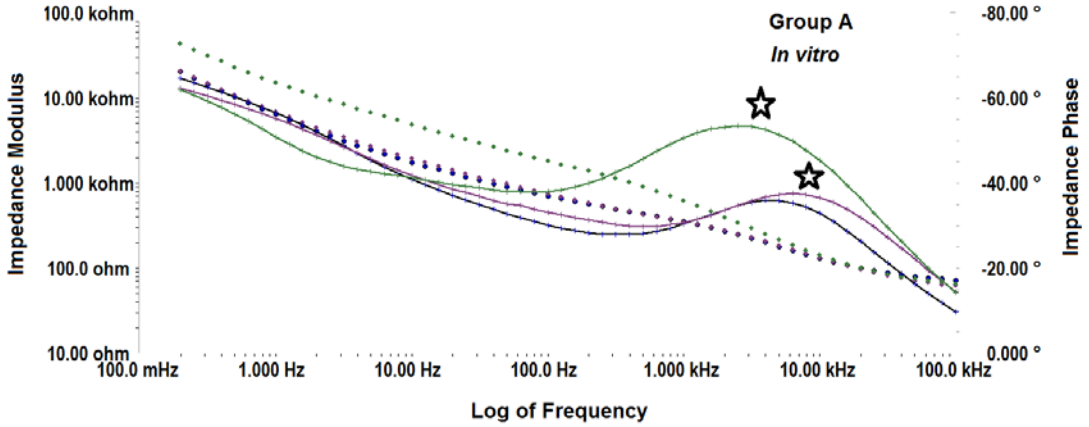

Figure 6.2: An overlay of impedance modulus (dotted curves) and impedance phase (solid curves) of un-stimulated (groupA) (n=3) electrodes in *in vitro* set up. EIS measurements use a three electrode setup in phosphate buffered saline solution (pH 7.4) with Ag/AgCl as the reference electrode and platinum foil as counter electrode. The frequency was swept from 200 mHz to 50 kHz. Phase transition points (star) are seen between 1 kHz - 100 KHz.

The impedance modulus for stimulated group was higher than un-stimulated, for example the average impedance modulus at 1Hz for un-stimulated group is 6 kΩ, at least, 2 times lower than stimulated. This behavior is in accordance with the conductivity of hydrous iridium oxide films being larger at higher potentials (Cogan 2009). Additionally, the un-stimulated EIROFs were deposited via ultrasonication. Whether this affects the conductivity of the EIROF films is yet to be investigated.

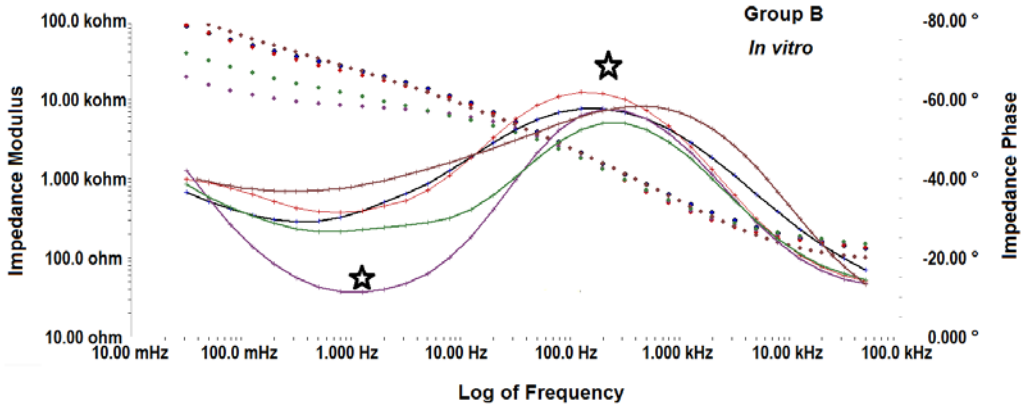

Figure 6.3: An overlay of impedance modulus (dotted curves) and impedance phase (solid curves) of stimulated (groupB) (n=4) electrodes. EIS measurements use a three electrode setup in phosphate buffered saline solution (pH 7.4) with Ag/AgCl as the reference electrode and platinum foil as counter electrode. The frequency was swept from 50 mHz to 50 kHz. Two phase transition points (star) between 100 mHz - 10 Hz and 100 Hz - 10 kHz are seen.

6.3.2 *In vivo* performance

The un-stimulated group shows an increase in impedance modulus (figure 6.4) across the frequency spectrum, it increase as much as 10 times at 10 kHz. While the stimulated group *in vivo* impedance modulus increases significantly for frequency ranges above 1 KHz and below 10 Hz, but in the mid frequency range it is comparable.

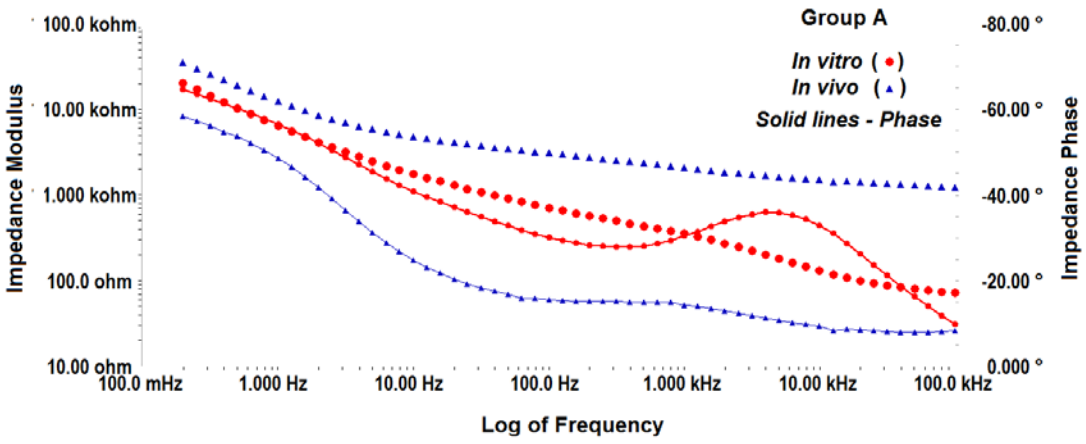

Figure 6.4: An overlay of *in vitro* (red) and *in vivo* (blue) impedance modulus and impedance phase (solid lines) of a representative electrode from un-stimulated group. EIS measurements use a three electrode setup in phosphate buffered saline solution (pH 7.4) with Ag/AgCl as the reference electrode and platinum foil as counter electrode. The frequency was swept from 200 mHz to 50 kHz. An increase in the impedance modulus and phase is seen across the measured frequency spectrum as the electrode is placed in rat brain. Additonally, flattening of the phase curvature between 1- 100 kHz is clearly visible.

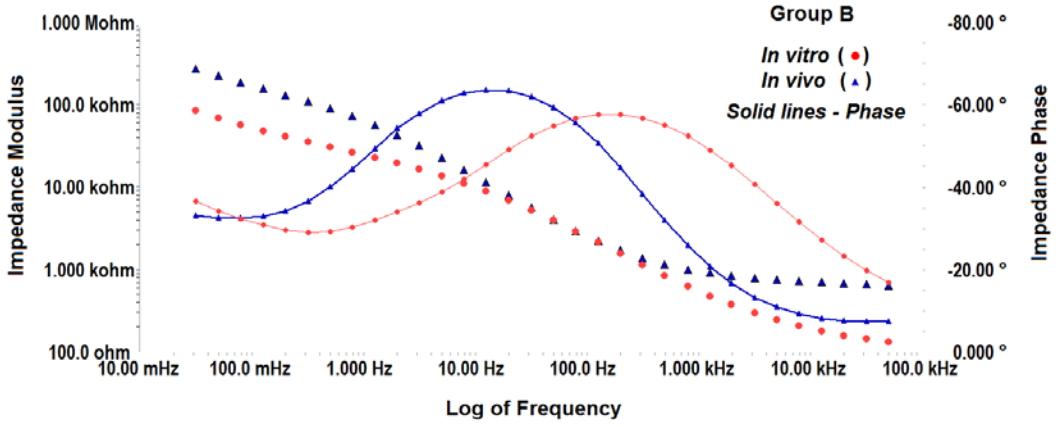

Figure 6.5: An overlay of *in vitro* (red) and *in vivo* (blue) impedance modulus and impedance phase (solid lines) of a representative electrode from stimulated group (groupB). EIS measurements use a three electrode setup in phosphate buffered saline solution (pH 7.4) with Ag/AgCl as the reference electrode and platinum foil as counter electrode. The frequency was swept from 50 mHz to 50 kHz. An increase in the impedance modulus is seen only in low (< 10 Hz) and high (> 1 kHz) frequency range, while the phase increases in the low to mid frequency range and decreases at frequencies > 100 Hz. is seen across the measured frequency spectrum as the electrode is placed in rat brain. Additionally, a shift in phase peak is seen towards lower frequencies.

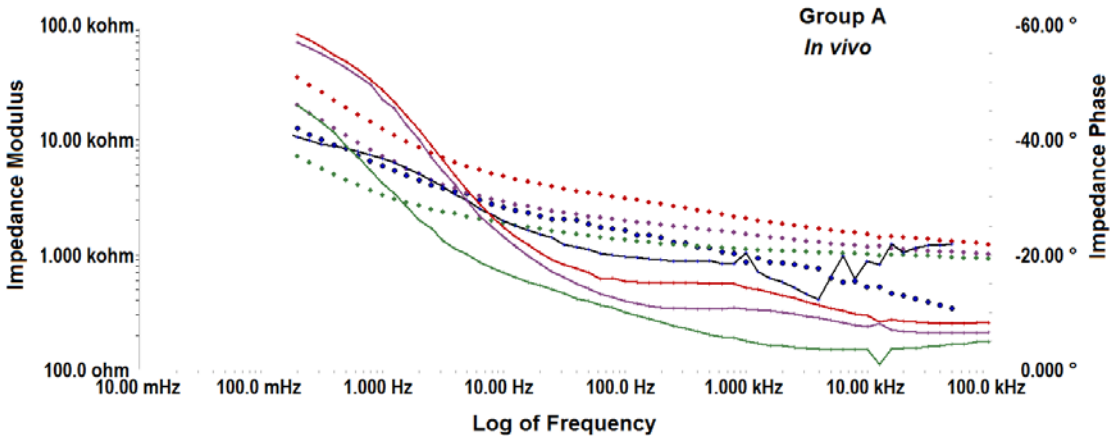

Figure 6.6: An overlay of *in vivo* impedance modulus (dotted curves) and impedance phase (solid curves) of un-stimulated (groupA) (n=4) electrodes. EIS measurements use a three electrode setup with Ag/AgCl as the reference electrode and platinum foil as counter electrode. The frequency was swept from 50 mHz to 50 kHz.

Stimulated group maintains its *in vitro* phase spectrum except for the shifts in the phase transition point towards lower frequencies *in vivo* (figure 6.5). The *in vitro* phase at high frequency (100 Hz-10 kHz) transition point is capacitive (closer to 0°) shifts towards mid frequencies (10–100 Hz) *in vivo*. Thus, the mid frequency resistive nature diminishes and a capacitive behavior dominates this region *in vivo* in comparison to *in vitro.* The 100 – 10 kHz frequency region is associated with the charge transfer redox reactions in the EIROF (Weiland and Anderson 2000).

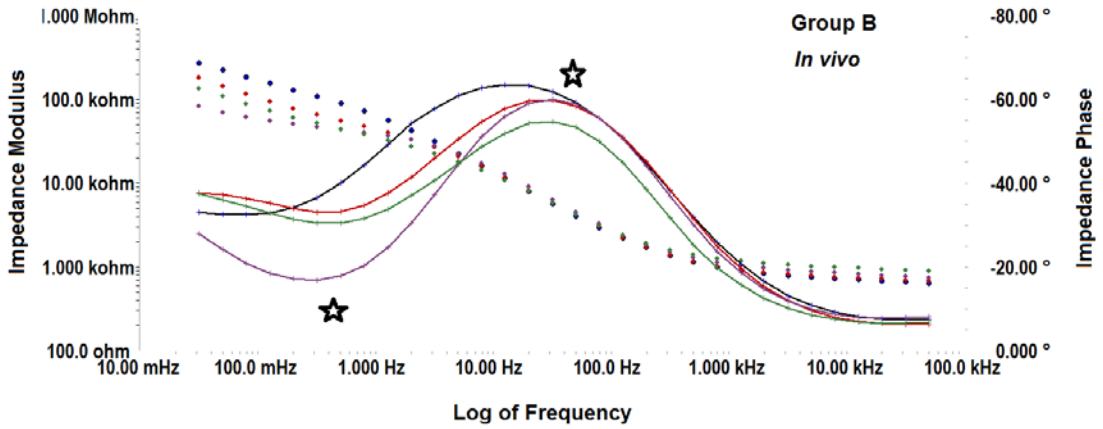

Figure 6.7: An overlay of *in vivo* impedance modulus (dotted curves) and impedance phase (solid curves) of stimulated (n=4) electrodes. EIS measurements use a three electrode setup with Ag/AgCl as the reference electrode and platinum foil as counter electrode. The frequency was swept from 50 mHz to 50 kHz.

While, the un-stimulated electrodes phase spectrum differs significantly from its *in vitro* spectra with an obvious depression of the phase transition point at frequencies > 1 KHz (figure 6.4). Also, an increase in the phase across the spectrum is observed, suggesting an increase in the resistive nature of the interface. For example, the phase difference at 10 kHz may be as high as 20 degrees. Thus the nature of the charge transfer behavior in the oxide film was varying *in vivo* for stimulated group (figure 6.7) while for un-stimulated group (figure 6.6) the increase in phase shows an increase in the resistive nature of the redox reactions. The low frequency region is associated with the intrinsic impedance of iridium oxide layers (Weiland and Anderson 2000).

Therefore, we sought to identify a suitable electric circuit equivalent model that explains these pronounced differences throughout the frequency range.

In vivo EIS dynamics of CV stimulated group EIROF electrodes are similar to the results reported by (Weiland and Anderson 2000). They were reporting the changes in impedance of chronically implanted AIROF electrodes due to application of biphasic stimulation pulses (100 µs/ph, 250 pulses/s). EIS (DC bias = 300 mV) and CVs (100 – 1000 mV/s, -0.6-0.9 V) which were measured from stimulated as well as a non-stimulated SIROF microelectrode site. The changes in impedance as due to CV stimulation were seen with their current pulse stimulated electrodes *in vivo*. However, the influence of CVs on this pattern was not discussed, though a change in impedance was mentioned post CVs. Probably, the slower cycling (25 cycles at 50 mV/s) effects the iridium oxide more compared to the faster CV cycles (larger than 100 mV/s) used in their study.

6.3.3 High Frequency Model (1-50 kHz)

As the conductive coating was EIROF across all the electrodes tested here, we began with the hypothesis that a single model would be able to explain the differences in the spectra. The traditional model most commonly used to fit *in vitro* spectra for iridium oxide or platinum electrode data consists of an electrolyte resistance in series with the parallel combination of the Constant Phase Element (CPE) or a capacitor and a Faradaic resistor. During the initial fits to the measured EIS spectra, the traditional model did not fit our EIS spectra and a single model was not sufficient to explain all the measured EIROF electrodes. Thus, an approach of breaking down the impedance to high and low frequency section and fitting these individual sections to a model was adopted (Weiland

and Anderson 2000). It turned out that the traditional model was able to fit only *in vitro* high frequency impedance (1-50 kHz) dataset of un-stimulated (group A) electrodes from our experiments. As reported in literature (Weiland and Anderson 2000) this model depicts the characteristic of a charge transfer in the high frequency region for AIROFs. So we sought a comprehensive model that would accommodate both our *in vitro* and *in vivo* data. In searching for an optimal model we took into account not only the chi-square values for goodness of fit of the whole frequency range, but also the errors for individual components (linear and non-linear elements) of the models.

The *in vitro* circuit model (figure 6.6) is composed of the solution resistance (R_s), the CPE and the charge transfer resistance (R_{ct}). CPE arises due to surface non-uniformity and roughness of the interface and accounts for the frequency dispersion of capacitance and thus its non-ideal behavior (Orazem and Tribollet 2008). The impedance of the CPE is given by $Z = (Q_o)^{-1} (i\omega)^{-n}$, where $(Q_o)^{-1}$ is a constant with dimension $Fcm^{-2} s^{(n-1)}$, ω is the angular frequency ($2\pi f$), $i = \sqrt{-1}$, and n is a scalar between 0 and 1. The phase angle of this non-ideal capacitive behavior is calculated as product of n and 90º. Thus, for an ideal capacitor n = 1 and for a resistor, n = 0. The CPE describes the deviation of the interfacial impedance from the ideal behavior (Orazem and Tribollet 2008).

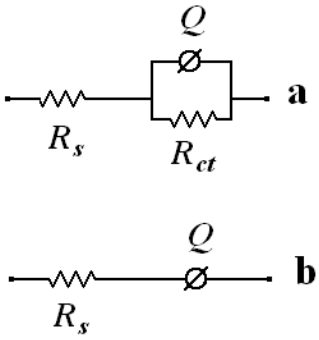

Figure 6.6: Equivalent circuit model used to fit high frequency impedance (1 kHz to 50 kHz) for the electrode-electrolyte interface (a) *in vitro* and (b) *in vivo*. Rs is the resistance of the solution (either electrolyte or tissue) and cabling, R_{ct} is representative of charge transfer reaction in the iridium oxide and Q is the constant phase element representing the non-linear double layer capacitive dispersion. The only difference between these two circuits is the value of R_{ct}. When *in vivo,* R_{ct} tends to infinity, and is thus represented by an open circuit in (b).

Figure 6.6 shows the model that appears to optimally fit the *in vivo* data: it is also the simplest model chosen. This circuit however did not fit the *in vitro* impedance. The two models are based on one idea (figure 6.6). When Rct$\rightarrow\infty$ it can be represented as an open circuit, and one would then obtain the *in vivo* circuit. This signifies an absence of an electron-limited transfer in the high frequency spectrum. The reduction of charge transfer is also observed with a decrease in redox CV peaks at 50 mV/s (figure 6.1). Table 6.2 summarizes the numeric results obtained with both models. The CPE-n exponent values for pre and post implantation are equivalent whereas the *in vivo* value is lower (0.70 ± 1.11% (pre), 0.31 ± 4.91% (*in vivo*), and 0.71 ± 0.86% (post)). The lowering of n value *in vivo* is indicative that the interfacial impedance is more resistive in nature in comparison to *in vitro*.

Table 6.3: Summary of the fitted parameter results with corresponding relative standard errors. The same model is used to gauge the goodness of fit in three scenarios: pre-implant, implanted, and post-implantation. These are the three rows. The columns summarize the results for each circuit element, along with the relative standard error, presented here, for clarity, in square brackets. The last column shows the chi-squared values for the three runs of the model, with values well below the required margin (0.001)

Un-stimulated Group	***Rs (Ω) [% error]***	***Q_o (F) [% error]***	***n [% error]***	***Rct (Ω) [% error]***	***$\chi 2$***
Pre (*In vitro*)	7.19E+01 [1.23 %]	4.35E-06 [8.12 %]	7.06E-01 [1.11%]	1.19E+03 [6.06 %]	1.40E-04
In vivo	5.30E+02 [4.15 %]	8.44E-05 [11.76 %]	3.14E-01 [4.91 %]	- -	3.27E-04
Post (*In vitro*)	6.28E+01 [1.22 %]	3.67E-06 [6.41 %]	7.18E-01 [0.87 %]	1.54E+03 [5.35 %]	1.36E-04

However, the CPE-Q_o value increased *in vivo* in comparison to pre and post implantation values (4.35 µF ± 8 % (pre), 84.40 µF ± 12% (*in vivo*), and 3.67µF ± 6 % (post)). All the values are reported in the form of value ± relative standard error (%). The solution resistance (R_s) is expected to be greater *in vivo* than pre and post implantation values as it represents the surrounding tissue. The estimated model parameters depict this trend. As table 1 shows, *in vitro* R_s = 71.9 Ω at 1.23 % (pre) and 62.8 Ω at 1.22 % (post), while *in vivo* R_s= 530 Ω at 4.15 %. This is a five-fold increase. The errors between the experimental values and the model results for each component are given in percentage, immediately after the resistance value. The parameter estimate errors, all below 15%, indicate that these values are indeed reliable.

6.3.4 Wider Spectrum Model (0.01 Hz to 50 kHz)

After developing the high frequency model, the saga of fitting the complete spectrum of impedance began. The simplest chosen model was the Randles which fit only the stimulated group, while it's fit towards un-stimulated group was visually poor as well plagued with high standard errors in parameters (> 100 %). The initial models developed in 1998 (Aurian-Blajeni et al. 1989) (figure 6.6) for hydrous iridium oxide fit un-stimulated electrodes reasonably well. The difference between the Randles and Aurian-Blajeni et al. model is the presence of a parallel RC component in series with the diffusion impedance.

Un-stimulated group *in vitro* model (figure 6.7) consists of a R_e (electrolyte resistance) the resistance of the electrolyte between the reference and the working (EIROF) electrode as well as series cabling and electrode wire resistance. Q_{dl} and n represent the double layer capacitance with a constant phase element. Physically it refers to the double layer formed by inserting the electrode into a liquid: the space between the solid and the liquid gives rise to interesting phenomena, which in turn mediate several mechanisms of charge transfer and impact the electrical performance of the electrode. R_{ct} (Charge transfer resistance) represents the resistance towards the transfer of charge due to any redox reactions occurring at the interface. The Warburg (W) impedance is technically a CPE where n=0.5 and is an oversimplified description of diffusion of the electrons or counter ions required for the charge transfer reaction (Weiland and Anderson 2000). Both C_m and R_m represent the intrinsic capacitance and resistance of the iridium oxide layer. The intrinsic resistance of the iridium oxide layer is "associated to the hopping

mechanism in disordered material" (Fritzsche 1972) . The *in vitro* model (figure 6.7) fits the high and low frequency spectrum well (figure 6.8).

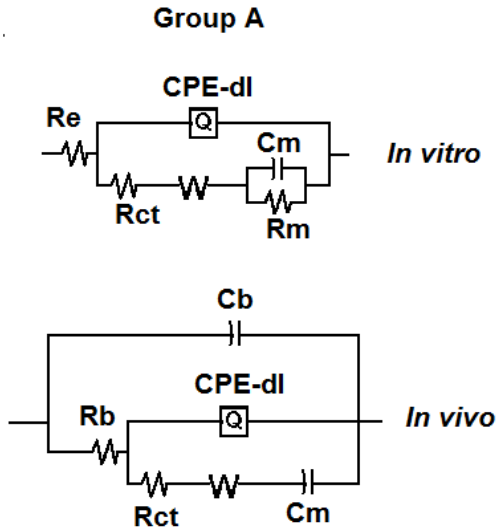

Figure 6.7: Equivalent circuit model used to fit wider frequency (200 mHz to 50 kHz) impedance for the un-stimulated EIROF microwires electrode-electrolyte interface *in vitro* and *in vivo*. R_e is the resistance of the solution and cabling, R_{ct} is representative of charge transfer reaction in the iridium oxide and CPE_{dl} is the constant phase element representing the non-linear double layer capacitive dispersion. The difference between these two circuits is the absence of Rct and replacement of R_e with a C_b and R_b. When *in vivo*, R_m tends to infinity, and is thus represented by an open circuit in (b). While C_b and R_b account for the placement of the reference and counter electrode on top exposed rat skull.

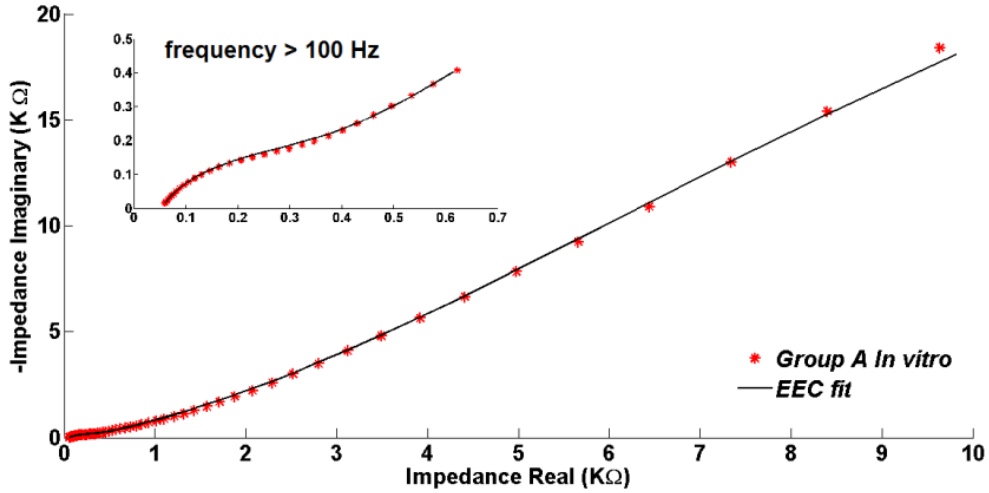

Figure 6.8: Complex impedance (Nyquist plots) of a (n=1) un-stimulated (groupA) EIROF microwire *in vitro* impedance. The solid line indicates the calculated data from the model as proposed in this paper, while the symbols represent the calculated impedance with the frequency as a parameter, varying from 20 mHz to 50 kHz. The inset is the high frequency impedance (> 100 Hz), showing the model fits well across the frequency spectrum.

An extra capacitance (C_b) introduced in the *in vivo* model accounts for the placement of the reference (AgCl) and counter electrode (Pt strip) (figure 6.7). In PBS (*in vitro*) the reference, counter and working (EIROF microwires) electrodes are placed in the same electrochemical cell. Thus, the impedance of the electrolyte between the reference and working electrode can be modeled as a simple resistor. *In vivo* the reference and counter electrodes are placed on top of the exposed rat skull with saline, while the working electrode (EIROF) was implanted in the rat hippocampi. Thus the bulk capacitance (C_b) and resistance (R_b) accounts for the impedance due to the saline, skull

and the brain tissue (figure 6.7). The presence of C_b and R_b improved the higher frequency (> 100 Hz) spectrum fits (figure 6.8) as compared to modeling the tissue as a simple resistor Re (figure 6.9), justifying its inclusion.

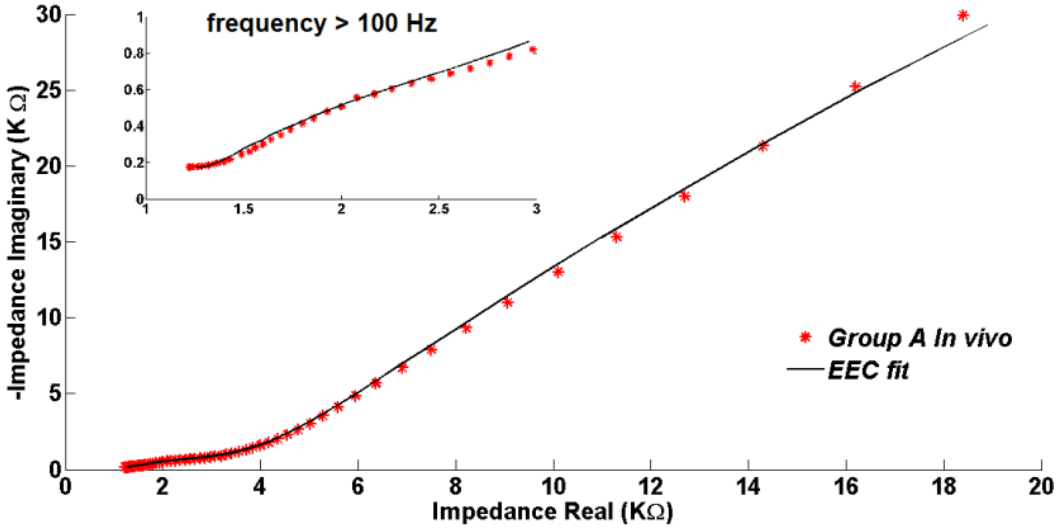

Figure 6.9: Complex impedance (Nyquist plots) of a EIROF microwire un-stimulated (groupA) measured *in vivo*. The solid line indicates the calculated data from the model as proposed in this paper, while the symbols represent the calculated impedance with the frequency as a parameter, varying from 20 mHz to 50 kHz. The inset is the high frequency impedance (> 100 Hz), showing the model fits well across the frequency spectrum. The high frequency spectrum (inset) shows a slight curvature (smaller time constant) and this is being accounted for bulk capacitance and resistance.

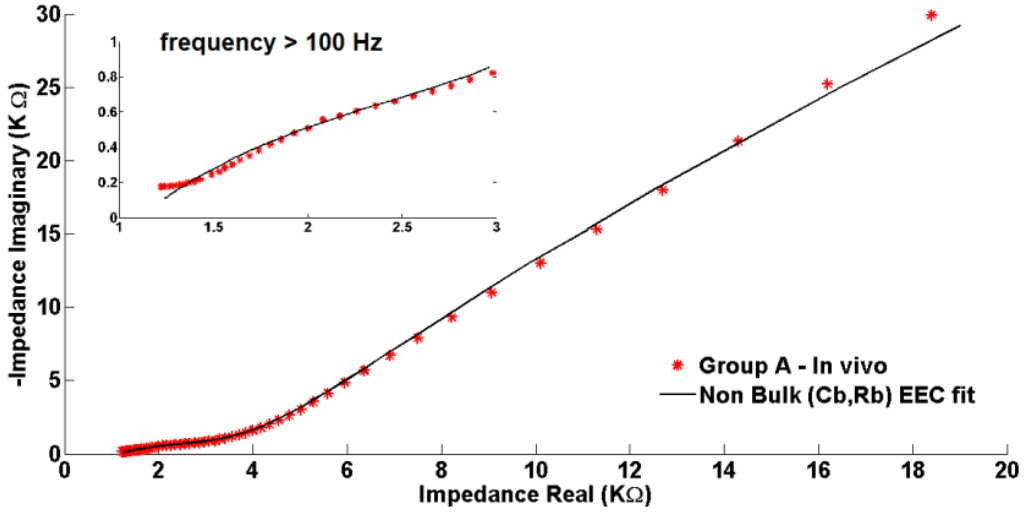

Figure 6.10: Complex impedance (Nyquist plots) of a un-stimulated (group A) EIROF microwire measured *in vivo*. The solid line indicates the calculated data from the model without the non-bulk components (R_b and C_b) as proposed in this paper, while the symbols represent the calculated impedance with the frequency as a parameter, varying from 50 mHz to 50 kHz. The inset is the high frequency impedance (> 100 Hz), showing the non-bulk model fits doesn't fit the slight curvature (smaller time constant).

The intrinsic resistance (Rm) is absent for *in vivo* un-stimulated model (figure 6.7). Inclusion of Rm resulted in $\chi 2 > 0.01$ as well errors for individual components (linear and non-linear elements) of the models > 100 %. The *in vivo* model for SIROF electrodes previously suggested in Weiland and Anderson (2001), also did not include R_m. However, there was no mention an *in vitro* EEC model for comparison.

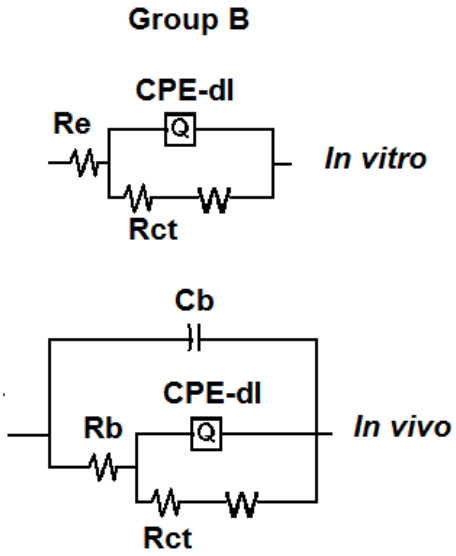

Figure 6.11: Equivalent circuit model used to fit wider frequency (50 mHz to 50 kHz) impedance for the stimulated (groupB) EIROF microwires electrode-electrolyte interface *in vitro* and *in vivo*. The *in vitro* model is essentially the Randles circuit with R_e the resistance of the solution electrolyte and cabling, R_{ct} is representative of charge transfer reaction in the iridium oxide and CPE_{dl} is the constant phase element representing the non-linear double layer capacitive dispersion. The difference between the two circuit is replacement of R_e with a C_b and R_b to account for the placement of the reference and counter electrode on top exposed rat skull.

Randles model fit the both the *in vitro* and *in vivo* impedance data for stimulated electrodes. Similar to the un-stimulated *in vivo* model C_b and R_b were included instead of R_e to account for the placement of the reference and counter electrodes (figure 6.11) for the fits (figure 6.12). Table 6.3 summarizes the numeric results obtained with *in vitro* and *in vivo* models for both groups. The results are summarized in a single table so that the parameter values can be compared against within as well as across groups. The deviation

between the experimental and modeled parameter values is greater for stimulated group with larger $\chi 2$ (~ 1E-3) compared to (1E-4) un-stimulated group fits.

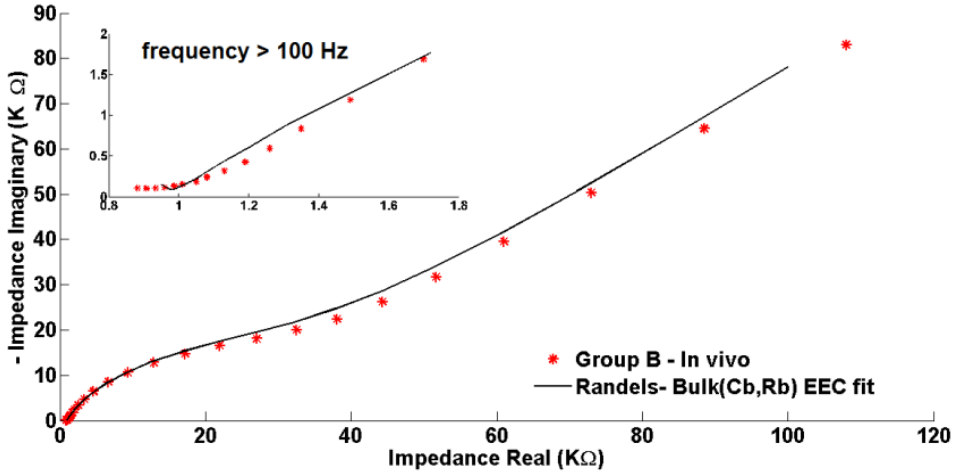

Figure 6.12: Complex impedance (Nyquist plots) of a stimulated (groupB) EIROF microwire measured *in vivo*. The solid line indicates the calculated data from the model with bulk components (R_b and C_b) as proposed in this paper, while the symbols represent the calculated impedance with the frequency as a parameter, varying from 200 mHz to 50 kHz. The inset is the high frequency impedance (> 100 Hz), fits shows the model fit is lower at high frequencies.

Table 6.4: Summary of the fitted parameter results with corresponding standard error means. The columns summarize the results for each circuit element, along with the standard error means of estimated parameters across electrode within a group.

	Un-stimulated In vitro (n=6) (mean ± s.e.m)	***Un-stimulated In vivo (n=4) (mean ± s.e.m)***	***Stimulated In vitro (n=4) (mean ± s.e.m)***	***Stimulated In vivo (n=4) (mean ± s.e.m)***
Eoc (mV)	326.00 ± 112.00	97.00 ± 29.80	-73.85 ± 0.85	-103.00 ± 13.01
C_b (pF)	-	99.90 ± 22.00	-	570 ± 54.30
R_e or R_b (Ω)	61.70 ± 6.57	786.00 ± 170.00	136 .00 ± 6. 39	801.00 ± 68.20
Q_{dl} (µF)	1.80 ± 0.26	30. 80 ± 15.60	3.51 ± 0.45	2.74 ± 0.10
Q-n	0.83 ± 0.04	0.06 ± 0.08	0.75 ± 0.02	0. 78 ± 0.005
R_{ct} (kΩ)	2.53 ± 1.80	4.98 ± 2.64	13.9 ± 3.64	73.70 ± 27.70
W ($k\Omega.s^{1/2}$)	21.10 ± 0.004	18.10 ± 9.04	12.20 ± 5.80	66.50 ± 7.75
C_m (µF)	107 ± 53.3	33 .00 ± 17.80	-	-
R_m (kΩ)	36.40 ± 13.34	-	-	-

The changes in the *in vitro* parameters with respect to *in vivo* parameters are broken down with brief explanations as follows:

- The higher value for R_b compared to R_e is due to the added resistance of tissue and exposed skull between the reference and the implanted EIROF microwire.
- The *in vivo* double layer capacity (Q_{dl}) increased for un-stimulated group while it slightly decreased for stimulated group. The increase in *in vivo* double layer capacitance for un-stimulated group is intriguing as the proton availability is lower in *in vivo* (Cogan et al. 2007). The decrease in the Q-n for un-stimulated group would suggest increase in resistivity of the interface, while it was comparable for stimulated group. This can also be corroborated by an increase in phase for un-stimulated group across the spectrum.

The double layer capacitance for AIROF electrodes has been shown to depend on the concentration of protons in the solution and is not sensitive to the electrode potential or the thickness of iridium oxide layer (Aurian-Blajeni et al. 1989). This trend was observed for the *in vitro* double layer capacitance showing only 14% relative standard error of mean across the samples.

- R_{ct} increases by 2 times for un-stimulated group while the increase is 5 times for stimulated group. Also, E_{oc} decreased for all electrodes when measured in the rodent hippocampi compared to PBS. The charge transfer resistance is dependent on applied potential (Cogan 2009). Though no DC bias was applied the electrodes had non-zero E_{oc} *in vitro* and *in vivo.* The estimated R_{ct} was lower for electrodes with larger E_{oc}. For an E_{oc} (*in vitro* un-stimulated) value of 754. 8 mV and 34.09 mV the corresponding R_{ct} was about 10 Ω and 10.5 kΩ. This trend was observed *in vivo* too, wherein for an E_{oc} of 162. 2 mV and 1.05 mV the R_{ct} was about 3.23 kΩ and 14.4 kΩ. It has been established that positive biases increases the conductivity of EIROFs (Weiland and Anderson 2000). Un-stimulated group presented greater and positive E_{oc} values compared to stimulated group. Thus, this could account for higher *in vitro* Rct of stimulated compared to un-stimulated group. Additionally, larger electrolyte resistance for group B could also influence the charge transfer resistance.
- Warburg impedance decreases slightly for un-stimulated group while it increases for stimulated group. (Aurian-Blajeni et al. 1989) and (Weiland and Anderson 2000) used a CPE instead of a Warburg element during fit, and suggested the CPE

reflected the “morphology seen by the protons in their movement through the narrow pores”. Instead of using a CPE the fits in this study used Warburg element (W), which is essentially fixing the CPEs constant (n) to 0.5 (infinite planar diffusion) (Orazem and Tribollet 2008). Thus the increase in Warburg impedance could suggest that the protons *in vivo* are interacting with EIROF morphology that has narrower pores for stimulated electrodes. A change in morphological structure of amorphous and crystalline SIROF due to stimulation has been reported (Thanawala et al. 2008). Weiland et al (2000) reported the decrease in CSCc due to current pulsing and this increases the Warburg impedance. Thus continuous CV cycling could be changing the morphology by narrowing the pores and decreasing the resistive currents due redox reactions as seen with pulsing.

- *In vivo* the intrinsic charge (C_m) of EIROFs for un-stimulated decreases while this parameter did not fit the stimulated group. It is probable that CV stimulation changes the intrinsic properties of EIROF films.
- *In vivo* the intrinsic resistance (R_m) of EIROFs is absent for un-stimulated group. This is inferred as R_m being high enough to be modeled as an open circuit.

6.4 Conclusions

Here we show that *in vitro* and *in vivo* models of EIROF electrodes are *dependent* on the application of stimulation prior to EIS measurement. This has been established previously for chronically implanted SIROF electrodes under pulsatile stimulation (Weiland and Anderson, 2000). However, the study involved tracking changes of *in vivo*

impedance due to stimulation while comparison with an *in vitro* was not shown. In this study the stimulation cycle consisted of 25 slow CV cycles (-0.7 V to 0.7 V at 50 mV/s) instead of pulses. The rationale behind this stimulation protocol was to test if a standard slow CV method which can be argued as low frequency stimulation would affect EIROFs performance. The behavior of CV stimulated EIROF impedance is similar to current pulses stimulated SIROF electrodes (Weiland and Anderson, 2000). The mid frequency impedance doesn't change but it's the low and high frequency impedance that increases. While the impedance increased for un-stimulated electrodes across the measured frequency spectrum.

Also, for un-stimulated EIROF electrodes the equivalent circuit model had to be modified as the microwire moves from *in vitro* to *in vivo* scenarios. This was first established by fitting the high frequency (1-50 kHz) spectrum with the simplest possible model of resistor (R_s) in series with a parallel capacitor (C_{dl}) and resistor (R_{ct}) (figure 6.6). For *in vivo* scenarios $R_{ct} \rightarrow \infty$ and had to be modeled as an open circuit. On the other hand wider spectrum (0.01 Hz – 50 kHz) model consisted of larger number of parameters (W,C_m,R_m) to fit the *in vitro* EIS spectra reasonably (figure 6.7). An increase in the R_{ct} is observed but the intrinsic resistance (R_m) of the EIROF film had to be modeled as an open circuit. It is interesting that the CV stimulated electrodes presented negative E_{oc} for both *in vitro* and *in vivo*. Also, the absence of EIROF intrinsic resistance (R_m) and capacitance (C_m) in the stimulated *in vitro* and *in vivo* model suggests that CV stimulation affects the oxides intrinsic properties. The *in vivo* R_{ct} values are larger than *in vitro* for both un-stimulated and stimulated electrodes. Thus, the relevance of *in vitro*

model as predictors of *in vivo* performance is not straightforward. The absence of factors such as influence of tissue on the material needs to be accounted. Additionally, we need to be aware if measuring methods are biasing our interpretation.

CHAPTER 7: Al_2O_3-PARYLENE C- RESULTS AND DISCUSSIONS

7.1 Overview

Accelerated lifetime testing (ALT) of Parylene C and Al_2O_3-Parylene C coated devices was conducted at 60 °C. Samples were tested up to 3 months while performing electrochemical measurements that indicate the integrity of the insulation. The electrochemical characterization included electrochemical impedance spectroscopy, DC leakage currents, and cyclic voltammetry. In addition, based on modeling of the data using electrical circuit equivalents, it is shown that there are two main modes of failure. Our results suggest that failure of the insulating layer is due to pore and blister formation or thinning/delamination of the coating over time**.**

7.2 Failure Criterion

To understand the failure criterion an example of a simple circuit model used to describe an intact insulation is discussed. The model is a parallel capacitor (C_L) and resistor (R_L) associated with layer capacitance and resistance (Fernández-Sánchez, McNeil, and Rawson 2005). The layer resistance is attributed to any inherent defects in the insulation layer. For an intact insulation the R_L is extremely high while the capacitive impedance ($1/j\omega C_L$, $j = (-1)^{½}$, $\omega = 2\pi f$) is the lower for the applied electric field. Thus the phase for an ideal intact coating would be - 90° across the frequency spectra. As the coating transits from an excellent coating to an intermediate it allows for larger current to

pass through due to increased electrolyte permeation. This decreases the coating resistance while increasing the coating capacitance. This translates to an increase in the low frequency phase while the mid and high frequency phase is still dominated by the coating capacitance (-90°) (Fernández-Sánchez, McNeil, and Rawson 2005). Thus, low frequency phase increase indicates the initial stages of degradation. The impedance modulus drops with increase in mid frequency phase as the electrolyte permeates deep enough to contact the underlying metal (Fernández-Sánchez, McNeil, and Rawson 2005). The model to explaining insulation degradation is discussed in detail in the equivalent circuit modeling section.

The failure criteria used in this study (table 7.1) was based on the literature (Corfias, Pebere, and Lacabanne 1999)(Akbarinezhad and Faridi 2008)(Xie et al. 2012) to allow classification of coating status based on leakage current and EIS observations under accelerated aging.

Table 7.5: Failure criteria to classify the insulation barrier properties

	Leakage current (pA)	***Impedance, modulus (Ω)***	***Impedance, phase (°)***
Excellent	< 50	$\geq 10^9$ at $f \leq 1$ Hz	$\geq 80°$ for all frequencies
Intermediate	< 1000	$< 10^9$ at $f \leq 1$ Hz	$< 80°$ in any frequency < 1Hz
Failure	≥ 1000	$< 10^8$ at $f \leq 1$ Hz	$< 80°$ for any frequency > 1 Hz

7.3 Electrical Equivalent Circuit modeling

The lateral impedance between the fingers of the IDEs was measured over the course of ALT. To quantify the changes in the electrical properties over the ALT period, the EIS data was fit to appropriate equivalent circuits. As the electrodes are coated with insulation the lateral impedance can be modeled as a perfect capacitor (Fernández-Sánchez, McNeil, and Rawson 2005). However, polymeric coatings are permeable to moisture (Hassler, Boretius, and Stieglitz 2011) and this can be seen as non-zero values for the real part of the impedance. Thus, it is modeled as a layer capacitance (C_L) and layer resistance (R_L) in parallel. The capacitance is usually replaced by a constant phase element (CPE) (Fernández-Sánchez, McNeil, and Rawson 2005), mathematically expressed as $Z = Q_o/ (j\omega)^{\alpha}$, Q_o is a constant, $j = (-1)^{½}$, $\omega = 2\pi f$, and α is a constant between 0 and 1. If $\alpha=1$, Q_o is the capacitance.

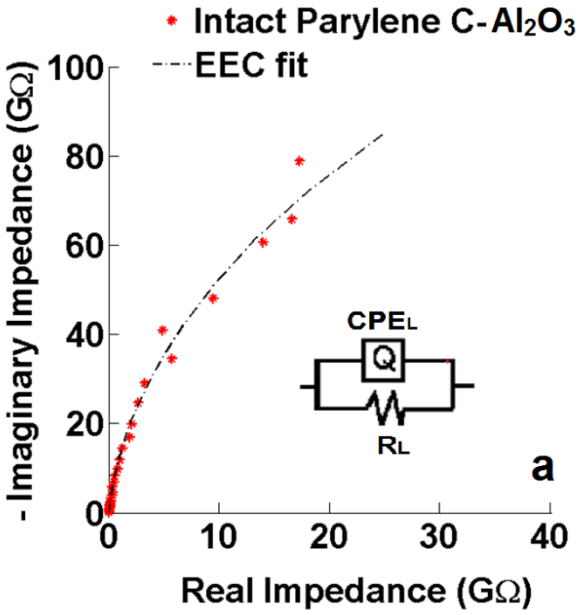

Figure 7.1: Complex impedance (Nyquist plots) plots for an intact coating with respective equivalent circuit model in inset. The solid line indicates the calculated data from the model as proposed in this paper, while the symbol (*) represent the calculated impedance with the frequency as a parameter, varying from 10 mHz to 10 kHz. CPE_L (capacitance of the insulation) in parallel with R_L (resistance of the insulation) is traditionally used to model intact insulation.

CPE is a frequency dependent capacitance and is usually associated with the distribution of time constants due to inhomogeneous surfaces (Orazem and Tribollet 2008). Thus, CPE accounts for any non-ideal dielectric characteristics of the insulation due to inhomogeneity of the surface (Cieślik et al. 2011). Thus we used a parallel combination of CPE_L and R_L to model the intact coatings (figure 7.1inset), an example of its fit to the measured data is shown in figure 7.1. When the insulation degrades, electrolyte penetrates through accessing the underlying metal. The commonly used

equivalent circuit to model this process consists of a polarization resistance (R_P) and double layer capacitance (C_{dl}) (figure 7.2 a) in addition to C_L and R_L.

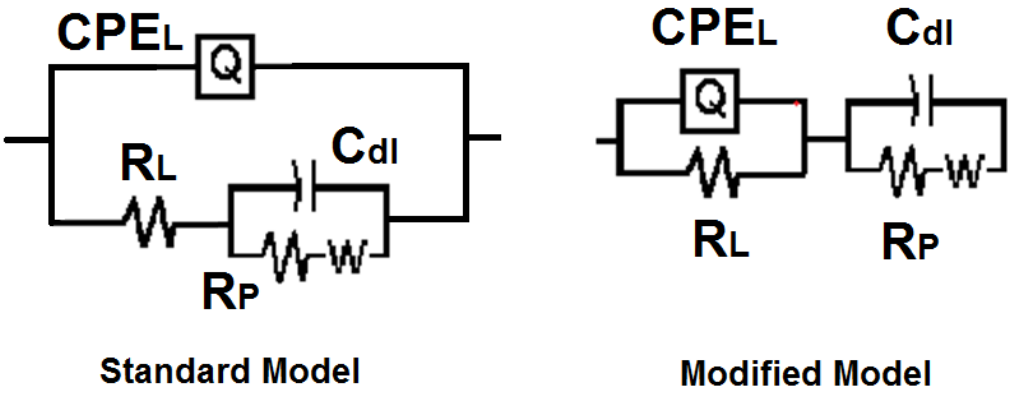

Figure 7.2: CPE_L (capacitance of the insulation) in parallel with R_L (resistance of the insulation), R_P (pore resistance), C_{dl} (double layer capacitance at the exposed metal interface) and W (Warburg impedance accounting for diffusion of ions across the interface).

R_P reflects the rate of corrosion of the underlying metal substrate and C_{dl} is the double layer capacitance between the exposed metal and the electrolyte (Hassler et al. 2010). R_P and C_{dl} cause the appearance of two semicircles in the Nyquist representation of the impedance spectra. The smaller semi-circle at high frequency is due to coating capacitance and resistance while the half-semicircle at low frequency is due to R_P and C_{dl} (figure 7.3).

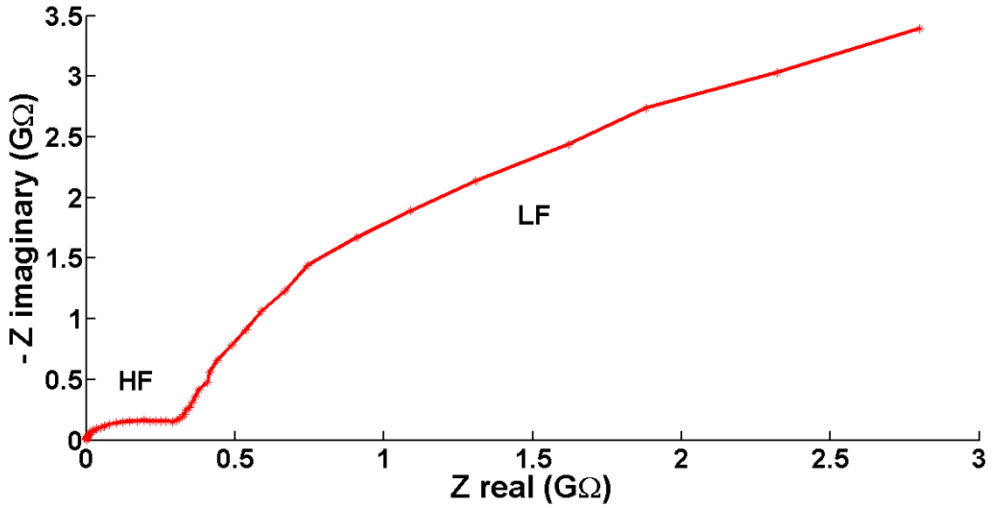

Figure 7.3: Complex impedance (Nyquist plot) plot of a failed coating. Two semi-circular regions manifest in the plot. The low frequency (LF) region represents the capacitive double layer due to the exposed metal and high frequency (HF) relates to the layer capacitance.

50 % of the failing Al_2O_3-Parylene C IDEs presented with such EIS spectra (figure 7.3) and these were initially fit using the standard model (figure 7.2). However, the fits not only presented with low chi-squared values (~ 10E-2) but didn't fit our failing EIS spectra presentations (figure 7.3). It is important that the fit all the impedance plots (Real versus Imaginary, Modulus and Phase versus Frequency, Real and Imaginary versus frequency, Real versus Imaginary Admittance as well as the complex capacitance plots). More importantly, it should be able to explain the electrochemical processes occurring at the interface. The standard models are traditionally used for an electrochemical setup that includes an external reference electrode such as an Ag|AgCl

having negligible impedance. Thus, the EIS spectra and its fit to the standard model reflect the electrochemical processes occurring at the coated working electrode.

However, as the insulating coating degrades, the lateral impedance between the IDE fingers would decrease as soon as underlying metal (Au) on either one of the IDE finger is exposed. Since the reference electrode is a coated IDE finger with high impedance, it needs to be accounted for in the equivalent circuit of a failed coating. The modified equivalent circuit model fit our failing EIS data (figure 7.2) and accounts for pore formation that allows access of the electrolyte to the underlying metal. The accessible metal is thus modeled as a double layer capacitance (C_{dl}) in parallel with Warburg diffusion impedance (W) and polarization resistance (R_P) of the metal. The Warburg impedance accounts for electrochemical process occurring under the insulation (Fernández-Sánchez, McNeil, and Rawson 2005).

The modified model fit our failing electrodes with decent Chi-squared values (~ 1E-3), all the impedance plots as well as with improved residual plots. Figure 7.4 shows the fit comparison between the standard versus modified model to a failing Al_2O_3-Parylene C IDE sample. The modified model fits the low frequency spectrum better. The modified model provides for the physio-chemical explanation but also provides a satisfactory visual fit while the standard model fails to fit the model in the low and mid frequency range. The Warburg impedance used in the model usually reflects the electrochemical reactions occurring under the insulation.

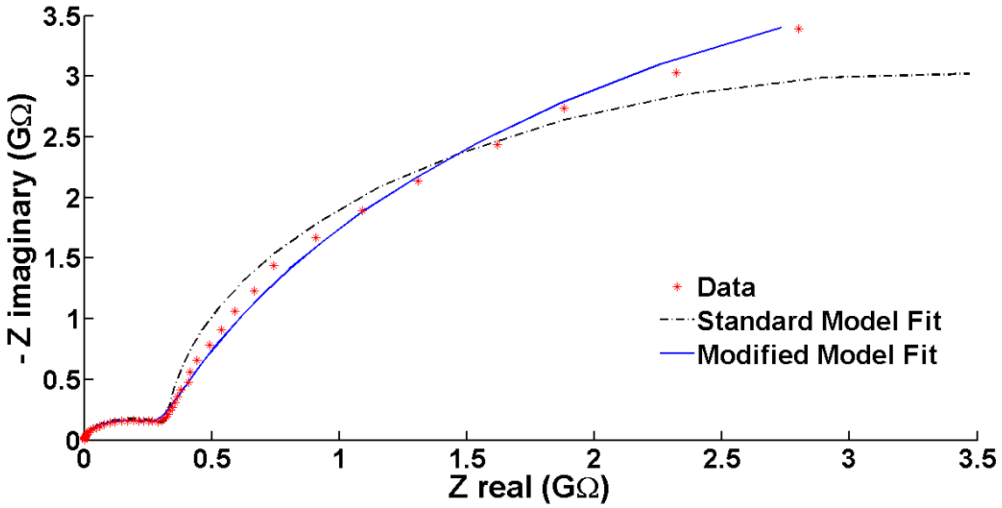

Figure 7.4: Complex impedance (Nyquist plots) plots for a failed coating with respective fits using the standard (dashed line) and modified (solid line) equivalent circuit models. The symbol (*) represent the calculated impedance with the frequency as a parameter, varying from 10 mHz to 10 kHz. The modified model fits the low frequency spectrum better than the standard model**.**

7.4 Room Temperature Inspection

The average leakage current during dry test (in air) for Al_2O_3-Parylene C samples was 2.1 ± 1.2 pA (mean ± s.e.m, n=8) while for Parylene C 0.29 ± 0.08 pA (mean ± s.e.m, n=6). This translates to a DC resistance greater than 100 GΩ ($5V/I_{DC}$) in air. EIS was measured for all samples in air before immersion in phosphate buffered saline (PBS). The EIS spectrum is a straight line in the Nyquist plot and owing to extremely high resistances the error in estimation for layer resistance was in the range of 20-50 %. The estimated average Q_L for all the IDEs was 62 ± 0.9 pF (mean ± s.e.m, n=14).

After dry testing the samples were immersed in PBS at room temperature. A bending of the impedance curve in the Nyquist plots was observed when the samples were immersed in PBS at room temperature, suggesting electrolyte penetration through small defects in the insulation. This also manifests as a horizontal line in the low frequency range in the Bode impedance representation (Fernández-Sánchez, McNeil, and Rawson 2005).

20 % (2 out of 10) Al_2O_3-Parylene C and 40 % (4 out of 10) Parylene-C samples failed during room temperature PBS inspection. ALT was performed on these samples but was not included in the life time assessment or fit results. The intact insulation model (figure 7.2) was used to fit the surviving room temperature samples impedance data. The average Q_L in PBS compared to air increased by ten-fold for Parylene C and Al_2O_3-Parylene C IDEs (table 7.2). This is due to the penetrating electrolyte having a higher dielectric constant (ε_r=80) (Uematsu and Frank) than the Parylene C coating (ε_r=3.15) (Xie et al. 2012). As expected, the average R_L of Al_2O_3-Parylene C was 5 times greater than that of Parylene C (table 7.2).

Table 7.6: EIS equivalent circuit model parameters of Parylene C and Al_2O_3-Parylene C coated IDE samples at room temperature in PBS

Room temperature PBS	***Q_L (pF) (mean ± s.e.m)***	***Q_n (mean ± s.e.m)***	***R_L (GΩ) (mean ± s.e.m)***
Parylene C (n=6)	151 ± 12.8	0.96 ± 0.0004	5.9 ± 2.4
Al_2O_3-ParyleneC (n=8)	156 ± 17.7	0.97 ± 0.0006	25.9 ± 3.2

7.5 Age Acceleration at 60 °C

After room temperature inspection the samples were age accelerated at 60 °C in PBS. Representative plots from two IDEs illustrate the stability of an intact coating (figure 7.6) and the transition in impedance and phase exhibited by a failed coating (figure 7.5).

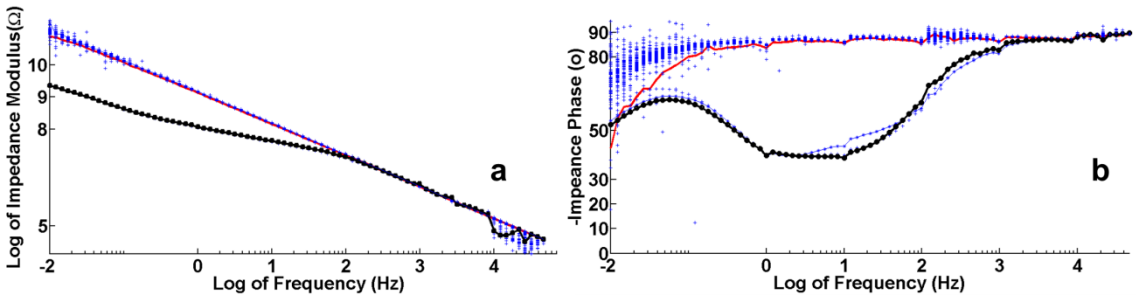

Figure 7.5: Overlay of impedance (a) modulus (b) phase of Al_2O_3 -Parylene C (5 nm/6 µm) sample under age acceleration at 60 °C. At day 1 (solid red line) the sample presents with high impedance and phase ~ – 80° (capacitive characteristics) for frequencies greater than 1 mHz. By day 29 (black ●) decrease in impedance modulus is accompanied by increase in phase above -40° (conductive characteristics), indicating access of electrolyte to the underlying metal due to barrier failure.

Specifically, the EIS spectra of the failing insulation shows a decrease in the impedance modulus (figure 7.5a) and transition of phase > -80° (figure 7.5b), which is consistent with the emergence of a conductive pathway through the insulation. If the 10 Hz phase angle increases above -40° it usually means electrolyte permeation through the

insulation enough to cause electrochemical reactions on the underlying metal (Corfias, Pebere, and Lacabanne 1999; Akbarinezhad and Faridi 2008).

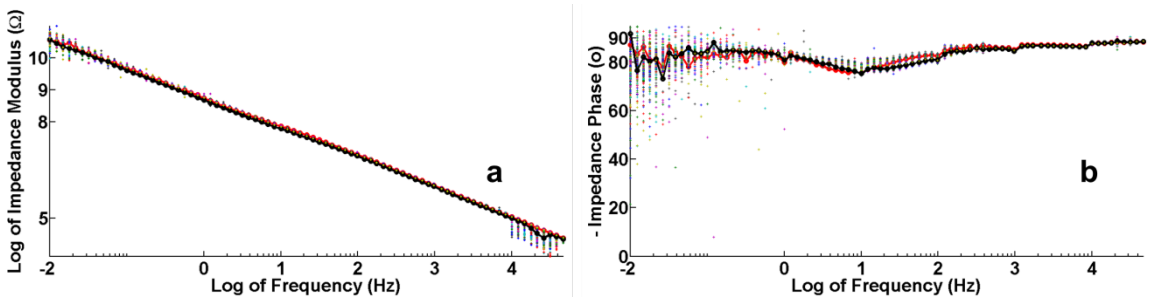

Figure 7.6: Overlay of impedance (a) modulus (b) phase of a stable Al_2O_3 -Parylene C (5 nm/6 µm) coated sample from day 1(solid red line) to over 1700 hours (~70 days) (black●) of age acceleration at 60 °C in PBS. The unchanging impedance spectrum and phase below – 80 ° (capacitive characteristics) indicates the coatings maintaining its barrier properties throughout the experiment.

Of the 14 total IDEs age accelerated, four IDEs from each group failed within the 3 month study period. The failed insulation model (figure 7.2) fit 75% of both Parylene C and Al_2O_3-Parylene C suggesting a similar failure mechanism. However, 75% of Parylene C samples failed within the first 24 hours of age acceleration at 60°C, while Al_2O_3-Parylene C failed after longer immersion time (> 100 hours).

7.5.1 Parylene C

The increase in Q_L for Parylene C and low R_L estimates below 3 G**Ω** (table 7.3) would suggest increased electrolyte penetration. The manifestation of R_P indicated access

to underlying metal (Fernández-Sánchez, McNeil, and Rawson 2005). The estimated α value of failed Parylene C (0.96) was nearly identical to the room temperature estimates (0.95) suggesting the similar surface morphology. The Parylene C sample that failed by day 3 (57 hours) of ALT had its day 1 EIS spectra fit the failing equivalent circuit model with R_L greater than 6 GΩ. This sample was not deemed as failure as the DC leakage current was less than 1000 pA. By day 3, R_L had reduced to 3 GΩ and I_{DC} over 1 nA.

Table 7.7: EIS equivalent circuit model parameters of Parylene C coated IDE samples at 60 °C in PBS

Fit Parameters	**PBS-Room Temp Surviving n=6 (mean ± s.e.m)**	**PBS 60 C @ Day Fail n=4 (mean ± s.e.m)**
Q_L (pF)	151 ± 13	312 ± 85
α	0.96 ± 0.004	0.95 ± 0.01
R_L (GΩ)	5.94 ± 2.4	2.40 ± 0.52
*** C_{dl} (pF)**	-	249 ± 52
*** R_P (GΩ)**	-	0.142 ± 0.031
*** W (GΩ. $S^{1/2}$)**	-	0.580 ± .0035

*applicable to only n=3 failed electrodes

The EIS spectra of the Parylene C sample that failed after the longest immersion time (> 1500 hours) fit the intact insulation model with an increase in Q_L and decrease in R_L. Increase in Q_L and decrease in R_L suggests either blistering (Taylor 1989) thinning (Sabot and Krause 2002) or delamination (Fernández-Sánchez, McNeil, and Rawson 2005).

The surviving Parylene C samples (n=2) presented with extremely high R_L (> 100 GΩ) (table 7.4) and low I_{DC} (~ 100 pA) at the end of 3 month testing period. Usually, the increase in R_L over time would suggest rusting of the underlying metal. However, this behavior was not observed in the failed samples. The failed samples were not removed from the ALT setup and data was collected for 3 months. A decrease in impedance is seen over time for these samples ruling out rusting of the underlying gold electrodes.

Table 7.8: EIS equivalent circuit model parameters of Parylene C coated IDE samples at day 1 and day 90 at 60 °C in PBS at

ALT @ 60 °C PBS	***Q_L (nF) (mean ± s.e.m)***	***Q_n (mean ± s.e.m)***	***R_L (GΩ) (mean ± s.e.m)***
Parylene C (n=3)-Day1	180 ± 21	0.96 ± 0.001	40 ± 23
ParyleneC (n=2)-Day 90	155 ± 13	0.95 ± 0.01	183 ± 0.7

7.5.2 Al_2O_3-Parylene C

The failing Al_2O_3-Parylene C samples also presented with lower R_L~ 4 G**Ω** (table 7.5). The R_P manifestation is clearly distinguishable in 50% of these samples as two semi-circles in the Nyquist plots. Both of these samples failed at time > 650 hours of age acceleration. The Al_2O_3-Parylene C sample that failed after the longest immersion time (1529 hours) showed best fit without a Warburg diffusion. The large increase in Q_L and decrease in α for all failed Al_2O_3-Parylene C samples would suggest blistetring, thinning

or microscopic delamination of Parylene C. While, the presence of C_{dl} and R_P would suggest that the Al_2O_3 layer was exposed and its dissolution (Abdulagatov et al. 2011) lead to access of the underlying Au electrodes. The decrease in α for all failed Al_2O_3-Parylene C sample indicate changes in surface morphology of the coating (Sabot and Krause 2002)(table 7.5).

Table 7.9: EIS equivalent circuit model parameters of Al_2O_3-Parylene C coated IDE at 60 °C in PBS

Fit Parameters	**PBS-Room Temp Surviving n=8 (mean ± s.e.m)**	**PBS 60 C @ Day Fail n=4 (mean ± s.e.m)**
Q_L (pF)	156 ± 18	4090 ± 1920
α	0.97 ± 0.006	0.92 ± 0.03
R_L (GΩ)	25.9 ± 3.2	3.95 ± 0.43
C_{dl} (nF)	-	1.32 ± 1.03
R_p (GΩ)	-	0.30 ± 0.22
*** W (GΩ. $S^{1/2}$)**	-	0.38 ± 0.06

*applicable to only n=3 failed electrodes

For the surviving Al_2O_3-Parylene C samples R_L at day 1 of ALT (109 ± 30 GΩ, n=8) was four times larger compared to room temperature (PBS) (25.9 ± 3.2 GΩ, n=8). Interestingly, the four samples Al_2O_3-Parylene C that failed started with high R_L (143 ± 45 GΩ, n=4) compared to the four samples that survived ALT (40 ± 9 GΩ, n=4).

75 % of surviving samples at the end of 3 months had lower R_L (16.2 ± 5.2 GΩ) compared to day 1 (39.7 ± 9.4 GΩ) of ALT, while Q_L increased to 187 ± 26 pF from 176

± 2.1 pF (day1). The reduction in layer resistance and increase in layer capacitance suggests slow degradation in the Al_2O_3-Parylene C over time as they are age accelerated at 60 °C. While one surviving Al_2O_3-Parylene C sample R_L increased from 181 GΩ (day 1) to 581 GΩ with a slight increase in the layer capacitance from 265 pF (day1) to 278 pF. Interestingly, this sample had begun as an intermediate insulation and by day 4 of its age acceleration had transitioned to an excellent insulation. The average parameter values of the fits of surviving samples are presented in table 7.6.

Table 7.10: EIS equivalent circuit model parameters of Al_2O_3-Parylene C coated IDE samples at day 1 and day 90 at 60 °C in PBS at

ALT @ 60 °C PBS	*Q_L (pF) (mean ± s.e.m)*	*Q_n (mean ± S.E.M)*	*R_L (GΩ) (mean ± S.E.M)*
Al_2O_3-Parylene C (n=8)-Day1	168 ± 17	0.96 ± 0.005	109 ± 30
Al_2O_3-ParyleneC (n=3)-Day 90	187 ± 26	0.96 ± 0.007	16 ± 5

*4 samples of Al2O3 survived but one of these had expectionally high R_L and not reported here

7.6 DC leakage current

The DC leakage current tested in air for Parylene C and Al_2O_3-Parylene C IDEs were low with an average of 1.33 ± 1 pA (mean ± s.e.m, n=14). An increase in the average DC leakage current to 77.9 ± 37 pA (mean ± s.e.m, n=8) for Al_2O_3-Parylene C and 357 ± 41 pA (mean ± s.e.m, n=6) for Parylene C was seen after immersion in PBS at room temperature. This is expected as the initial electrolyte ingress into polymeric

coating creates conductive pathways that are absent in air (Fernández-Sánchez, McNeil, and Rawson 2005). All coatings on IDEs maintaining barrier properties presented with leakage currents ≤ 800 pA (figure 7.7) throughout the study period, while the failed coatings (n=8) leakage currents exceeded 1 nA (figure 7.8).

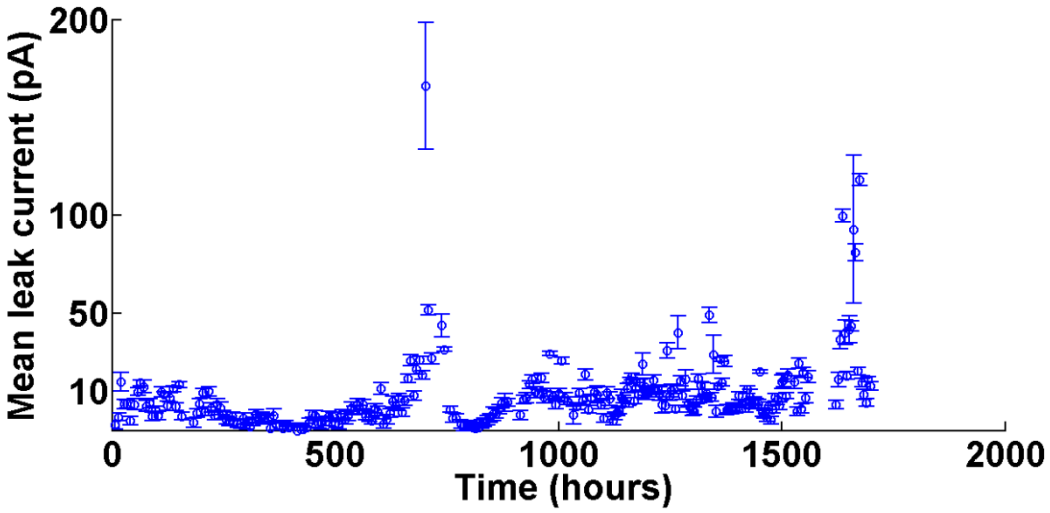

Figure 7.7: DC leakage current plotted against age accelerated (60 °C) time of a stable Al_2O_3 -Parylene C (5 nm/6 µm) coated sample. Each data point is an average of 600 seconds of acquired leakage currents at $5V_{DC}$ applied across the IDE sample. The sample presents with low DC leakage currents with occasional increase, well below the threshold to failure of 1000 pA.

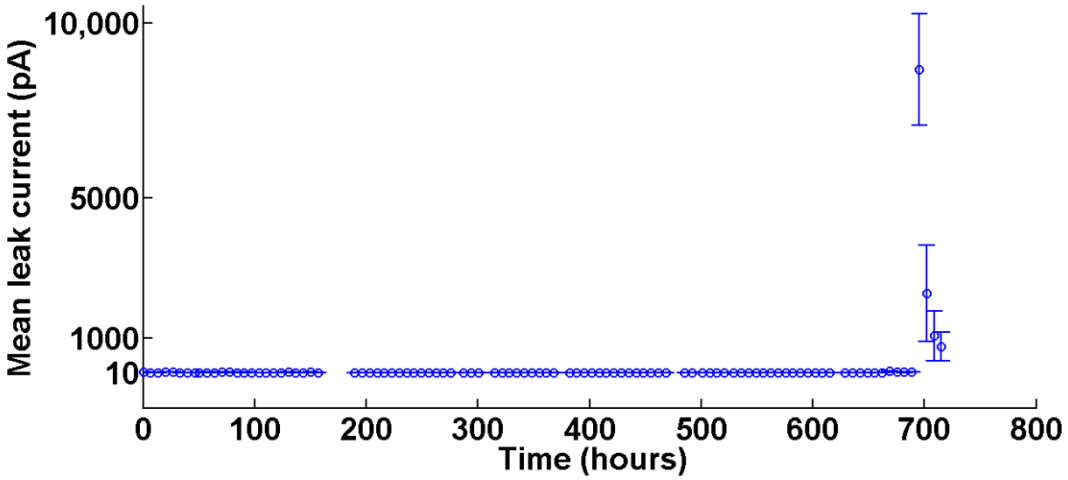

Figure 7.8: DC leakage current plotted against age accelerated (60 °C) time of a failing Al_2O_3 -Parylene C (5 nm/6 µm) coated sample. Each data point is an average of 600 seconds of acquired leakage currents at $5V_{DC}$ applied across the IDE sample. At 700 hours (~ 29 days) the DC leakage currents increases above 1000 pA, indicating failure in the barrier properties.

The 1 kHz impedance is a common metric used in the neural engineering realm to report the electrodes stability or quality. The rationale behind this is that the time duration of an action potential generated by a neuron is around 1 ms with low amplitude 10 mV (Quiroga and Panzeri 2009). Thus, the ability of a recording electrode to measure this low voltage signal is highly dependent on the impedance value at the frequency equivalent to 1/T being 1 kHz (Cogan 2008).

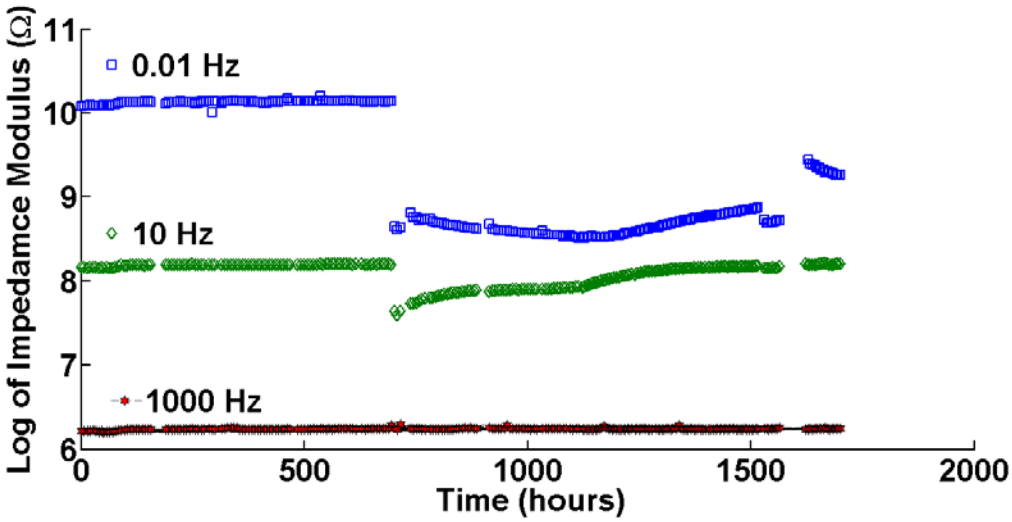

Figure 7.9: Impedance modulus of an age accelerated failing Al_2O_3 (5 nm)-Parylene C (6 µm), for three frequencies (0.01 (blue □), 10 (green◊) and 1000 (red*) Hz). The drop in impedance modulus of 0.01 and 10 Hz at 600 hours indicates failure of insulation. However, the impedance of modulus at 1 kHz is insensitive to the failure and maintains high its impedance magnitude for 1700 hours of age accelerated time.

Recently, 1 kHz modulus of impedance was used to evaluate the performance of liquid crystal insulating encapsulation for neural interfaces (Lee et al. 2011). Usually, when the insulation fails and the underlying metal is exposed the impedance of the capacitance is still lower than that of the layer resistance at high frequency (Zuo et al. 2008). Lowering of the 1 kHz impedance would occur when the insulation fails drastically. The insulation coating has to fail drastically such that its value is lower than the dominating capacitive impedance to reflect changes at higher frequencies (Zuo et al. 2008).

It is important to recognize that 6 out of 8 failing IDE samples (Al_2O_3-Parylene C (n=4) and Parylene C (n=2)) in this study showed no decrease in the impedance modulus at 1 kHz (figure 7.9). As seen in figure 7.9 the failing electrodes 1 kHz impedance modulus is stable even after its failure time point (700 hours) while the low and mid frequency impedance have lowered considerably. Thus, reliance on 1 kHz impedance modulus should not be solely used as a performance metric for material stability for neural electrodes.

The DC leakage currents of stable Al_2O_3-Parylene C samples were transitioning (figure 7.10) between intermediate and excellent insulation (table 7.1). The low frequency (0.01 Hz) phase was very sensitive to these transitions while the mid and high frequency spectrum were particularly insensitive (figure 7.10). The low frequency phase is directly related to the layer resistance (Fernández-Sánchez, McNeil, and Rawson 2005), thus the changes in DC leakage current are seen at the lower end of the frequency spectrum. As the glass transition temperature for Parylene C is between 55 – 95 °C (Kahouli et al. 2009), the polymer could be undergoing some transitions at 60 °C. Another, possibility would be exposure of surface contaminants in the polymer giving rise to this occasional increase in the DC leakage currents. These transitions were not investigated during this study.

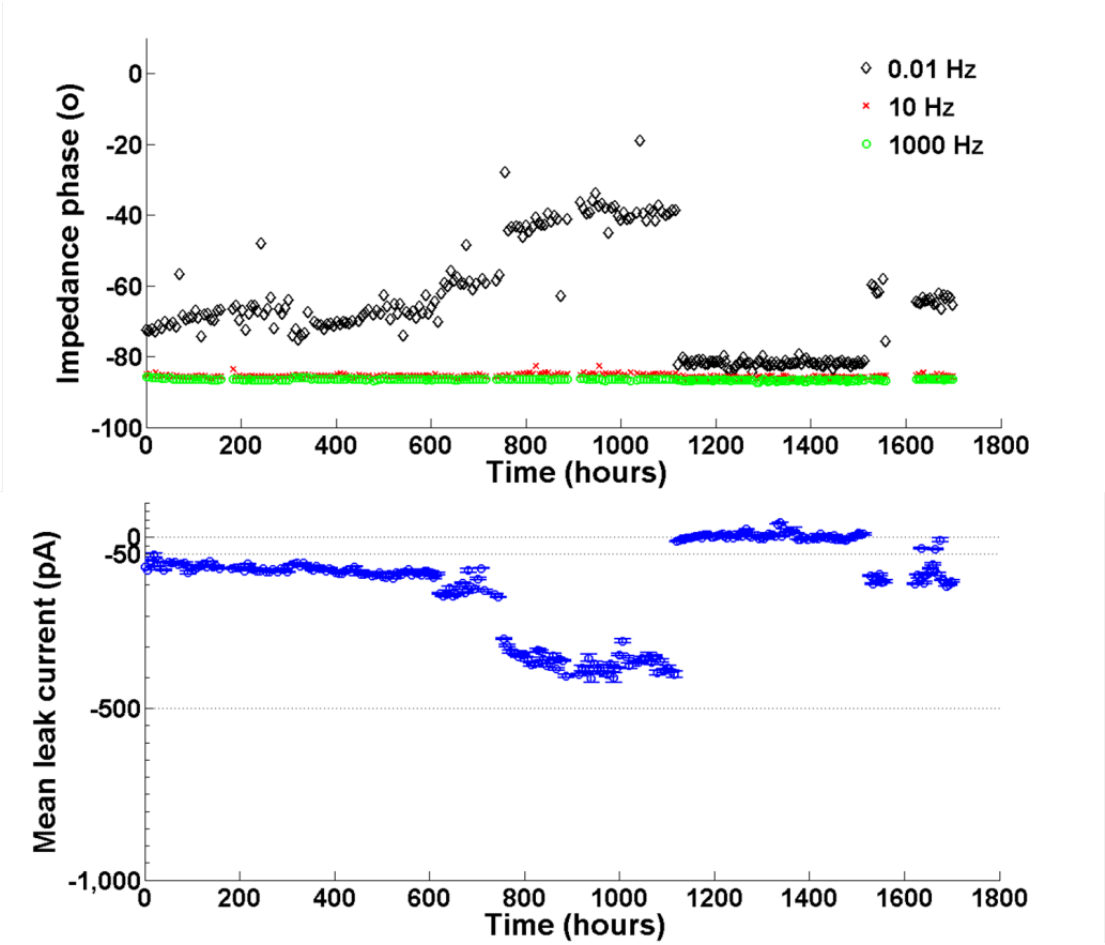

Figure 7.10: The low frequency (0.01 Hz) phase (◊)sensitive to transistions in DC leakage. While higher frequencies (> 10 Hz) are not sensitive to these transistions.

7.7 Mean Time to Failure

An exponential distribution for failure times (figure 7.11) was assumed to estimate the MTTF in each group. The 95% confidence interval for Parylene C was estimated at (465, 2683) (hours) and (1288, 20592) (hours) for Al_2O_3-Parylene C. MTTF of Parylene C and Al_2O_3-Parylene C are listed in table 7.7. The p-value for testing the

null hypothesis of equal MTTF between groups ($\mu_1 = \mu_2$) against one-sided alternative of $\mu_2 > \mu_2$ is 0.034, with effect size of 4.6 ($\mu_{2/}\mu_1$) thus demonstrating statistical significance.

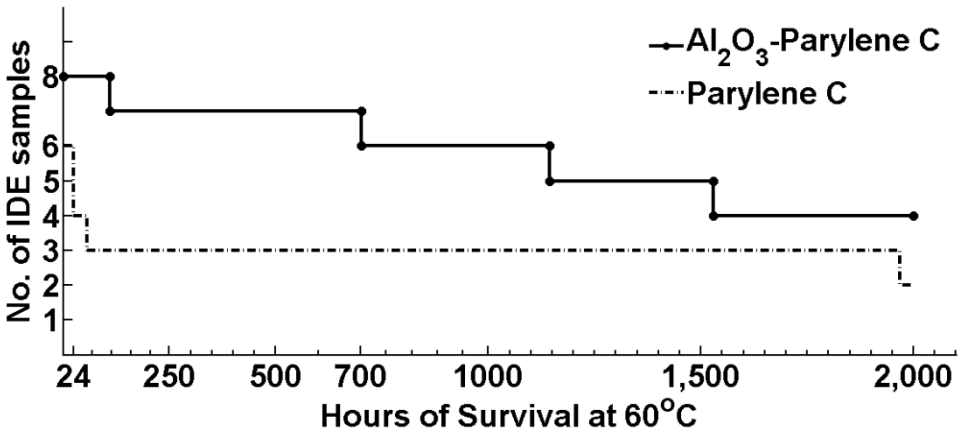

Figure 7.11: The time to failure of IDE samples used to calculate statistics reported for the lifetime comparison between Alumina- Parylene C (solid line) and Parylene C (dashed line) coated samples.

The observations suggest that the MTTF of Al_2O_3-Parylene C is approximately 4.6 times greater than Parylene C. In addition, for the same number of failure events to occur in both groups, assuming an exponential distribution of lifetimes, the required sample size is eight Parylene C and eighteen Al_2O_3-Parylene C IDEs. The MTTF at 37 °C for both samples was extrapolated assuming a Q_{10}=2. Thus, the range of 74.1-222.4 days at 60 °C is equivalent to 1-3 years at 37 °C.

Table 7.11: Mean Time to failure of Al_2O_3-Parylene C (5 nm/6 µm) and Parylene C (6 µm) at 60 °C

Sample	*MTTF (hrs) @ 60 °C Mean ±s.e.m*	*MTTF(days) @ 60 °C Mean ±s.e.m*	*~ MTTF@ 37°C lifetime (Q_{10}=2)*
Parylene C (n=6)	1117 ± 499	49.1 ± 20.7	< 1 year
Al_2O_3-Parylene C (n=8)	5150 ± 2683 *	214.6 ± 111.8	3 years

* The lifetime of Al_2O_3-Parylene C coating> Parylene C coating (p=0.03)

7.8 Conclusions

The data strongly suggests that the MTTF of Al_2O_3-Parylene C coating is significantly greater than Parylene C alone. The $MTTF_{37°C}$ for Parylene C (~ 8 months) reported here is comparable to values reported from other studies using similar coating thickness. Hara et al reported $MTTF_{37°C}$ as 6 months for Parylene C sheath microelectrode probe (Hara et al. 2012), while Li et al (2010) reported 2 days as $MTTF_{90°C}$ for Parylene C. (Hsu et al. 2009) show that Parylene C coated IDEs maintained barrier properties for more than one year at 37 °C. We have shown that the $MTTF_{37°C}$ of Al_2O_3-Parylene C (~ 36 months) is an improvement over Parylene C (~ 8 months).

The EIS spectra and equivalent circuit models suggest that there are two modes of failure in the tested IDEs The same circuit fits intact IDEs as well as that fail after longest immersion time (longer than 1,000 hours). These failures could be due to blistering of the or microscopic delamination (Yasuda, Yu, and Chen 2001)(Fernández-Sánchez, McNeil, and Rawson 2005) of the polymeric Parylene C coating allowing large volume of

electrolyte penetration. The second mode of failure is consistent with pore formation where electrolyte penetrates the insulation coating. These failure modes are common for polymeric coatings as these layers are porous allowing water and salts to permeate (Massey 2002). The common reported modes of failure are delamination, blistering, and formation of micro-pores(Huang et al. 2008) (Hassler et al. 2010)(Lee et al. 2011)(Hara et al. 2012). Li et al reported that Parylene C coatings failed due to magnification of electrical stresses at imperfection sites causing micro-cracks followed by delamination (Li et al. 2010). Other polymeric coatings show similar modes of failure. Parylene N coatings failure during soak tests was related to micro-cracks formation instead of delamination. Polyimide sandwiched layers failed due to dissolution, delamination, and blistering (Lee et al. 2011) possibly due "outgassing of trapped moisture" (Stark and Najafi 2001).

Here intact coatings maintained high impedances over the 3 month study period while the failed coatings show a decrease in impedance and increase in phase angles from –80° indicative of electrolyte access to underlying metal. A common metric to evaluate the performance of implantable neural electrodes is the impedance modulus at 1 kHz. It is important to recognize that 6 out of 8 failing IDE samples in this study showed no decrease in the impedance modulus at 1 kHz (figure 7.9). The insulation coating has to fail drastically such that its value is lower than the dominating capacitive impedance to reflect changes at higher frequencies (Zuo et al. 2008). Thus, reliance on 1 kHz impedance modulus should not be solely used as a performance metric for material stability for neural electrodes.

The significance of IDE coating failures in our testing paradigm on the overall functionality of implanted microelectrode arrays is difficult to extrapolate. Indeed, EIS is very sensitive to minute changes in film integrity. However the ability of an implanted microelectrode with pinholes or delamination to continue to record neuronal biopotentials will depend on volume conductor conditions. Nevertheless, it is apparent that the insulating character of Al_2O_3-Parylene C is significantly improved over Parylene C alone, suggesting that this is a promising material modification for increasing neural interface reliability.

CHAPTER 8: CONCLUSIONS

This thesis is a culmination of experimental and modeling work conducted on implantable conducting and insulating coatings for neural interfaces. Conducting materials investigated were electrodeposited iridium oxide films and electrophoretically deposited multi-walled carbon nanotubes. Parylene C and bilayer Al_2O_3-Parylene C barrier properties were compared to assess the mean time to failure under age acceleration conditions.

EPD-MWCNTs microwires were tested using electrochemical characterizations *in vitro* and *in vivo* to evaluate the **impact of the tissue** on the electrical performance of the electrode. Not only did the MWCNT microwires maintain their CSCc and redox peaks, the impedance modulus was not significantly different ($p>0.05$ for frequencies 0.01 Hz to 2 kHz) when implanted in deep brain structures. This behavior is contrary to traditional stimulation electrodes such as EIROFs, where a 30 % decrease in charge delivered and increase in impedance is observed. Increase in impedance at higher frequencies for MWCNT microwires (> 2 kHz) is due to the dominance of tissue properties whereas at lower frequencies it's the electrode processes that take over (Gimsa et al., 2005).

The impact **on the tissue** due to MWCNT microwires and electrochemical characterization was evaluated by studying the transcription levels of cytokine IL-1β and TLR2, both known to be involved in the inflammatory reaction due to implantation (Babcock et al. 2006; Saxena et al. 2013). Evaluation of inflammatory molecules revealed that transcripts for the cytokine IL-1β were up-regulated in response to low-frequency stimulation, whereas no modulation was observed for TLR2. This result indicates that the early response of the brain to mechanical trauma and low-frequency stimulation activated the IL-1β signaling cascade but not that of TLR2.

For EIROF microwires the **applicability of *in vitro* models as an *in vivo* model was tested with and without low frequency stimulation.** Two separate models fit the *in vitro* and *in vivo* impedance spectra depending on the application of slow CV cycle (-0.7 V to 0. 7V at 50 mV/s) stimulation prior to EIS measurement. Interestingly the *in vivo* impedance behavior of EIROF microwires following the CV cycles were similar to the impedance of SIROF electrodes stimulated with current pulses (Weiland and Anderson 2000). The mid frequency (10 Hz - 1 kHz) *in vitro* and *in vivo* impedance were similar. The low and high frequency ranges in the *in vivo* impedance increased over the *in vitro* values. EIROF microwires presented with reduced CSCc (30 %) *in vivo* unlike MWCNT microwires. The reduction-oxidation peaks were absent in EIROF CVs' in deep brain structure (rat hippocampi). These changes reflect a modification in the double layer composition due to electro-bio-chemical interactions occurring *in vivo*.

The lifetime and stability of insulation are critical features for reliable operation of an implantable neural interface device. A comprehensive study was conducted to

examine the MTTF of Parylene C and Al_2O_3-Parylene C coated devices using accelerated lifetime testing at 60 °C. The $MTTF_{60°C}$ for Al_2O_3-Parylene C was 4.6 times longer than Parylene-C coated samples. The extrapolated $MTTF_{37°C}$ of Al_2O_3-Parylene C (~ 36 months) is an improvement over Parylene C (~ 8 months). The EIS spectra and equivalent circuit models suggests that there are two modes of failure in the tested IDEs. IDEs failing after long immersion time (months) fit the same equivalent circuit as an intact insulation coated IDE. These failures could be due to of exposed Al_2O_3 (Abdulagatov et al. 2011) or microscopic delamination (Yasuda, Yu, and Chen 2001)(Fernández-Sánchez, McNeil, and Rawson 2005) of the polymeric coating. The second, usually faster, mode of failure is consistent with pore or blister formation where electrolyte penetrates the insulation coating.

Characterizing the difference in electrochemical behavior at the electrode interface between *in vitro* and *in vivo* difference in environment is useful in identifying the important parameters to increase the efficiency of conductive implant materials. For example, varying deposition parameters, combining different materials, and electrically modulating the interface prior to recording or stimulation. These techniques can be used to develop protocols where the performance is controlled in a frequency dependent manner based on its requirements. Long-term reliability on insulation with insights to failure can be used to devise models that quantify the capacity of implanted microelectrodes with pinholes or delamination to record or stimulate neuronal tissue. This could provide a realistic metric on the acceptable tolerance level for a reliable insulation/encapsulation on neural interfaces.

REFERENCES

A.Aarts, H.P. Neves, I. Ulbert, L. Wittner, L. Grand, M. B A Fontes, S. Herwik, et al. 2008. "A 3D Slim-base Probe Array for *in vivo* Recorded Neuron Activity." In *30th Annual International Conference of the IEEE Engineering in Medicine and Biology Society, 2008. EMBS 2008*, 5798–5801. doi:10.1109/IEMBS.2008.4650532.

A. I. Abdulagatov, Y. Yan, J. R. Cooper, Y. Zhang, Z. M. Gibbs, A. S. Cavanagh, R. G. Yang, Y. C. Lee, and S. M. George. 2011. "Al2O3 and TiO2 Atomic Layer Deposition on Copper for Water Corrosion Resistance." *ACS Applied Materials & Interfaces* 3 (12) (December 28): 4593–4601. doi:10.1021/am2009579.

M.D. Abramoff, P.J. Magelhaes, and S.J. Ram. 2004. "Image Processing with ImageJ." *Biophotonics International* 11 (7): 36–42.

P. M. Ajayan, 1999. "Nanotubes from Carbon." *Chemical Reviews* 99 (7) (July 1): 1787–1800. doi:10.1021/cr970102g.

E. Akbarinezhad, and H. R. Faridi. 2008. "Different Approaches in Evaluating Organic Paint Coatings with Electrochemical Impedance Spectroscopy." *Surface Engineering* 24 (4): 280–286. doi:10.1179/174329408X326524.

J. Anderson. 2004. "Inflammation, Wound Healing, and the Foreign Body Response." In *Biomaterials Science: An Introduction to Materials in Medicine*, edited by Buddy D. Ratner. Academic Press.

D.L. Andre, S. Balaji, M. Jonathan, D. Corina, and G.J. Bruce. 2009. "Mechanisms Determining Safety and Performance of Brain Stimulating Electrodes." *Conference Proceedings : Annual International Conference of the IEEE Engineering in Medicine and Biology Society. IEEE Engineering in Medicine and Biology Society. Conference* 2009: 689–692. doi:10.1109/IEMBS.2009.5334136.

A. Ansaldo, C. Elisa, M. Emma, F.Luciano, and R. Davide. 2011. "Superior Electrochemical Performance of Carbon Nanotubes Directly Grown on Sharp Microelectrodes." *ACS Nano* 5 (3). doi:10.1021/nn103445d. http://pubs.acs.org.mutex.gmu.edu/doi/abs/10.1021/nn103445d.

P. Ashby, Y. J. Kim, R. Kumar, A. E. Lang, and A. M. Lozano. 1999. "Neurophysiological Effects of Stimulation through Electrodes in the Human Subthalamic Nucleus." *Brain* 122 (10) (October 1): 1919 –1931. doi:10.1093/brain/122.10.1919.

B. Aurian-Blajeni, X. Beebe, R.D. Rauh, and T.L. Rose. 1989. "Impedance of Hydrated Iridium Oxide Electrodes." *Electrochimica Acta* 34 (6) (June): 795–802. doi:10.1016/0013-4686(89)87112-9.

A., Shirley, R. Boot-Handford, M. Humphries, K. Kadler, and A. Shuttleworth. 1998. *The Extracellular Matrix Factsbook*. Academic Press.

E. Azzarello, E. Masi, and S. Mancuso. 2012. "Electrochemical Impedance Spectroscopy." In *Plant Electrophysiology*, edited by Alexander G. Volkov, 205–223. Springer Berlin Heidelberg. http://link.springer.com/chapter/10.1007/978-3-642-29119-7_9.

A.A. Babcock, M. Wirenfeldt, T. Holm, H. H. Nielsen, L. Dissing-Olesen, H. Toft-Hansen, J. M. Millward, et al. 2006. "Toll-Like Receptor 2 Signaling in Response to Brain Injury: An Innate Bridge to Neuroinflammation." *The Journal of Neuroscience* 26 (49) (December 6): 12826–12837. doi:10.1523/JNEUROSCI.4937-05.2006.

C.E. Banks, A. Crossley, C. Salter, S. J. Wilkins, and R. G. Compton. 2006. "Carbon Nanotubes Contain Metal Impurities Which Are Responsible for the 'Electrocatalysis' Seen at Some Nanotube-Modified Electrodes." *Angewandte Chemie International Edition* 45 (16): 2533–2537. doi:10.1002/anie.200600033.

A.J. Bard, and L. R Faulkner. 2006. *Electrochemical Methods: Fundamentals and Applications*. A1bazaar.

L. Bareket-Keren, and Y. Hanein. 2013. "Carbon Nanotube-based Multi Electrode Arrays for Neuronal Interfacing: Progress and Prospects." *Frontiers in Neural Circuits* 6: 122. doi:10.3389/fncir.2012.00122.

J.N. Barisci, Gordon G. Wallace, and Ray H. Baughman. 2000. "Electrochemical Studies of Single-wall Carbon Nanotubes in Aqueous Solutions." *Journal of Electroanalytical Chemistry* 488 (2) (July 14): 92–98. doi:10.1016/S0022-0728(00)00179-0.

E. Barsoukov, and J. R. Macdonald. 2005. *Impedance Spectroscopy: Theory, Experiment, and Applications*. John Wiley & Sons.

Y. Barsukov, and J. R. Macdonald. 2002. “Electrochemical Impedance Spectroscopy.” In *Characterization of Materials*. John Wiley & Sons, Inc. http://onlinelibrary.wiley.com/doi/10.1002/0471266965.com124/abstract.

J.E. Baur, and T. W. Spaine. 1998. “Electrochemical Deposition of Iridium (IV) Oxide from Alkaline Solutions of iridium(III) Oxide.” *Journal of Electroanalytical Chemistry* 443 (2) (February 20): 208–216. doi:10.1016/S0022-0728(97)00532-9.

M. Baxendale, 2003. “Biomolecular Applications of Carbon Nanotubes.” *Nanobiotechnology, IEE Proceedings* - 150 (1): 3–8. doi:10.1049/ip-nbt:20030576.

E. Ben-Jacob, and Y. Hanein. 2008. “Carbon Nanotube Micro-electrodes for Neuronal Interfacing.” *Journal of Materials Chemistry* 18 (43): 5181–5186.

G. Bierwagen, D. Tallman, J. Li, L. He, and C. Jeffcoate. 2003. “EIS Studies of Coated Metals in Accelerated Exposure.” *Progress in Organic Coatings* 46 (2) (March): 149–158. doi:10.1016/S0300-9440(02)00222-9.

R. Biran, D. C. Martin, and P. A. Tresco. 2005. “Neuronal Cell Loss Accompanies the Brain Tissue Response to Chronically Implanted Silicon Microelectrode Arrays.” *Experimental Neurology* 195 (1) (September): 115–126. doi:10.1016/j.expneurol.2005.04.020.

V.I. Birss, and P. G. Pickup. 1988. “The Electrochemistry of Iridium Oxide Films in Some Nonaqueous Solvents.” http://dspace.ucalgary.ca/jspui/handle/1880/44748.

A.R. Boccaccini, J. Cho, J. A. Roether, B. J.C. Thomas, E. J. Minay, and M. S.P. Shaffer. 2006. “Electrophoretic Deposition of Carbon Nanotubes.” *Carbon* 44 (15) (December): 3149–3160. doi:10.1016/j.carbon.2006.06.021.

J.A. Boockvar, A. Telfeian, G. H. Baltuch, B. Skolnick, T. Simuni, M. Stern, M. L. Schmidt, and J. Q. Trojanowski. 2000. “Long-term Deep Brain Stimulation in a Patient with Essential Tremor: Clinical Response and Postmortem Correlation with Stimulator Termination Sites in Ventral Thalamus.” *Journal of Neurosurgery* 93 (1) (July): 140–144. doi:10.3171/jns.2000.93.1.0140.

S.B. Brummer, and M. J. Turner. 1977. “Electrochemical Considerations for Safe Electrical Stimulation of the Nervous System with Platinum Electrodes.” *IEEE Transactions on Biomedical Engineering* BME-24 (1): 59–63. doi:10.1109/TBME.1977.326218.

P.A. Carpentier, W. S. Begolka, J. K. Olson, A. Elhofy, W. J. Karpus, and S.D. Miller. 2005. “Differential Activation of Astrocytes by Innate and Adaptive Immune Stimuli.” *Glia* 49 (3): 360–374. doi:10.1002/glia.20117.

A.M. Cassell, J. A. Raymakers, J. Kong, and H. Dai. 1999. “Large Scale CVD Synthesis of Single-Walled Carbon Nanotubes.” *The Journal of Physical Chemistry B* 103 (31): 6484–6492. doi:10.1021/jp990957s.

B.Y. Chang, and S.M. Park. 2010. “Electrochemical Impedance Spectroscopy.” *Annual Review of Analytical Chemistry* 3 (1): 207–229. doi:10.1146/annurev.anchem.012809.102211.

J.H. Chang, B. Lu, and Y.C. Tai. 2011. “Adhesion-enhancing Surface Treatments for Parylene Deposition.” In *Solid-State Sensors, Actuators and Microsystems Conference (TRANSDUCERS), 2011 16th International*, 390 –393. doi:10.1109/TRANSDUCERS.2011.5969484.

T.Y. Chang, V. G. Yadav, S. D. Leo, A. Mohedas, B. Rajalingam, C.L. Chen, S. Selvarasah, M. R. Dokmeci, and A. Khademhosseini. 2007. “Cell and Protein Compatibility of Parylene-C Surfaces.” *Langmuir* 23 (23) (November 1): 11718–11725. doi:10.1021/la7017049.

M. Cieślik, K. Engvall, J. Pan, and A. Kotarba. 2011. “Silane–parylene Coating for Improving Corrosion Resistance of Stainless Steel 316L Implant Material.” *Corrosion Science* 53 (1) (January): 296–301. doi:10.1016/j.corsci.2010.09.034.

G. Ciofani, V. Raffa, O. Vittorio, A. Cuschieri, T. Pizzorusso, M. Costa, and G. Bardi. 2010. “*In vitro* and *in vivo* Biocompatibility Testing of Functionalized Carbon Nanotubes.” *Methods in Molecular Biology (Clifton, N.J.)* 625: 67–83. doi:10.1007/978-1-60761-579-8_7.

S.F. Cogan, 2006. “*In vivo* and *In vitro* Differences in the Charge-injection and Electrochemical Properties of Iridium Oxide Electrodes.” In *28th Annual International Conference of the IEEE Engineering in Medicine and Biology Society, 2006. EMBS ’06*, 882–885. doi:10.1109/IEMBS.2006.259654.

S.F. Cogan, J. Ehrlich, T.D. Plante, and R. V. Wagenen. 2009. “Penetrating Microelectrode Arrays with Low-impedance Sputtered Iridium Oxide Electrode Coatings.” In *Annual International Conference of the IEEE Engineering in Medicine and Biology Society, 2009. EMBC 2009*, 7147–7150. doi:10.1109/IEMBS.2009.5335359.

S.F. Cogan, A. A Guzelian, W. F Agnew, T.G.H Yuen, and D. B McCreery. 2004. “Over-pulsing Degrades Activated Iridium Oxide Films Used for Intracortical Neural Stimulation.” *Journal of Neuroscience Methods* 137 (2) (August 30): 141–150. doi:10.1016/j.jneumeth.2004.02.019.

S.F. Cogan. 2008. “Neural Stimulation and Recording Electrodes.” *Annual Review of Biomedical Engineering* 10 (1): 275–309. doi:10.1146/annurev.bioeng.10.061807.160518.

S.F. Cogan, J. Ehrlich, T. D. Plante, A. Smirnov, D. B. Shire, M. Gingerich, and J. F. Rizzo. 2004. “Sputtered Iridium Oxide Films (SIROFs) for Neural Stimulation Electrodes.” *Conference Proceedings : Annual International Conference of the IEEE Engineering in Medicine and Biology Society. IEEE Engineering in Medicine and Biology Society. Conference* 6: 4153–4156. doi:10.1109/IEMBS.2004.1404158.

S.F. Cogan, J. Ehrlich, T. D. Plante, A. Smirnov, D. B. Shire, M. Gingerich, and J. F. Rizzo. 2009. “Sputtered Iridium Oxide Films for Neural Stimulation Electrodes.” *Journal of Biomedical Materials Research Part B: Applied Biomaterials* 89B (2): 353–361. doi:10.1002/jbm.b.31223.

S.F. Cogan, P. R. Troyk, J. Ehrlich, C. M. Gasbarro, and T. D. Plante. 2007. “The Influence of Electrolyte Composition on the *In vitro* Charge-injection Limits of Activated Iridium Oxide (AIROF) Stimulation Electrodes.” *Journal of Neural Engineering* 4 (2) (June 1): 79. doi:10.1088/1741-2560/4/2/008.

C. Corfias, N. Pebere, and C. Lacabanne. 1999. “Characterization of a Thin Protective Coating on Galvanized Steel by Electrochemical Impedance Spectroscopy and a Thermostimulated Current Method.” *Corrosion Science* 41 (8) (August 1): 1539–1555. doi:10.1016/S0010-938X(98)00203-0.

H.G. Craighead, S. W. Turner, R. C. Davis, C. James, A. M. Perez, P. M. St. John, M. S. Isaacson, et al. 1998. “Chemical and Topographical Surface Modification for Control of Central Nervous System Cell Adhesion.” *Biomedical Microdevices* 1 (1): 49–64. doi:10.1023/A:1009982306118.

X. Cui, and D. C. Martin. 2003. “Electrochemical Deposition and Characterization of Poly (3, 4-ethylenedioxythiophene) on Neural Microelectrode Arrays.” *Sensors and Actuators B: Chemical* 89 (1-2): 92–102.

N. Didier, I. A. Romero, C. Créminon, A. Wijkhuisen, J. Grassi, and A. Mabondzo. 2003. “Secretion of Interleukin-1β by Astrocytes Mediates Endothelin-1 and Tumour Necrosis Factor-α Effects on Human Brain Microvascular Endothelial Cell Permeability.” *Journal of Neurochemistry* 86 (1): 246–254. doi:10.1046/j.1471-4159.2003.01829.x.

M.S. Dresselhaus, G. Dresselhaus, J. C. Charlier, and E. Hernández. 2004. “Electronic, Thermal and Mechanical Properties of Carbon Nanotubes.” *Philosophical Transactions of the Royal Society of London. Series A: Mathematical, Physical*

and Engineering Sciences 362 (1823) (October 15): 2065–2098. doi:10.1098/rsta.2004.1430.

Duan, Y.Y., G.M. Clark, and R.S.C. Cowan. 2004. "A Study of Intra-cochlear Electrodes and Tissue Interface by Electrochemical Impedance Methods *in vivo*." *Biomaterials* 25 (17) (August): 3813–3828. doi:10.1016/j.biomaterials.2003.09.107.

Edell, D.J., V.V. Toi, V.M. McNeil, and L.D. Clark. 1992. "Factors Influencing the Biocompatibility of Insertable Silicon Microshafts in Cerebral Cortex." *IEEE Transactions on Biomedical Engineering* 39 (6): 635–643. doi:10.1109/10.141202.

S. Eick, J. Wallys, B. Hofmann, A. van Ooyen, U. Schnakenberg, S. Ingebrandt, and A. Offenhausser. 2009. "Iridium Oxide Microelectrode Arrays for *In vitro* Stimulation of Individual Rat Neurons from Dissociated Cultures." *Frontiers in Neuroengineering* 2 (November 16). doi:10.3389/neuro.16.016.2009. http://www.ncbi.nlm.nih.gov/pmc/articles/PMC2783441/.

H. A. Elsen, C. F. Monson, and M. Majda. 2009. "Effects of Electrodeposition Conditions and Protocol on the Properties of Iridium Oxide pH Sensor Electrodes." *Journal of The Electrochemical Society* 156 (1) (January 1): F1–F6. doi:10.1149/1.3001924.

C. Ethier, E. R. Oby, M. J. Bauman, and L. E. Miller. 2012. "Restoration of Grasp Following Paralysis through Brain-controlled Stimulation of Muscles." *Nature* 485 (7398) (May 17): 368–371. doi:10.1038/nature10987.

W.C. Fang, J.H. Huang, L.C. Chen, Y. O. Su, K.H. Chen, and C.L. Sun. 2006. "Carbon Nanotubes Grown Directly on Ti Electrodes and Enhancement of Their Electrochemical Properties by Nitric Acid Treatment." *Electrochemical and Solid-State Letters* 9 (1) (January): A5–A8. doi:10.1149/1.2128123.

K. Fassbender, S. Schneider, T. Bertsch, D. Schlueter, M. Fatar, A. Ragoschke, S. Kühl, U. Kischka, and M. Hennerici. 2000. "Temporal Profile of Release of Interleukin-1β in Neurotrauma." *Neuroscience Letters* 284 (3) (April 28): 135–138. doi:10.1016/S0304-3940(00)00977-0.

C. Fernández-Sánchez, C. J. McNeil, and K. Rawson. 2005. "Electrochemical Impedance Spectroscopy Studies of Polymer Degradation: Application to Biosensor Development." *TrAC Trends in Analytical Chemistry* 24 (1) (January): 37–48. doi:10.1016/j.trac.2004.08.010.

M. Figee, J. Luigjes, R. Smolders, C.E.V. Alfonso, G. van Wingen, B. de Kwaasteniet, M. Mantione, et al. 2013. "Deep Brain Stimulation Restores Frontostriatal

Network Activity in Obsessive-compulsive Disorder." *Nature Neuroscience* 16 (4) (April): 386–387. doi:10.1038/nn.3344.

W. Franks, I. Schenker, P. Schmutz, and A. Hierlemann. 2005. "Impedance Characterization and Modeling of Electrodes for Biomedical Applications." *IEEE Transactions on Biomedical Engineering* 52 (7): 1295–1302. doi:10.1109/TBME.2005.847523.

H. Fritzsche, 1972. "Electronic Processes in Non-Crystalline Materials. N. F. Mott and E. A. Davis. Oxford University Press, New York, 1971. Xiv, 438 Pp., Illus. $24. International Series of Monographs on Physics." *Science* 176 (4039) (June 9): 1117–1117. doi:10.1126/science.176.4039.1117.

P. Galvan-Garcia, E. W. Keefer, F. Yang, M. Zhang, S. Fang, A. A. Zakhidov, R. H. Baughman, and M. I. Romero. 2007. "Robust Cell Migration and Neuronal Growth on Pristine Carbon Nanotube Sheets and Yarns." *Journal of Biomaterials Science, Polymer Edition* 18 (10): 1245–1261.

S. Gawad, M. Giugliano, M. Heuschkel, B. Wessling, H. Markram, U. Schnakenberg, P. Renaud, and H. Morgan. 2009. "Substrate Arrays of Iridium Oxide Microelectrodes for *In vitro* Neuronal Interfacing." *Frontiers in Neuroengineering* 2 (January 22). doi:10.3389/neuro.16.001.2009. http://www.ncbi.nlm.nih.gov/pmc/articles/PMC2634525/.

K. Göbbels, T. Kuenzel, A. Ooyen, W. Baumgartner, U. Schnakenberg, and P. Bräunig. 2010. "Neuronal Cell Growth on Iridium Oxide." *Biomaterials* 31 (6) (February): 1055–1067. doi:10.1016/j.biomaterials.2009.10.029.

J. Gooding, and J. Justin. 2005. "Nanostructuring Electrodes with Carbon Nanotubes: A Review on Electrochemistry and Applications for Sensing." *Electrochimica Acta* 50 (15) (May 20): 3049–3060. doi:10.1016/j.electacta.2004.08.052.

W. F. Gorham. 1966. "A New, General Synthetic Method for the Preparation of Linear Poly-p-xylylenes." *Journal of Polymer Science Part A-1: Polymer Chemistry* 4 (12): 3027–3039. doi:10.1002/pol.1966.150041209.

R. A. Green, C. M. Williams, N. H. Lovell, and L. A. Poole-Warren. 2008. "Novel Neural Interface for Implant Electrodes: Improving Electroactivity of Polypyrrole through MWNT Incorporation." *Journal of Materials Science: Materials in Medicine* 19 (4) (January): 1625–1629. doi:10.1007/s10856-008-3376-7.

R.W. Griffith, and D. R. Humphrey. 2006. "Long-term Gliosis Around Chronically Implanted Platinum Electrodes in the Rhesus Macaque Motor Cortex." *Neuroscience Letters* 406 (1-2) (October 2): 81–86. doi:10.1016/j.neulet.2006.07.018.

W.M. Grill, and J. T. Mortimer. 1994. “Electrical Properties of Implant Encapsulation Tissue.” *Annals of Biomedical Engineering* 22 (1) (January 1): 23–33. doi:10.1007/BF02368219.

L. Guo, D. G. Morris, X. Liu, C. Vaslet, R. H. Hurt, and A. B. Kane. 2007. “Iron Bioavailability and Redox Activity in Diverse Carbon Nanotube Samples.” *Chemistry of Materials* 19 (14) (July 1): 3472–3478. doi:10.1021/cm062691p.

D.L. Guyton, and F. T. Hambrecht. 1974. “Theory and Design of Capacitor Electrodes for Chronic Stimulation.” *Medical & Biological Engineering* 12 (5) (September): 613–620. doi:10.1007/BF02477223.

M. Han, P.S. Manoonkitiwongsa, C.X. Wang, and D.B. McCreery. “*In vivo* Validation of Custom-Designed Silicon-Based Microelectrode Arrays for Long-Term Neural Recording and Stimulation.” *IEEE Transactions on Biomedical Engineering* 59 (2): 346–354. doi:10.1109/TBME.2011.2172440.

U.K. Hanisch. 2002. “Microglia as a Source and Target of Cytokines.” *Glia* 40 (2): 140–155. doi:10.1002/glia.10161.

S.A. Hara, B.J. Kim, J.T.W. Kuo, C. Lee, C.A. Gutierrez, T. Hoang, and E. Meng. 2012. “Pre-implantation Electrochemical Characterization of a Parylene C Sheath Microelectrode Array Probe.” In *2012 Annual International Conference of the IEEE Engineering in Medicine and Biology Society (EMBC)*, 5126 –5129. doi:10.1109/EMBC.2012.6347147.

B.S. Harrison, and A. Atala. 2007. “Carbon Nanotube Applications for Tissue Engineering.” *Biomaterials* 28 (2) (January): 344–353. doi:10.1016/j.biomaterials.2006.07.044.

C. Hassler, T. Boretius, and T. Stieglitz. 2011. “Polymers for Neural Implants.” *Journal of Polymer Science Part B: Polymer Physics* 49 (1): 18–33. doi:10.1002/polb.22169.

C. Hassler, R. P. von Metzen, P. Ruther, and T. Stieglitz. 2010. “Characterization of Parylene C as an Encapsulation Material for Implanted Neural Prostheses.” *Journal of Biomedical Materials Research Part B: Applied Biomaterials* 93B (1): 266–274. doi:10.1002/jbm.b.31584.

L.R. Hochberg, D. Bacher, B. Jarosiewicz, N. Y. Masse, J. D. Simeral, J. Vogel, S. Haddadin, et al. 2012. “Reach and Grasp by People with Tetraplegia Using a Neurally Controlled Robotic Arm.” *Nature* 485 (7398) (May 17): 372–375. doi:10.1038/nature11076.

R. Hornig, T. Laube, P. Walter, M.Velikay-Parel, N. Bornfeld, M. Feucht, H. Akguel, et al. 2005. “A Method and Technical Equipment for an Acute Human Trial to Evaluate Retinal Implant Technology.” *Journal of Neural Engineering* 2 (1) (March 1): S129–S134. doi:10.1088/1741-2560/2/1/014.

J.M. Hsu, L. Rieth, R.A. Normann, P. Tathireddy, and F. Solzbacher. 2009. “Encapsulation of an Integrated Neural Interface Device With Parylene C.” *IEEE Transactions on Biomedical Engineering* 56 (1) (January): 23 –29. doi:10.1109/TBME.2008.2002155.

C.G. Hu, W.L. Wang, K.J. Liao, G.B. Liu, and Y.T. Wang. 2004. “Systematic Investigation on the Properties of Carbon Nanotube Electrodes with Different Chemical Treatments.” *Journal of Physics and Chemistry of Solids* 65 (10) (October): 1731–1736. doi:10.1016/j.jpcs.2004.04.009.

Z. Hu, P. Troyk, G. DeMichele, K. Kayvani, and S. Suh. 2012. “Intrinsic Activation of Iridium Electrodes over a Wireless Link.” In *2012 Annual International Conference of the IEEE Engineering in Medicine and Biology Society (EMBC)*, 2788–2791. doi:10.1109/EMBC.2012.6346543.

R. Huang, C. Pang, Y. Tai, J. Emken, C. Ustun, and R. Andersen. 2008. “Parylene Coated Silicon Probes for Neural Prosthesis.” In *3rd IEEE International Conference on Nano/Micro Engineered and Molecular Systems, 2008. NEMS 2008*, 947 –950. doi:10.1109/NEMS.2008.4484478.

D. W. L Hukins, A. Mahomed, and S.N. Kukureka. 2008. “Accelerated Aging for Testing Polymeric Biomaterials and Medical Devices.” *Medical Engineering & Physics* 30 (10) (December): 1270–1274. doi:10.1016/j.medengphy.2008.06.001.

M. Hüppauff, and B. Lengeler. 1993. “Valency and Structure of Iridium in Anodic Iridium Oxide Films.” *Journal of The Electrochemical Society* 140 (3) (March 1): 598–602. doi:10.1149/1.2056127.

S. Iijima, and T. Ichihashi. 1993. “Single-shell Carbon Nanotubes of 1-nm Diameter.” *Nature* 363 (6430) (June 17): 603–605. doi:10.1038/363603a0.

C.S. Jack, N. Arbour, J. Manusow, V. Montgrain, M. Blain, E. McCrea, A. Shapiro, and J. P. Antel. 2005. “TLR Signaling Tailors Innate Immune Responses in Human Microglia and Astrocytes.” *The Journal of Immunology* 175 (7) (October 1): 4320–4330.

E. Jan, J. L. Hendricks, V. Husaini, S. M. Richardson-Burns, A. Sereno, D. C. Martin, and N. A. Kotov. 2009. “Layered Carbon Nanotube-Polyelectrolyte Electrodes Outperform Traditional Neural Interface Materials.” *Nano Letters* 9 (12) (December 9): 4012–4018. doi:10.1021/nl902187z.

E. Jan, and N. A. Kotov. 2007. “Successful Differentiation of Mouse Neural Stem Cells on Layer-by-Layer Assembled Single-Walled Carbon Nanotube Composite.” *Nano Letters* 7 (5) (May 1): 1123–1128. doi:10.1021/nl0620132.

A. Kahouli, A. Sylvestre, L. Ortega, F. Jomni, B. Yangui, M. Maillard, B. Berge, J.-C. Robert, and J. Legrand. 2009. “Structural and Dielectric Study of Parylene C Thin Films.” *Applied Physics Letters* 94 (15): 152901. doi:10.1063/1.3114404.

S. Kane, S.F. Cogan, T. Plante, J. Ehrlich, D. McCreery, and P. Troyk. 2013. “Electrical Performance of Penetrating Microelectrodes Chronically Implanted in Cat Cortex.” *IEEE Transactions on Bio-medical Engineering* (February 26). doi:10.1109/TBME.2013.2248152.

S. R. Kane, S. F. Cogan, J. Ehrlich, T. D. Plante, and D. B. McCreery. 2011. “Electrical Performance of Penetrating Microelectrodes Chronically Implanted in Cat Cortex.” In *2011 Annual International Conference of the IEEE Engineering in Medicine and Biology Society,EMBC*, 5416–5419. doi:10.1109/IEMBS.2011.6091339.

E. W. Keefer, B. R. Botterman, M. I. Romero, A. F. Rossi, and G. W. Gross. 2008. “Carbon Nanotube Coating Improves Neuronal Recordings.” *Nat Nano* 3 (7) (July): 434–439. doi:10.1038/nnano.2008.174.

P. R. Kennedy, M.T. Kirby, M.M. Moore, B. King, and A. Mallory. 2004. “Computer Control Using Human Intracortical Local Field Potentials.” *IEEE Transactions on Neural Systems and Rehabilitation Engineering* 12 (3): 339–344. doi:10.1109/TNSRE.2004.834629.

D. Khang, S. Y. Kim, P. Liu-Snyder, G. T. R. Palmore, S. M. Durbin, and T. J. Webster. 2007. “Enhanced Fibronectin Adsorption on Carbon Nanotube/poly(carbonate) Urethane: Independent Role of Surface Nano-roughness and Associated Surface Energy.” *Biomaterials* 28 (32) (November): 4756–4768. doi:10.1016/j.biomaterials.2007.07.018.

M.L. Khraiche, N. Jackson, and J. Muthuswamy. 2009. “Early Onset of Electrical Activity in Developing Neurons Cultured on Carbon Nanotube Immobilized Microelectrodes.” *Conference Proceedings: Annual International Conference of the IEEE Engineering in Medicine and Biology Society. IEEE Engineering in Medicine and Biology Society. Conference* 2009: 777–780. doi:10.1109/IEMBS.2009.5333590.

R. Krupke, F. Hennrich, H. v. Löhneysen, and M. M. Kappes. 2003. “Separation of Metallic from Semiconducting Single-Walled Carbon Nanotubes.” *Science* 301 (5631) (July 18): 344 –347. doi:10.1126/science.1086534.

R. Kurrat, J. E. Prensloi and J. J. Ramsden. 1997. “Kinetics of Human and Bovine Serum Albumin Adsorption at Silica-Titania Surfaces.” *Journal of Colloid and Interface Science* 185 (1) (January 1): 1–8.

L. Lacerda, A. Bianco, M. Prato, and K. Kostarelos. 2006. “Carbon Nanotubes as Nanomedicines: From Toxicology to Pharmacology.” *Advanced Drug Delivery Reviews* 58 (14) (December 1): 1460–1470. doi:10.1016/j.addr.2006.09.015.

A. Lasia. 1999. “Electrochemical Impedance Spectroscopy and Its Applications.” *Modern Aspects of Electrochemistry* 32: 143–248.

A. W. Laxton, D. F. Tang-Wai, M. P. McAndrews, D. Zumsteg, R. Wennberg, R. Keren, J. Wherrett, et al. 2010. “A Phase I Trial of Deep Brain Stimulation of Memory Circuits in Alzheimer’s Disease.” *Annals of Neurology* 68 (4) (October): 521–534. doi:10.1002/ana.22089.

I. S. Lee, C. N. Whang, J. C. Park, D. H. Lee, and W.S. Seo. 2003. “Biocompatibility and Charge Injection Property of Iridium Film Formed by Ion Beam Assisted Deposition.” *Biomaterials* 24 (13) (June): 2225–2231. doi:10.1016/S0142-9612(03)00025-5.

S. W. Lee, K. S. Min, J. Jeong, J. Kim, and S. J. Kim. 2011. “Monolithic Encapsulation of Implantable Neuroprosthetic Devices Using Liquid Crystal Polymers.” *IEEE Transactions on Biomedical Engineering* 58 (8): 2255–2263. doi:10.1109/TBME.2011.2136341.

W. Lee, and V. Parpura. 2009. “Chapter 6 - Carbon Nanotubes as Substrates/scaffolds for Neural Cell Growth.” *Progress in Brain Research* 180: 110–125. doi:10.1016/S0079-6123(08)80006-4.

S. F. Lempka, S. Miocinovic, M. D. Johnson, J. L. Vitek, and C. C. McIntyre. 2009. “*In vivo* Impedance Spectroscopy of Deep Brain Stimulation Electrodes.” *Journal of Neural Engineering* 6 (4) (August 1): 046001. doi:10.1088/1741-2560/6/4/046001.

R. M. Levy, S. Lamb, and J. E. Adams. 1987. “Treatment of Chronic Pain by Deep Brain Stimulation: Long Term Follow-up and Review of the Literature.” *Neurosurgery* 21 (6) (December): 885–893.

J. Li, C.S. Jeffcoate, G.P. Bierwagen, D. J. Mills, and D. E. Tallman. 1998. “Thermal Transition Effects and Electrochemical Properties in Organic Coatings: Part 1 Initial Studies on Corrosion Protective Organic Coatings.” *Corrosion* 54: 763–771.

W. Li, D.C. Rodger, E. Meng, J. D. Weiland, M. S. Humayun, and Y. C. Tai. 2010. "Wafer-Level Parylene Packaging With Integrated RF Electronics for Wireless Retinal Prostheses." *Journal of Microelectromechanical Systems* 19 (4): 735–742. doi:10.1109/JMEMS.2010.2049985.

X. Liu, D. B. McCreery, R. R. Carter, L. A. Bullara, T. G. H. Yuen, and W. F. Agnew. 1999. "Stability of the Interface Between Neural Tissue and Chronically Implanted Intracortical Microelectrodes." *IEEE Transactions on Rehabilitation Engineering* 7 (3) (September): 315 –326. doi:10.1109/86.788468.

A. O. Lobo, E. F. Antunes, A. H. A. Machado, C. Pacheco-Soares, V. J. Trava-Airoldi, and E. J. Corat. 2008. "Cell Viability and Adhesion on as Grown Multi-wall Carbon Nanotube Films." *Materials Science and Engineering: C* 28 (2) (March 10): 264–269. doi:10.1016/j.msec.2007.01.003.

V. Lovat, D. Pantarotto, L. Lagostena, B. Cacciari, M. Grandolfo, M. Righi, G. Spalluto, M. Prato, and L. Ballerini. 2005. "Carbon Nanotube Substrates Boost Neuronal Electrical Signaling." *Nano Letters* 5 (6) (June 1): 1107–1110. doi:10.1021/nl050637m.

Y. Lu, T. Li, X. Zhao, M. Li, Y. Cao, H. Yang, and Y. Y. Duan. 2010. "Electrodeposited Polypyrrole/carbon Nanotubes Composite Films Electrodes for Neural Interfaces." *Biomaterials* 31 (19) (July): 5169–5181. doi:10.1016/j.biomaterials.2010.03.022.

J. R. Macdonald. 1991. "Application of Electrochemical Impedance Spectroscopy in Electrochemistry and Corrosion Science." In *Techniques for Characterization of Electrodes and Electrochemical Processes*, edited by R. Varma and J. R. Selman. Wiley.

J. R. Macdonald. 2010. "Utility of Continuum Diffusion Models for Analyzing Mobile-ion Immittance Data: Electrode Polarization, Bulk, and Generation-recombination Effects." *Journal of Physics. Condensed Matter: An Institute of Physics Journal* 22 (49) (November 16): 495101. doi:10.1088/0953-8984/22/49/495101.

J. R. Macdonald. 1992. "Impedance Spectroscopy." *Annals of Biomedical Engineering* 20 (3) (May 1): 289–305. doi:10.1007/BF02368532.

J. R. Macdonald. 2011. "Effects of Various Boundary Conditions on the Response of Poisson–Nernst–Planck Impedance Spectroscopy Analysis Models and Comparison with a Continuous-Time Random-Walk Model." *The Journal of Physical Chemistry A* 115 (46) (November 24): 13370–13380. doi:10.1021/jp206719g.

E. B. Malarkey, K. A. Fisher, E. Bekyarova, W. Liu, R. C. Haddon, and V. Parpura. 2009. “Conductive Single-Walled Carbon Nanotube Substrates Modulate Neuronal Growth.” *Nano Letters* 9 (1) (January 14): 264–268. doi:10.1021/nl802855c.

E. B. Malarkey, and V. Parpura. 2007. “Applications of Carbon Nanotubes in Neurobiology.” *Neurodegenerative Diseases* 4 (4): 292–299. doi:10.1159/000101885.

L. K. Massey. 2002. *Permeability Properties of Plastics and Elastomers, 2nd Ed.: A Guide to Packaging and Barrier Materials*. William Andrew.

M. Mattson, R. Haddon, and A. Rao. 2000. “Molecular Functionalization of Carbon Nanotubes and Use as Substrates for Neuronal Growth.” *Journal of Molecular Neuroscience* 14 (3) (June 1): 175–182. doi:10.1385/JMN:14:3:175.

H. S. Mayberg, A. M. Lozano, V. Voon, H. E. McNeely, D. Seminowicz, C. Hamani, J. M. Schwalb, and S. H. Kennedy. 2005. “Deep Brain Stimulation for Treatment-Resistant Depression.” *Neuron* 45 (5) (March): 651–660. doi:10.1016/j.neuron.2005.02.014.

G. C. McConnell, R. J. Butera, and R. V. Bellamkonda. 2009. “Bioimpedance Modeling to Monitor Astrocytic Response to Chronically Implanted Electrodes.” *Journal of Neural Engineering* 6 (5) (October 1): 055005. doi:10.1088/1741-2560/6/5/055005.

W. Q. Meeker, L. A. Escobar, and V. Chan. 2000. *Using Accelerated Tests to Predict Service Life in Highly-Variable Environments*.

D.R. Merrill, M. Bikson, and J. G. R. Jefferys. 2005. “Electrical Stimulation of Excitable Tissue: Design of Efficacious and Safe Protocols.” *Journal of Neuroscience Methods* 141 (2) (February 15): 171–198. doi:10.1016/j.jneumeth.2004.10.020.

R. P. Metzen, and T. Stieglitz. 2013. “The Effects of Annealing on Mechanical, Chemical, and Physical Properties and Structural Stability of Parylene C.” *Biomedical Microdevices*: 1–9. doi:10.1007/s10544-013-9758-8.

R. D. Meyer, S. F. Cogan, T. H. Nguyen, and R. D. Rauh. 2001. “Electrodeposited Iridium Oxide for Neural Stimulation and Recording Electrodes.” *IEEE Transactions on Neural Systems and Rehabilitation Engineering* 9 (1): 2–11. doi:10.1109/7333.918271.

S. Minnikanti, and N. Peixoto. 2011. “Implantable Electrodes with Carbon Nanotube Coatings.” In *Carbon Nanotubes Applications on Electron Devices*, edited by Jose Mauricio Marulanda. InTech. http://www.intechopen.com/books/carbon-

nanotubes-applications-on-electron-devices/implantable-electrodes-with-carbon-nanotube-coatings.

S. Minnikanti, M. G. A. G. Pereira, S. Jaraiedi, K. Jackson, C. M. Costa-Neto, Q. Li, and N. Peixoto. 2010. "*In vivo* Electrochemical Characterization and Inflammatory Response of Multiwalled Carbon Nanotube-based Electrodes in Rat Hippocampus." *Journal of Neural Engineering* 7 (1) (February 1): 016002. doi:10.1088/1741-2560/7/1/016002.

S. Minnikanti, P. Skeath, and N. Peixoto. 2009a. "Electrochemical Characterization of Multi-walled Carbon Nanotube Coated Electrodes for Biological Applications." *Carbon* 47 (3) (March): 884–893. doi:10.1016/j.carbon.2008.11.045.

M. Monthioux, and V. L Kuznetsov. 2006. "Who Should Be Given the Credit for the Discovery of Carbon Nanotubes?" *Carbon* 44 (9): 1621–1623.

J. Mozota, and B. E. Conway. 1981. "Modification of Apparent Electrocatalysis for Anodic Chlorine Evolution on Electrochemically Conditioned Oxide Films at Iridium Anodes." *Journal of The Electrochemical Society* 128 (10) (October 1): 2142–2149. doi:10.1149/1.2127205.

D. A. X. Nayagam, R. A. Williams, J. Chen, K. A. Magee, J. Irwin, J. Tan, P. Innis, et al. 2011. "Biocompatibility of Immobilized Aligned Carbon Nanotubes." *Small* (February): n/a–n/a. doi:10.1002/smll.201002083.

S. Negi, R. Bhandari, L Rieth, and F. Solzbacher. 2010. "*In vitro* Comparison of Sputtered Iridium Oxide and Platinum-coated Neural Implantable Microelectrode Arrays." *Biomedical Materials* 5 (1) (February): 015007. doi:10.1088/1748-6041/5/1/015007.

S. Negi, R. Bhandari, L. Rieth, R. Van Wagenen, and F. Solzbacher. 2010. "Neural Electrode Degradation from Continuous Electrical Stimulation: Comparison of Sputtered and Activated Iridium Oxide." *Journal of Neuroscience Methods* 186 (1) (January 30): 8–17. doi:10.1016/j.jneumeth.2009.10.016.

Y. Ni, H. Hu, E. B. Malarkey, B. Zhao, V. Montana, R. C. Haddon, and V. Parpura. 2005. "Chemically Functionalized Water Soluble Single-Walled Carbon Nanotubes Modulate Neurite Outgrowth." *Journal of Nanoscience and Nanotechnology* 5 (October): 1707–1712. doi:10.1166/jnn.2005.189.

M. A. L. Nicolelis, D. Dimitrov, J. M. Carmena, R. Crist, G. Lehew, J. D. Kralik, and S. P. Wise. 2003. "Chronic, Multisite, Multielectrode Recordings in Macaque Monkeys." *Proceedings of the National Academy of Sciences* 100 (19) (September 16): 11041–11046. doi:10.1073/pnas.1934665100.

R. H. Niessen, J. de Jonge, and P. H. L. Notten. 2006. “The Electrochemistry of Carbon Nanotubes I. Aqueous Electrolyte.” *Journal of The Electrochemical Society* 153 (8) (August 1): A1484–A1491. doi:10.1149/1.2205184.

S. Niyogi, M. A. Hamon, H. Hu, B. Zhao, P. Bhowmik, R. Sen, M. E. Itkis, and R. C. Haddon. 2002. “Chemistry of Single-Walled Carbon Nanotubes.” *Accounts of Chemical Research* 35 (12) (December 1): 1105–1113. doi:10.1021/ar010155r.

J. K. Olson, and S. D. Miller. 2004. “Microglia Initiate Central Nervous System Innate and Adaptive Immune Responses through Multiple TLRs.” *The Journal of Immunology* 173 (6) (September 15): 3916–3924.

M. E. Orazem, and B. Tribollet. 2008. *Electrochemical Impedance Spectroscopy*. Wiley.

T. Owens, A. A. Babcock, J. M. Millward, and H. Toft-Hansen. 2005. “Cytokine and Chemokine Inter-regulation in the Inflamed or Injured CNS.” *Brain Research Reviews* 48 (2) (April): 178–184. doi:10.1016/j.brainresrev.2004.12.007.

J. J. Pancrazio. 2008. “Neural Interfaces at the Nanoscale.” *Nanomedicine (London, England)* 3 (6) (December): 823–830. doi:10.2217/17435889.3.6.823.

K. H. Park, M. Chhowalla, Z. Iqbal, and F. Sesti. 2003. “Single-walled Carbon Nanotubes Are a New Class of Ion Channel Blockers.” *Journal of Biological Chemistry* 278 (50) (December 12): 50212 –50216. doi:10.1074/jbc.M310216200.

G. Paxinos, and C. Watson. 2007. *The Rat Brain in Stereotaxic Coordinates: Hard Cover Edition*. Academic Press.

N. Peixoto, K. Jackson, R. Samiyi, and S. Minnikanti. 2009. “Charge Storage: Stability Measures in Implantable Electrodes.” In , 658–661. doi:10.1109/IEMBS.2009.5333449.

V. H. Perry. 1994. *Macrophages and the Nervous System*. RG Landes.

Polikov, Vadim S., Patrick A. Tresco, and William M. Reichert. 2005. “Response of Brain Tissue to Chronically Implanted Neural Electrodes.” *Journal of Neuroscience Methods* 148 (1) (October 15): 1–18. doi:10.1016/j.jneumeth.2005.08.015.

C. Portet, G. Yushin, and Y. Gogotsi. 2007. “Electrochemical Performance of Carbon Onions, Nanodiamonds, Carbon Black and Multiwalled Nanotubes in Electrical Double Layer Capacitors.” *Carbon* 45 (13) (November): 2511–2518. doi:10.1016/j.carbon.2007.08.024.

A. Prasad, Q. S. Xue, V. Sankar, T. Nishida, G. Shaw, W. J. Streit, and J. C. Sanchez. 2012. “Comprehensive Characterization and Failure Modes of Tungsten Microwire Arrays in Chronic Neural Implants.” *Journal of Neural Engineering* 9 (5) (October 1): 056015. doi:10.1088/1741-2560/9/5/056015.

R. Q. Quiroga, and S. Panzeri. 2009. “Extracting Information from Neuronal Populations: Information Theory and Decoding Approaches.” *Nature Reviews Neuroscience* 10 (3) (March 1): 173–185. doi:10.1038/nrn2578.

T. Radman, Y. Su, J. Hi An, L. C. Parra, and M. Bikson. 2007. “Spike Timing Amplifies the Effect of Electric Fields on Neurons: Implications for Endogenous Field Effects.” *The Journal of Neuroscience* 27 (11) (March 14): 3030–3036. doi:10.1523/JNEUROSCI.0095-07.2007.

A. Ramachandran, M. Junk, K. P. Koch, and K. P. Hoffmann. 2007. “A Study of Parylene C Polymer Deposition Inside Microscale Gaps.” *IEEE Transactions on Advanced Packaging* 30 (4): 712–724. doi:10.1109/TADVP.2007.901662.

E. P. Randviir, and C. E. Banks. 2013. “Electrochemical Impedance Spectroscopy: An Overview of Bioanalytical Applications.” *Analytical Methods* (January 10). doi:10.1039/C3AY26476A. http://pubs.rsc.org/en/content/articlelanding/2013/ay/c3ay26476a.

A. R. Rezai, D. Finelli, J. A. Nyenhuis, G. Hrdlicka, J. Tkach, A. Sharan, P. Rugieri, P. H. Stypulkowski, and F. G. Shellock. 2002. “Neurostimulation Systems for Deep Brain Stimulation: *In vitro* Evaluation of Magnetic Resonance Imaging-related Heating at 1.5 Tesla.” *Journal of Magnetic Resonance Imaging* 15 (3) (March): 241–250. doi:10.1002/jmri.10069.

L. S. Robblee, J. L. Lefko, and S. B. Brummer. 1983. “Activated Ir: An Electrode Suitable for Reversible Charge Injection in Saline Solution.” *Journal of The Electrochemical Society* 130 (3) (March 1): 731–733. doi:10.1149/1.2119793.

N. J. Rothwell, and G. N. Luheshi. 2000. “Interleukin 1 in the Brain: Biology, Pathology and Therapeutic Target.” *Trends in Neurosciences* 23 (12) (December): 618–625.

A. Sabot, and S. Krause. 2002. “Simultaneous Quartz Crystal Microbalance Impedance and Electrochemical Impedance Measurements. Investigation into the Degradation of Thin Polymer Films.” *Analytical Chemistry* 74 (14) (July 1): 3304–3311. doi:10.1021/ac0200724.

J. P. Salvetat, J. M. Bonard, N. H. Thomson, A. J. Kulik, L. Forr, W. Benoit, and L. Zuppiroli. 1999. “Mechanical Properties of Carbon Nanotubes.” *Applied Physics A: Materials Science & Processing* 69 (3) (September): 255–260. doi:10.1007/s003390050999.

P. Sarkar, and S. N. Patrick. 1996. “Electrophoretic Deposition (EPD): Mechanisms, Kinetics, and Application to Ceramics.” *Journal of the American Ceramic Society* 79 (8) (August): 1987–2002. doi:10.1111/j.1151-2916.1996.tb08929.x.

F. Sauter-Starace, O. Bibari, F. Berger, P. Caillat, and A. L. Benabid. 2009. “ECoG Recordings of a Non-human Primate Using Carbon Nanotubes Electrodes on a Flexible Polyimide Implant.” In , 112–115. doi:10.1109/NER.2009.5109247.

T. Saxena, L. Karumbaiah, E. A. Gaupp, R. Patkar, K. Patil, M. Betancur, G. B. Stanley, and R. V. Bellamkonda. 2013. “The Impact of Chronic Blood–brain Barrier Breach on Intracortical Electrode Function.” *Biomaterials* 34 (20) (July): 4703–4713. doi:10.1016/j.biomaterials.2013.03.007.

E. M. Schmidt, M. J. Bak, and J. S. McIntosh. 1976. “Long-term Chronic Recording from Cortical Neurons.” *Experimental Neurology* 52 (3) (September): 496–506. doi:10.1016/0014-4886(76)90220-X.

M. Schuettler, M. Praetorius, S. Kammer, B. Schick, and T. Stieglitz. 2002. “Recording of Auditory Evoked Potentials in Rat Using a 60 Channel Polyimide Electrode Array: Preliminary Results.” In *Engineering in Medicine and Biology, 2002. 24th Annual Conference and the Annual Fall Meeting of the Biomedical Engineering Society EMBS/BMES Conference, 2002. Proceedings of the Second Joint*, 3:2109–2110 vol.3. doi:10.1109/IEMBS.2002.1053192.

D. Servello, M. Porta, M. Sassi, A. Brambilla, and M. M. Robertson. 2008. “Deep Brain Stimulation in 18 Patients with Severe Gilles de La Tourette Syndrome Refractory to Treatment: The Surgery and Stimulation.” *Journal of Neurology, Neurosurgery & Psychiatry* 79 (2) (February 1): 136 –142. doi:10.1136/jnnp.2006.104067.

J. P. Seymour, Y. M. Elkasabi, H. Y. Chen, J. Lahann, and D. R. Kipke. 2009. “The Insulation Performance of Reactive Parylene Films in Implantable Electronic Devices.” *Biomaterials* 30 (31) (October): 6158–6167. doi:10.1016/j.biomaterials.2009.07.061.

M. Shein, A. Greenbaum, T. Gabay, R. Sorkin, M. David-Pur, E. Ben-Jacob, and Y. Hanein. 2009. “Engineered Neuronal Circuits Shaped and Interfaced with Carbon Nanotube Microelectrode Arrays.” *Biomedical Microdevices* 11 (2) (April 1): 495–501. doi:10.1007/s10544-008-9255-7.

M. Shim, N. W. S. Kam, R. J. Chen, Y. Li, and H. Dai. 2002. “Functionalization of Carbon Nanotubes for Biocompatibility and Biomolecular Recognition.” *Nano Letters* 2 (4): 285–288.

J. D. Simeral, S. P. Kim, M. J. Black, J. P. Donoghue, and L. R. Hochberg. 2011. “Neural Control of Cursor Trajectory and Click by a Human with Tetraplegia 1000 Days after Implant of an Intracortical Microelectrode Array.” *Journal of Neural Engineering* 8 (2) (April 1): 025027. doi:10.1088/1741-2560/8/2/025027.

S. B. Sinnott. 2002. “Chemical Functionalization of Carbon Nanotubes.” *Journal of Nanoscience and Nanotechnology* 2 (2): 113–123.

R. Sorkin, A. Greenbaum, M. David-Pur, S. Anava, A. Ayali, E. Ben-Jacob, and Y. Hanein. 2009. “Process Entanglement as a Neuronal Anchorage Mechanism to Rough Surfaces.” *Nanotechnology* 20 (1) (January): 015101. doi:10.1088/0957-4484/20/1/015101.

B. H. Stark, and K. Najafi. 2001. “An Ultra-thin Hermetic Package Utilizing Electroplated Gold.” In *Dig. 11th IEEE Int. Conf. Solid-State Sensors and Actuators (Transducers’ 01)*, 194–197. https://www2.lirmm.fr/lirmm/interne/BIBLI/CDROM/MIC/2001/EUROSENSORS_2001/Data/1C3-05P.pdf.

P. Steegstra, and E. Ahlberg. 2012. “Influence of Oxidation State on the pH Dependence of Hydrous Iridium Oxide Films.” *Electrochimica Acta* 76 (August 1): 26–33. doi:10.1016/j.electacta.2012.04.143.

S. Sunderam, N. Chernyy, J. Mason, N. Peixoto, S. L. Weinstein, S. J. Schiff, and B. J. Gluckman. 2006. “Seizure Modulation with Applied Electric Fields in Chronically Implanted Animals.” In *28th Annual International Conference of the IEEE Engineering in Medicine and Biology Society, 2006. EMBS ’06*, 1612–1615. doi:10.1109/IEMBS.2006.259454.

D. H. Szarowski, M. D. Andersen, S. Retterer, A. J. Spence, M. Isaacson, H. G. Craighead, J. N. Turner, and W. Shain. 2003. “Brain Responses to Micro-machined Silicon Devices.” *Brain Research* 983 (1–2) (September 5): 23–35. doi:10.1016/S0006-8993(03)03023-3.

S. R. Taylor. 1989. “Assessing the Moisture Barrier Properties of Polymeric Coatings Using Electrical and Electrochemical Methods.” *IEEE Transactions on Electrical Insulation* 24 (5): 787–806. doi:10.1109/14.42159.

S. S. Thanawala, R. J. Baird, D. G. Georgiev, and G. W. Auner. 2008. “Amorphous and Crystalline IrO2 Thin Films as Potential Stimulation Electrode Coatings.” *Applied Surface Science* 254 (16) (June 15): 5164–5169. doi:10.1016/j.apsusc.2008.02.054.

M. M. J. Treacy, T. W. Ebbesen, and J. M. Gibson. 1996. “Exceptionally High Young’s Modulus Observed for Individual Carbon Nanotubes.” *Nature* 381 (6584) (June 20): 678–680. doi:10.1038/381678a0.

P. R. Troyk, and S. F. Cogan. 2005. “Sensory Neural Prostheses.” In *Neural Engineering*, edited by Bin He, 1–48. Bioelectric Engineering. Springer US. http://link.springer.com/chapter/10.1007/0-306-48610-5_1.

J. N. Turner, W. Shain, D. H. Szarowski, M. Andersen, S. Martins, M. Isaacson, and H. Craighead. 1999. “Cerebral Astrocyte Response to Micromachined Silicon Implants.” *Experimental Neurology* 156 (1) (March): 33–49. doi:10.1006/exnr.1998.6983.

M. Uematsu, and E. U. Frank. “Static Dielectric Constant of Water and Steam (American Chemical Society and the American Institute of Physics for the National Bureau of Standards, 1981).”

O. O. Van der Biest, and L. J. Vandeperre. 1999. “Electrophoretic Deposition of Materials.” *Annual Review of Materials Science* 29 (1): 327–352. doi:10.1146/annurev.matsci.29.1.327.

F. Velasco, M. Velasco, A. L. Velasco, F. Jimenez, I. Marquez, and M. Rise. 1995. “Electrical Stimulation of the Centromedian Thalamic Nucleus in Control of Seizures: Long-Term Studies.” *Epilepsia* 36 (1) (January): 63–71. doi:10.1111/j.1528-1157.1995.tb01667.x.

S. Venkatraman, J. Hendricks, Z. A. King, A. J. Sereno, S. Richardson-Burns, D. Martin, and J. M. Carmena. 2011. “*In vitro* and *In vivo* Evaluation of PEDOT Microelectrodes for Neural Stimulation and Recording.” *IEEE Transactions on Neural Systems and Rehabilitation Engineering* 19 (3): 307–316. doi:10.1109/TNSRE.2011.2109399.

J. L. Vitek. 2002. “Mechanisms of Deep Brain Stimulation: Excitation or Inhibition.” *Movement Disorders* 17 (S3) (March): S69–S72. doi:10.1002/mds.10144.

K. Wang, H. A. Fishman, H. Dai, and J. S. Harris. 2006. “Neural Stimulation with a Carbon Nanotube Microelectrode Array.” *Nano Letters* 6 (9): 2043–2048. doi:10.1021/nl061241t.

K. Wang, C. C. Liu, and D. M. Durand. 2009. “Flexible Nerve Stimulation Electrode with Iridium Oxide Sputtered on Liquid Crystal Polymer.” *IEEE Transactions on Bio-medical Engineering* 56 (1) (January): 6–14. doi:10.1109/TBME.2008.926691.

T. J. Webster, M. C. Waid, J. L. McKenzie, R. L. Price, and J. U. Ejiofor. 2004. “Nano-biotechnology: Carbon Nanofibres as Improved Neural and Orthopaedic Implants.” *Nanotechnology* 15 (1) (January 1): 48. doi:10.1088/0957-4484/15/1/009.

W. Wei, A. Sethuraman, C. Jin, N. A. Monteiro-Riviere, and R. J. Narayan. 2007. “Biological Properties of Carbon Nanotubes.” *Journal of Nanoscience and Nanotechnology* 7 (4-5) (May): 1284–1297.

J. D. Weiland, and D. J. Anderson. 2000. “Chronic Neural Stimulation with Thin-film, Iridium Oxide Electrodes.” *IEEE Transactions on Biomedical Engineering* 47 (7): 911–918. doi:10.1109/10.846685.

J.C. Williams, J. A. Hippensteel, J. Dilgen, W. Shain, and D. R. Kipke. 2007. “Complex Impedance Spectroscopy for Monitoring Tissue Responses to Inserted Neural Implants.” *Journal of Neural Engineering* 4 (4) (December): 410–423. doi:10.1088/1741-2560/4/4/007.

B. S. Wilson, C. C. Finley, D. T. Lawson, R. D. Wolford, D. K. Eddington, and W. M. Rabinowitz. 1991. “Better Speech Recognition with Cochlear Implants.” *Nature* 352 (6332) (July 18): 236–238. doi:10.1038/352236a0.

K. M. Woo, V. J. Chen, and P. X. Ma. 2003. “Nano-fibrous Scaffolding Architecture Selectively Enhances Protein Adsorption Contributing to Cell Attachment.” *Journal of Biomedical Materials Research Part A* 67A (2): 531–537. doi:10.1002/jbm.a.10098.

B. J. Woodford, R. R. Carter, D. McCreery, L. A. Bullara, and W. F. Agnew. 1996. “Histopathologic and Physiologic Effects of Chronic Implantation of Microelectrodes in Sacral Spinal Cord of the Cat.” *Journal of Neuropathology and Experimental Neurology* 55 (9) (September): 982–991.

X. Xie, L. Rieth, S. Merugu, P. Tathireddy, and F. Solzbacher. 2012. “Plasma-assisted Atomic Layer Deposition of Al2O3 and Parylene C Bi-layer Encapsulation for Chronic Implantable Electronics.” *Applied Physics Letters* 101 (9) (August 27): 093702–093702–5. doi:doi:10.1063/1.4748322.

H. Xu, J. Bai, J. Meng, W. Hao, H. Xu, and J. M. Cao. 2009. “Multi-walled Carbon Nanotubes Suppress Potassium Channel Activities in PC12 Cells.” *Nanotechnology* 20 (28) (July): 285102. doi:10.1088/0957-4484/20/28/285102.

K. Yamanaka. 1989. “Anodically Electrodeposited Iridium Oxide Films (AEIROF) from Alkaline Solutions for Electrochromic Display Devices.” *Japanese Journal of Applied Physics* 28 (Part 1, No. 4): 632–637. doi:10.1143/JJAP.28.632.

W. Yang, P. Thordarson, J. J. Gooding, S. P. Ringer, and F. Braet. 2007. “Carbon Nanotubes for Biological and Biomedical Applications.” *Nanotechnology* 18 (41) (October): 412001. doi:10.1088/0957-4484/18/41/412001.

H. Yasuda, Q. S. Yu, and M. Chen. 2001. “Interfacial Factors in Corrosion Protection: An EIS Study of Model Systems.” *Progress in Organic Coatings* 41 (4) (May): 273–279. doi:10.1016/S0300-9440(01)00142-4.

J. M. Yoo, S. Negi, P. Tathireddy, F. Solzbacher, J. I. Song, and L. W. Rieth. 2013. “Excimer Laser Deinsulation of Parylene-C on Iridium for Use in an Activated Iridium Oxide Film-coated Utah Electrode Array.” *Journal of Neuroscience Methods*. doi:10.1016/j.jneumeth.2013.02.010. http://www.sciencedirect.com/science/article/pii/S0165027013000769.

T. Yoshino, N. Baba, and K. Arai. 1987. “Electrochromic IrO_x Thin Films Formed in Sulfatoiridate (III, IV) Complex Solution by Periodic Reverse Current Electrolysis (PRIROF).” *Japanese Journal of Applied Physics* 26 (Part 1, No. 9) (September 20): 1547–1549. doi:10.1143/JJAP.26.1547.

K. F. Zaidi, Z. H. Benchekroun, S. Minnikanti, J. Pancrazio, and N. Peixoto. 2010. “*In vitro* Models for Measuring Charge Storage Capacity.” In *26th Southern Biomedical Engineering Conference SBEC 2010, April 30 - May 2, 2010, College Park, Maryland, USA*, edited by Keith E. Herold, Jafar Vossoughi, and William E. Bentley, 97–100. IFMBE Proceedings 32. Springer Berlin Heidelberg. http://link.springer.com/chapter/10.1007/978-3-642-14998-6_26.

E. Zoulias, E. Varkaraki, N. Lymberopoulos, C. N. Christodoulous, and G. N. Karagiorgis. 2004. “A Review on Water Electrolysis.” *TCJST* 4 (2): 41–71.

Y. Zuo, R. Pang, W. Li, J. P. Xiong, and Y. M. Tang. 2008. “The Evaluation of Coating Performance by the Variations of Phase Angles in Middle and High Frequency Domains of EIS.” *Corrosion Science* 50 (12) (December): 3322–3328. doi:10.1016/j.corsci.2008.08.049.

BIOGRAPHY

Saugandhika Minnikanti graduated from Rajasthan University, India, in 2002. She received her Masters of Science from George Mason University in 2007.